eROSITA X-ray Analysis of the PeVatron Candidate Westerlund 1

Master's Thesis in Physics

Presented by
Konstantin Haubner

September 22, 2023

Dr. Karl Remeis-Sternwarte
Friedrich-Alexander-Universität Erlangen-Nürnberg

Supervisor: Prof. Dr. Manami Sasaki

Zusammenfassung

Die Natur von PeVatrons, Quellen kosmischer Strahlung mit PeV-Energien, ist noch unklar. Erschwert wird ihre Untersuchung durch die Entartung zwischen hadronischen und leptonischen γ-Strahlungsszenarien, da zur Erklärung kosmischer Strahlung Hadronenbeschleunigung erforderlich ist. Das Ziel dieser Arbeit ist daher die Suche nach Synchrotron-Röntgenstrahlung von dem PeVatron-Kandidaten J1646−458, in dessen Mitte der massereiche junge Sternhaufen Westerlund 1 liegt. Da Synchrotronstrahlung nur von Leptonen erwartet wird, würde sie eine Identifizierung der Quelle als Leptonenbeschleuniger erlauben. Zusätzlich wurde auch die diffuse Röntgenstrahlung von Westerlund 1 selbst untersucht, um ihre Erzeugung besser zu verstehen.

Die genutzten Daten stammen von den ersten vier Himmelsdurchmusterungen des eROSITA-Teleskopes an Bord von SRG. Für die Untersuchung der Strahlung um Westerlund 1 herum wurden vier ringförmige Analyseregionen mit einem Radius bis zu 40 arcmin um den Haufen definiert. Da diese stark mit Streulicht kontaminiert sind, habe ich sie mit geeigneten Testregionen mit ähnlicher Kontamination verglichen, indem ich Gauß-Verteilungen an die Differenz der Analyse- und Testspektren gefittet und mit t-Tests die Anwesenheit einer zusätzlichen Quellkomponente in den Analyseregionen geprüft habe. Außerdem habe ich die Spektren der Analyseregionen sowie das diffuse Emissionsspektrum des Sternhaufens selbst gefittet.

Wie durch die negativen Mittelwerten der Gauß-Fits wurde auch durch die t-Tests eine höhere Countzahl in den Analyseregionen abgelehnt, und zwar abhängig von der jeweiligen Region mit einer Signifikanz $\gtrsim 3\sigma$. Daher folgere ich, dass in den eROSITA-Daten keine Evidenz für eine Synchrotronkomponente um Westerlund 1 herum vorhanden ist. Basierend auf Hintergrundfits an die Analyseregionen habe ich eine Schranke auf den Synchrotronfluss von $\eta_\mathrm{X} \lesssim 3.06 \cdot 10^5\,\mathrm{TeV}^{-1}\,\mathrm{cm}^{-2}\,\mathrm{s}^{-1}$ bestimmt.

Dieser Wert wurde dann für einen Fit der spektralen Energieverteilung der Quelle verwendet und so eine Schranke auf das magnetische Feld um den Sternhaufenrandstoß von $B \lesssim 2\,\mu\mathrm{G}$ gefunden. Dieses Ergebnis stimmt überein mit Schätzungen in der Literatur. Insbesondere folgt damit, dass sowohl das leptonische Emissionsszenario am Randstoß des Sternhaufens als auch das hadronische Emissionsszenario im Haufen selbst möglich bleiben.

Das diffuse Spektrum von Westerlund 1 selbst konnte mit einem doppelt thermischen Modell oder mit einem Modell mit einer thermischen und einer nichtthermischen Komponente gefittet werden. Daher schließe ich, dass die Präferenz für das rein thermische Modell, die in der Literatur besteht, gültig bleibt. Die Leuchtkraft der Strahlung kann durch thermalisierte Sternwinde mit einem möglichen Beitrag bis zu etwa 40% von Vorhauptreihensternen erklärt werden.

Abstract

The physical nature of PeVatrons, sources which accelerate cosmic rays to PeV energies, is still unclear. In particular, the analysis of PeVatrons is complicated by the degeneration between hadronic and leptonic γ-ray emission scenarios, since the explanation of cosmic rays requires hadron acceleration. Therefore, this thesis aims at the search for X-ray synchrotron radiation from the PeVatron candidate J1646−458, at the center of which lies the massive young star cluster Westerlund 1. Since synchrotron radiation is only expected from leptons, its detection would allow the identification of J1646−458 as a leptonic accelerator. In addition, the diffuse X-ray emission from the star cluster Westerlund 1 itself was studied to constrain its X-ray emission mechanism.

The data for this study comes from the first four all-sky surveys of the eROSITA telescope on board SRG. For studying the diffuse emission around Westerlund 1, four ring-shaped analysis regions up to a radius of 40 arcmin around the cluster were defined. Due to strong stray light contamination in these regions, I compared them to suitable test regions of similar contamination via Gaussian fits to the difference of analysis and test spectra and via t-tests for the presence of a source component in the analysis spectra. Further, I performed spectral fits to the analysis regions around Westerlund 1 as well as to the diffuse spectrum of the star cluster itself.

Consistent with the negative mean values of the Gaussian fits, the t-tests rejected the null hypothesis in favor of more counts in the test than in the analysis regions at a $\gtrsim 3\sigma$ level, depending on the region. Therefore, I conclude that no synchrotron component around Westerlund 1 is evident in the eROSITA data. Based on fits of background models to the analysis regions, I derived an upper limit on the synchrotron flux of $\eta_X \lesssim 3.06 \cdot 10^5\,\mathrm{TeV}^{-1}\,\mathrm{cm}^{-2}\,\mathrm{s}^{-1}$.

Using this value for a leptonic spectral energy distribution fit, an upper limit on the magnetic field strength at the cluster wind termination shock of $B \lesssim 2\,\mu\mathrm{G}$ was found. This value is consistent with previous estimates in the literature. Importantly, this means that both the leptonic emission scenario at the cluster wind termination shock and the hadronic scenario inside Westerlund 1 itself are still viable.

Regarding Westerlund 1 itself, its diffuse spectrum could be fitted either with a model with two thermal components or with a model with a thermal and a nonthermal component. Therefore, I conclude that the preference for the purely thermal model reported in the literature is still valid. The diffuse thermal emission luminosity can be explained by thermalized stellar winds inside the cluster with a potential contribution up to around 40% from pre-main sequence stars.

Table of Contents

List of Figures

List of Tables

List of Abbreviations

APEC astrophysical plasma emission code

ARF ancillary response file

ART-XC Astronomical Roentgen Telescope – X-ray Concentrator

CCD charge-coupled device

CGM circumgalactic medium

CMB cosmic microwave background

CR cosmic ray

CXB cosmic X-ray background

DSA diffusive shock acceleration

eFEDS eROSITA Final Equatorial Depth Survey

eRASS eROSITA all-sky survey

eROSITA extended Roentgen survey with an imaging telescope array

eSASS eROSITA Science Analysis Software System

Fermi LAT Fermi Large Area Telescope

FWC filter wheel closed

GTI good time interval

HAWC High-Altitude Water Cherenkov Observatory

HE high-energy

H.E.S.S. High Energy Stereoscopic System

IC inverse Compton

ISM	interstellar medium
LHAASO	Large High Altitude Air Shower Observatory
LHB	local hot bubble
LMXB	low mass X-ray binary
PMS	pre-main sequence
PWN	pulsar wind nebula
RMF	redistribution matrix function
SED	spectral energy distribution
SNR	supernova remnant
SRG	Spektr-Roentgen-Gamma
SWCX	Solar wind charge exchange
TM	telescope module
UHE	ultra-high-energy
VHE	very-high-energy
Wd 1	Westerlund 1
WR	Wolf-Rayet
XMM Newton	X-ray Multi-mirror Newton

CHAPTER 1

Motivation

> Δεν μπορούμε ν’ αλλάξουμε την πραγματικότητα, λέει ένας αγαπημένος μου Βυζαντινός μυστικός· ας αλλάξουμε τότε το μάτι που βλέπει την πραγματικότητα.
>
> Νίκος Καζαντζάκης, Αναφορά στον Γκρέκο

1.1 X-ray Studies of PeVatron Candidates

Cosmic rays (CRs) are charged particles, mainly protons and heavier nuclei, which are produced in astrophysical sources and propagate through interstellar space. Alongside electromagnetic radiation, magnetic fields, and the distribution and flow of gas, they are one of the main drivers of the dynamics of the interstellar medium (ISM). Highlighting their importance for galaxy evolution, their energy density is $\approx 1\,\mathrm{eV\,cm^{-3}}$ (Boulares & Cox, 1990; Webber, 1998) and thus comparable to the energy densities of the radiative, thermal (both Draine, 2010), turbulent (Mac Low & Klessen, 2004), and magnetic (Yoast-Hull et al., 2016) phases of the ISM.

Specifically, there is evidence that CRs influence the geometry of the supernova remnants (SNRs) where they are accelerated (Pais et al., 2018), i.e., of the expanding stellar ejecta of supernova explosions which shock the surrounding ISM. Further, CRs change the metal abundances in the ISM and impact star formation (Padovani et al., 2020). In addition, they might offer an explanation for the presence of cool high-velocity clouds in the circumgalactic medium (CGM) (Wiener et al., 2019) and efficiently drive strong galactic winds, as first noted by Ipavich (1975). Importantly, these CR driven winds might help regulate the baryon content of galaxies (Dashyan & Dubois, 2020) and therefore might even help to alleviate the ”missing baryons” problem, i.e, the fact that the fraction of baryonic mass to dark matter mass in galaxies regularly falls below the cosmic mean baryon density (Ruszkowski & Pfrommer, 2023).

In short, these effects of CRs exemplify the relevance of understanding their origin, propagation, and properties for building a better picture of galaxy evolution. Among these, this thesis is occupied with the origin of Galactic CRs with energies above $\approx 1\,\mathrm{PeV} = 10^{15}\,\mathrm{eV}$, which is not well understood yet.

Below an energy of $\approx 1\,\mathrm{PeV}$, the so-called "standard paradigm" of Galactic CRs posits that 1. they are diffusively confined in the magnetic halo of the Galaxy, and that 2. they are accelerated at the shock fronts of isolated SNRs via the process of diffusive shock acceleration (DSA). This model accounts well for the energy in Galactic CRs and the slope of their spectrum (Gabici et al., 2019). However, the standard paradigm struggles to explain the origin of CRs with energies around $\approx 1\,\mathrm{PeV}$. Theoretically, it is challenging to achieve such high energies in SNRs. Indeed, SNRs are often predicted to reach maximum CR energies of $\approx 10 - 100\,\mathrm{TeV}$, falling short of the required energies by at least an order of magnitude (Brose et al., 2022; Lagage & Cesarsky, 1983).

Empirically, the study of Galactic CRs of the highest energies recently achieved a breakthrough through the detection of Galactic sources which accelerate particles to energies above 1 PeV (Abeysekara et al., 2020; Cao et al., 2021). These sources, which were dubbed "PeVatrons", can be identified via secondary γ-rays produced by the CRs which they accelerate. Adding to the theoretical problems of the isolated SNR paradigm, many of the recently discovered PeVatrons show no spatial correlation with known SNRs.

Consequently, the detection of PeVatrons rekindled the interest in alternative sources of CRs. Among these are, for example, pulsar wind nebulae (PWNe), microquasars, and young star clusters (Cardillo & Giuliani, 2023). In this thesis, the focus lies on the X-ray analysis of the massive young star cluster Westerlund 1 (Wd 1) which is spatially correlated with the PeVatron candidate HESS J1646−458 (Abramowski et al., 2012; Aharonian et al., 2022). In particular, I performed the first X-ray analysis of the extended region coinciding with HESS J1646−458 using data from the extended Roentgen survey with an imaging telescope array (eROSITA) (Predehl et al., 2021) on board the Spektr-Roentgen-Gamma (SRG) orbital observatory (Sunyaev et al., 2021).

X-ray observations of PeVatrons are crucial because they can provide additional information on the origin of the γ-rays associated with a PeVatron. The reason is that secondary γ-rays do not definitely identify a source as a CR accelerator, since the emission can in principle stem from two different processes: 1. In the so-called leptonic scenario, relativistic electrons produce γ-rays via the inverse Compton (IC) upscattering of photons. 2. In the so-called hadronic scenario, accelerated protons produce pions which then decay into γ-photons. Since CRs are mainly hadronic in nature, a hadronic source population is required for explaining the origin of CRs above $\approx 1\,\mathrm{PeV}$.

Luckily, in the leptonic scenario, an electron population should produce synchrotron radiation in addition to IC γ-rays if a strong enough magnetic field is present. This is not expected in the hadronic scenario, since the large mass of protons suppresses the production of synchrotron radiation. Consequently, the detection or non-detection of X-ray synchrotron radiation can help to constrain the γ-ray emission scenario as well as the magnetic field strength around a source. Therefore, I performed such an analysis on the surroundings of the Wd 1 star cluster.

1.2 X-ray Studies of Young Star Clusters

In addition to the extended X-ray emission around Wd 1, I also studied the diffuse X-ray emission from the star cluster itself using eROSITA. The main aim of this analysis lies in better understanding the X-ray content of young massive star clusters like Wd 1. For example, this emission can stem from the magnetic activity of T-Tauri and protostars, the winds of OB and Wolf-Rayet (WR) stars, SNRs, and the compact objects remaining after the deaths of massive stars (Clark et al., 2008).

In particular, X-ray observations of young star clusters can provide constraints on their low-mass pre-main sequence (PMS) stellar content which might not be observable in the optical or infrared due to source confusion, therefore allowing new insights into the star formation in such clusters. In addition, a part of the diffuse X-ray emission in young star clusters should stem from stellar winds of massive stars. This way, X-ray observations can constrain the influence of stellar winds from star clusters on galaxy evolution, e.g., whether winds trigger or quench star formation in the ISM, or to which extent they increase the metal abundances in the surrounding medium (Muno et al., 2006).

In principle, however, some of the emission of the star cluster could also stem from nonthermal radiation. This could then indicate the presence of accelerated particles inside the cluster, providing evidence for CR acceleration. Theoretically, such a process could happen at colliding stellar winds or SNR shocks inside the cluster.

CHAPTER 2

Cosmic Rays

> Others there were, countless to our thought though known each and numbered in the mind of Illúvatar, whose labour lay elsewhere and in other regions and histories of the Great Tale, amid stars remote and worlds beyond the reach of the furthest thought.
>
> J.R.R. Tolkien, Myths Transformed

2.1 Detection

The atmosphere of Earth is constantly bombarded by charged particles which are called ”cosmic rays (CRs)” in astrophysics. These CRs are mainly protons, fewer heavier nuclei, even fewer electrons, and a small amount of antiparticles. Their energies span about 14 orders of magnitude, from $\sim 1\,\mathrm{MeV}$ to $\sim 10^{20}\,\mathrm{eV} \sim 10\,\mathrm{J}$. Given the proton mass $m_\mathrm{p} \approx 0.9\,\mathrm{GeV}$, it follows that a large fraction of CRs are well in the relativistic regime and move with velocities close to the speed of light. Similar to their energies, the particle flux of CRs spans 15 orders of magnitude and decreases from about $1\,\mathrm{m}^{-2}\,\mathrm{s}^{-1}\,\mathrm{sr}^{-1}$ at $1\,\mathrm{GeV}$ to about $1\,\mathrm{km}^{-2}\,\mathrm{century}^{-1}\,\mathrm{sr}^{-1}$ at $10^{20}\,\mathrm{eV}$ (Longair, 2011).

Historically, CRs were first discovered by the Austrian physicist Victor Hess. In 1912, he measured the ionization rate as a function of height above the ground during several balloon flights. Contrary to his expectation, he found an increase of the ionization rate with increasing height. As an explanation, he suggested a new type of radiation which enters the atmosphere from above (Hess, 1912).

In that regard, it is important to note that the CRs in the atmosphere have a different composition from the CRs in space. This is because primary CRs, which are accelerated in astrophysical sources, can interact with the medium they traverse and thus produce secondary CRs. In the ISM, this changes the chemical composition of CRs, e.g., via the production of boron from carbon in spallation reactions (Gabici et al., 2019). Further, in the atmosphere of Earth, CRs produce large amounts of muons, and, if their energy is high enough, air showers. Specifically, these air showers typically stem from the production of a neutral pion which subsequently decays into γ-photons. These can cascade downwards, producing more electrons and photons via pair production and bremsstrahlung (Workman, 2022).

From the ground, CRs can then be detected through the Cherenkov radiation produced by their secondary air showers and muons. Unfortunately, such measurements of the primary CRs and secondary particles produces on Earth cannot reveal the production sites of the particles. This is because CRs are charged and thus deflected in the Galactic magnetic field. Luckily, however, CRs can produce electromagnetic radiation via different nonthermal processes, e.g., bremsstrahlung, synchrotron radiation, or IC scattering. Therefore, sources of CRs can be identified via the detection of nonthermal radiation from astrophysical sources. This radiation is in principle observable over a large range of frequencies from radio over X-rays up to γ-rays, depending on the detailed nature of the source and its environment.

2.2 Spectrum

One of the most characteristic properties of CRs' is their energy spectrum. It is common practice in astrophysics to give spectra in the form of differential flux as a function of energy. For the following discussion, differential flux is defined as

$$\Phi(E) := \frac{\mathrm{d}N}{\mathrm{d}A\mathrm{d}t\mathrm{d}\Omega\mathrm{d}E}, \tag{2.2.1}$$

where N is the number of particles traversing an area A during time t. This particle flux originates from a solid angle Ω. Importantly, it is measured in an infinitesimal energy interval $\mathrm{d}E$. This allows to obtain the total particle flux in an energy interval between E_1 and E_2 by integrating equation 2.2.1 between these energies.

When discussing the spectrum of CRs, it is important to note that there are several different ways to give this differential flux depending on the precise meaning of N and E (Workman, 2022). In this thesis, the differential flux is given as the CR particle number per energy-per-nucleus and as the nucleon number per energy-per-nucleon.

The overall differential flux spectrum of CRs as measured by several different observatories and missions is given in figure 2.1. It was taken from the PhD thesis Lenok (2022). There are several things to note about the spectrum:

1. The differential flux is given in particle number per kinetic energy-per-nucleus. It is multiplied with the kinetic energy of the nucleus squared to aid readability and to provide a proxy for the energy flux per energy bin.

2. The left hand side of the plot gives information on the spectra of individual particle species while the right hand side gives the summed-up spectrum of all species. All data

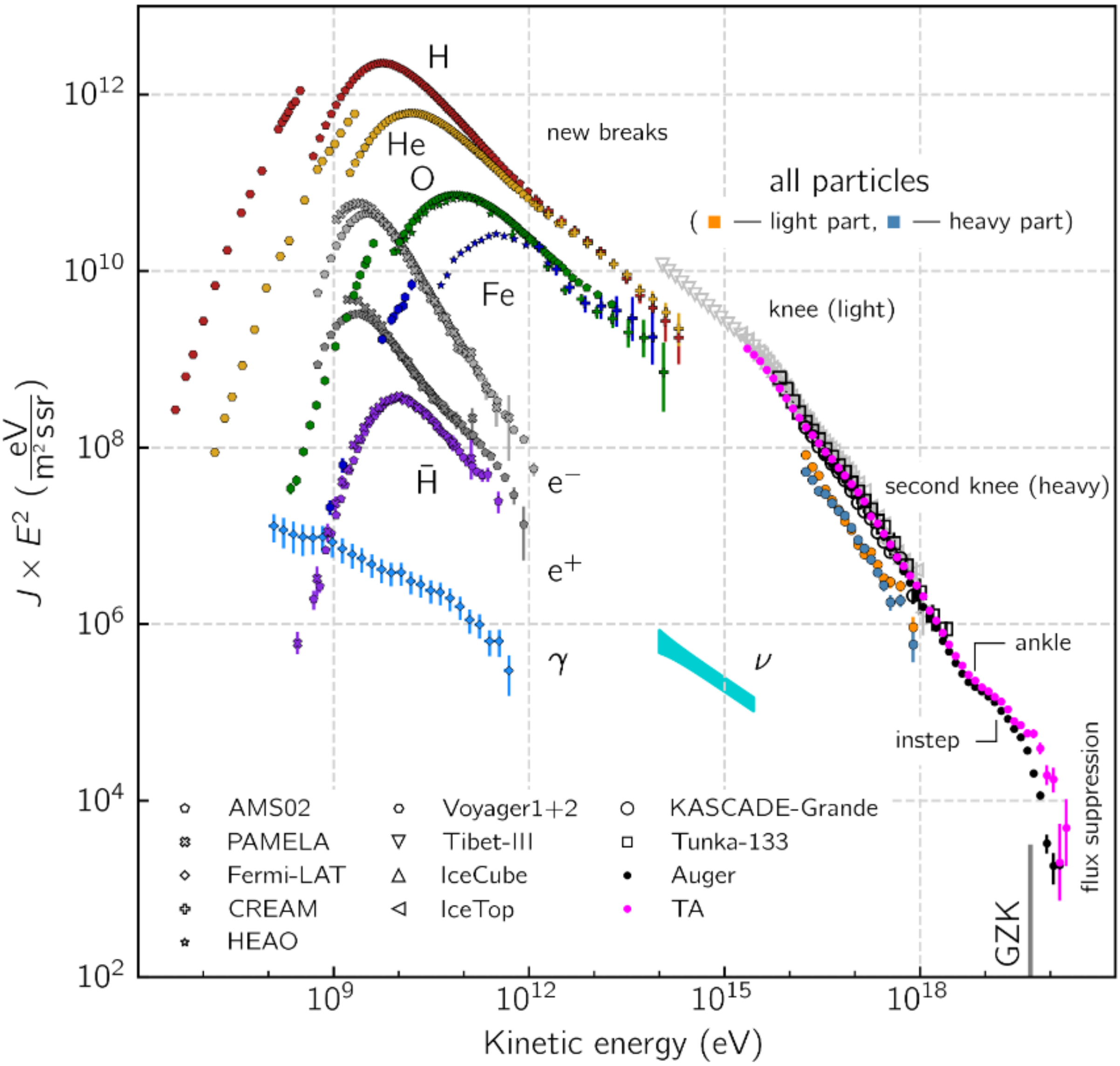

Figure 2.1: Differential CR flux as a function of kinetic energy per nucleus for individual particle species (left hand) and all particle species summed up (right hand). For more information on the figure, see the main text. Taken from Lenok (2022).

points come from measurements as indicated in the legend. The orange and blue data points labeled ”light part” and ”heavy part” indicate the spectra of light and heavy particles.

3. Given for comparison in blue is an estimate of the extragalactic γ-ray background as measured by the Fermi Large Area Telescope (Fermi LAT) between 100 MeV and 820 GeV (Ackermann et al., 2015). In a similar manner, the turquoise data gives an estimate of the astrophysical neutrino flux as measured by IceCube (Aartsen et al., 2015).

4. The label ”GZK” is the Greisen–Zatsepin–Kuz’min cutoff. At such high energies, CRs loose energies via the production of pions in interactions with cosmic microwave background (CMB) photons (Lenok, 2022). Other labels in the figure indicate features of the spectrum which are discussed in the following part of this section.

Below energies of a few GeV, the spectrum of CRs approximately follows a power law with a spectral index $\alpha \approx 0$ (Ruszkowski & Pfrommer, 2023) and is modulated by Solar activity. In particular, the intensity of these low-energy CRs is anticorrelated with Solar activity. The origin of this part of the CR spectrum is often attributed to Solar flares in combination with Galactic sources (Workman, 2022).

In the energy range from a few GeV to about 100 TeV, the spectrum of CRs is well described by a power law given by (Longair, 2011; Workman, 2022)

$$\Phi(E) \approx 1.8 \left(\frac{E}{1\,\mathrm{GeV}} \right)^{-\alpha} \text{nucleons}\,\mathrm{cm}^{-2}\,\mathrm{s}^{-1}\,\mathrm{sr}^{-1}\,\mathrm{GeV}^{-1}. \tag{2.2.2}$$

In general, the spectrum is characterized by several spectral breaks which are often interpreted as indications of changes in the underlying physics of CR production and transport. Up to $\approx 3\,\mathrm{PeV}$, the spectral index α is in the range from 2.5 to 2.7. At these energies, a major break happens which is commonly referred to as the ”knee” of the CR spectrum. Above the knee, the spectral index is $\alpha \approx 3.1$, until the spectrum flattens again at the so-called ”ankle” at $\approx 3\,\mathrm{EeV}$ (Longair, 2011). Above the ankle, the spectral index is $\alpha \approx 2.6$ (Aab et al., 2020). Both the knee and the ankle are clearly visible in figure 2.1.

It is plausible to assume a change of the dominant CR source population from Galactic to extragalactic somewhere around the ankle. The argument for this is based on the Larmor radius of charged particles, also called their gyroradius. This is the radius of the circular orbit of a charged particle in a uniform magnetic field and is given by

$$r_{\mathrm{Larmor}} = \frac{\gamma m v_{\perp}}{|q| B}, \tag{2.2.3}$$

where γ is the Lorentz factor of the charged particle, m is its mass, $v_{\perp}$ is its velocity perpendicular to the ambient magnetic field B, and q is its charge. For a proton ($m_{\mathrm{p}} \approx 0.9\,\mathrm{GeV}$, $q = +e$) with energy 3 EeV in the average Galactic magnetic field of $B_{\mathrm{gal}} \sim 1\,\mu\mathrm{G}$, this results in a Larmor radius $r_{\mathrm{Larmor}} \sim 10\,\mathrm{kpc}$. This is of the order of magnitude of the radius of the Galactic disc, meaning that above energies of $\approx 3\,\mathrm{EeV}$ CRs are not confined to the Galaxy anymore.

This is a rough estimate, but it demonstrates why the source population of CRs should change from Galactic to extragalactic around the ankle. On the other hand, below this point down to a few GeV, the main sources of CRs are probably of Galactic origin.

Besides the general features of the CR spectrum discussed above, the recent decades have brought great improvements in our understanding of the properties of CRs. In particular, the CR measurement experiments PAMELA and AMS02 demonstrated that the idea of a featureless power law spectrum up to the knee was to simple. Below the knee, there are several features in the CR spectrum as indicated by the label ”new breaks” in figure 2.1, e.g., a decrease in the spectral index of hydrogen and helium around $\approx 300\,\mathrm{GeV}$ and an overall difference in the spectral index between these two particle species. In particular, the latter feature is not understood yet. At higher energies, between the knee and the ankle, there is another spectral break called the ”second knee” at $\approx$ 100 PeV. It is sometimes interpreted as an alternative point for the transition from Galactic to extragalactic sources (Gabici et al., 2019). Another break around 13 EeV is labeled ”instep” in figure 2.1 (Lenok, 2022). However, an extensive discussion of these additional features is beyond the scope of this thesis.

2.3 Composition

Besides their spectrum, another source of information on CRs is their composition with respect to different particle species. Overall, roughly 98% of CRs are nuclei, stripped of their electrons, and only roughly 2% are electrons. In particular, this means that the composition of CRs is dominated by hadrons. In total, about 85% of the particles are protons, about 12% are helium nuclei, and about 2% are heavier nuclei (Simpson, 1983). There is also a small positron and antiproton component in the composition of CRs (Lenok, 2022).

With respect to the hadronic component of CRs, figure 2.2 shows the abundances of different elements in low-energy CRs ($\approx$ 0.2 GeV per nucleon) compared to the element abundances in the Solar system. The y-axis is normalized to a value of 10^3 for silicon.

There are several things to note about this plot (Workman, 2022):

1. Overall, the relative abundances of different elements are similar in CRs and in the Solar system. Specifically, the dependence of the stability of nuclei on whether their atomic number is odd or even seems to be noticeable in both samples.

2. A notable difference is the overabundance of the light elements lithium, beryllium, and boron in CRs compared to the Solar system. Similarly, the elements just below iron (scandium, titanium, vanadium, chromium, and manganese) are overabundant in CRs.

3. Relative to the heavy elements, hydrogen and helium are underabundant in the composition of CRs in comparison to the Solar system values.

A natural explanation for the features of the CR composition is that they arise as an imprint of particle propagation through the Galaxy: As primary CRs, which are accelerated to their respective energies in astrophysical sources, propagate through the ISM, they can interact with the surrounding medium in spallation reactions. This way, heavier nuclei can be fragmented into lighter ones, e.g., boron can be produced from carbon. Employing the physics of this production mechanism, it is then possible to derive further information about the origin of CRs. For example, from the ratio of secondary to primary particles, one can calculate the residence time of CRs in the Galactic disk $\tau_{\mathrm{CR}} \sim 1$ Myr (Gabici et al., 2019).

It is important to note that figure 2.2 gives the relative element abundances only around a specific energy per nucleon for the CRs. In general, the relative abundances are different at different energies because the spectra of different species of particles cannot properly be described by a single power law. Instead, one requires different power law indices for different species, changing the relative abundances. For example, as revealed by the PAMELA experiment, the ratio of helium over hydrogen in the composition of CRs increases for increasing energies (Adriani et al., 2011). To give another example, the ratio of secondary to primary CRs decreases with increasing energy. This observation can be interpreted as a sign of decreasing residence time of CRs in the Galactic disk with increasing energy (Workman, 2022).

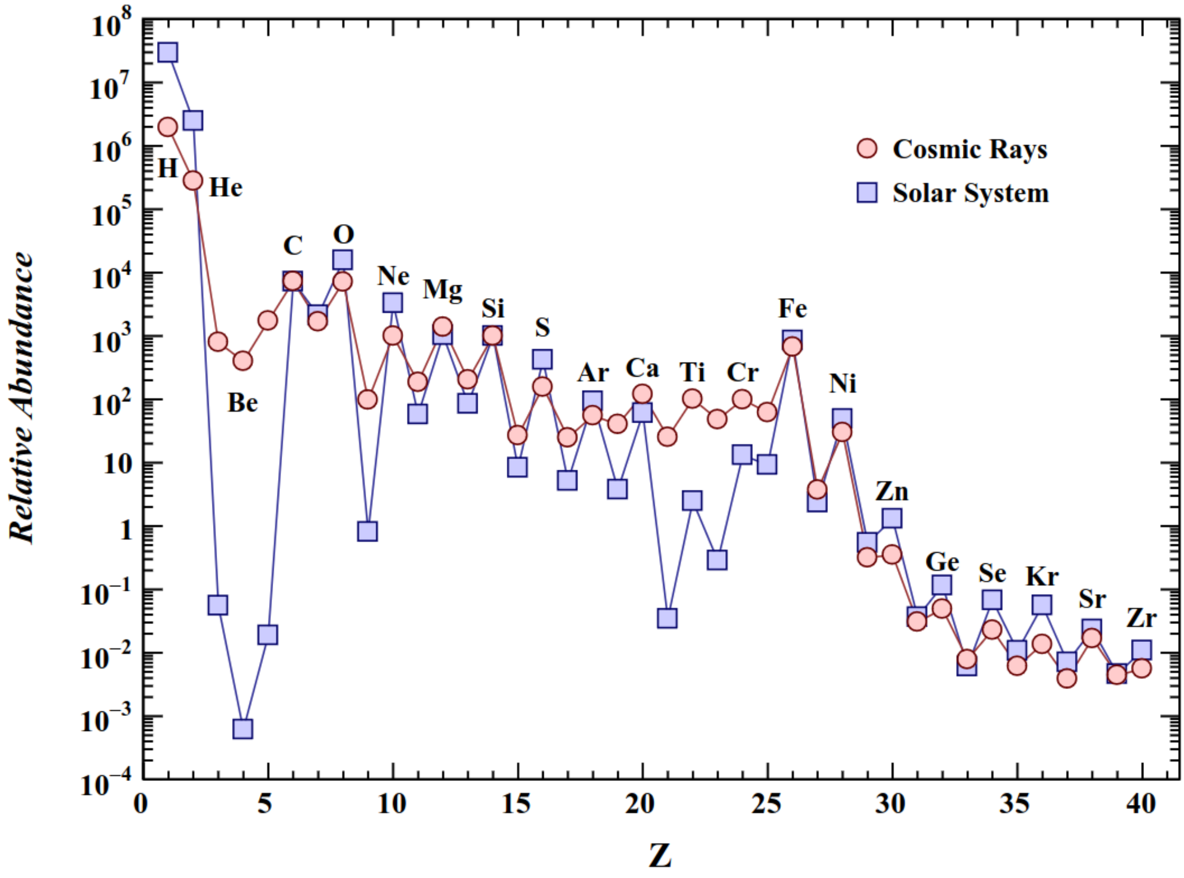

Figure 2.2: Relative elementary abundances of low-energy CRs (≈ 0.2 GeV per nucleon) compared to the Solar system abundances. The y-axis is normalized to a relative abundance of 10^3 for silicon. Taken from Workman (2022).

2.4 Secondary Radiation

Since CRs are charged particles, they are deflected in the magnetic field of the Milky Way. Due to this, the directions from which CRs arrive in the Solar system and on Earth have lost correlation with the actual direction of their production sites. This effect hinders an easy identification of the astrophysical sources which accelerate the Galactic share of CRs.

For this reason, observations of secondary electromagnetic radiation produced by CRs is of particular interest. As photons are electrically neutral, they are not deflected in magnetic fields and allow to draw conclusion about the sources of the charged particles producing them. In general, the nonthermal radiative processes through which CRs loose energy are separated into leptonic and hadronic, based on whether a process dominates for leptonic CR particles (mainly electrons) or hadronic CR particles (mainly protons and helium nuclei). The dominant leptonic processes are bremsstrahlung, synchrotron radiation, and inverse Compton (IC) scattering, while the dominant hadronic process is the production and the decay of pions.

Since IC radiation, bremsstrahlung, and pion decay are mainly observed in γ-rays and the discussion of γ-rays is relevant for this thesis, it is worth noting that this radiation is commonly separated into three bands based on the energy of the photons: high-energy (HE) between 100 MeV and 100 GeV, very-high-energy (VHE) between 100 GeV and 100 TeV, and ultra-high-energy (UHE) between 100 TeV and 100 PeV.

2.4.1 Bremsstrahlung

Bremsstrahlung (German for ”braking radiation”) is emitted by charged particles which are deflected in the electrostatic field of another charge. The typical case is the deflection of an electron in the electrostatic field of a nucleus. In this case, the alternative term free-free radiation refers to the fact that the emitting electron remains unbound to a nucleus over the entire course of the process.

Since Galactic CRs have energies above $\approx$ 1 GeV, CR electrons are well in the relativistic regime. The exact formula for the energy loss of a single relativistic electron due to bremsstrahlung was derived by Bethe and Heitler (1934) and is given by

$$-\left(\frac{\mathrm{d}E_\mathrm{e}}{\mathrm{d}t}\right)_\mathrm{brems} = \frac{Z(Z+1.3)e^6 n}{8\pi^2\varepsilon_0^3 m_\mathrm{e}^2 c^4 h} E_\mathrm{e}\left(\ln\left(\frac{183}{Z^{1/3}}\right)+\frac{1}{8}\right) \propto E_\mathrm{e}, \tag{2.4.1}$$

where E_e is the energy of the emitting electron, Z is the proton number of the particles deflecting the electron, e is the elementary charge, n is the density of the medium deflecting the electron, ε_0 is the vacuum permittivity, m_e is the electron mass, c is the speed of light, and h is Planck’s constant.

One can see that the energy loss due to bremsstrahlung is directly proportional to the electron’s energy and to the density of the surrounding medium. In particular, this means that bremsstrahlung gets more efficient in dense gaseous regions. In most cases, however, synchrotron and IC radiation are more efficient than bremsstrahlung (Aharonian, 2004).

Regarding the analysis of bremsstrahlung spectra, it is interesting to note that they closely reflect the spectral energy distributions of the underlying particle populations. For example, in the case of bremsstrahlung from a power law electron distribution with spectral index α, the resulting bremsstrahlung spectrum, too, is a power law with index α (Aharonian, 2004).

2.4.2 Synchrotron Radiation

Synchrotron radiation is of particular relevance for this thesis since my analysis focuses on the search for synchrotron radiation around Wd 1. This radiation is produced by relativistic charged particles propagating through a magnetic field. Due to their interaction with the magnetic field, they gyrate around the field lines and in the process loose energy via the emission of synchrotron radiation. This radiation is not emitted isotropically, but rather within a tight cone in the direction of the particle's motion (Bartelmann, 2013).

The energy loss of an electron due to synchrotron radiation can be calculated via (Bartelmann, 2013)

$$-\left(\frac{\mathrm{d}E_{\mathrm{e}}}{\mathrm{d}t}\right)_{\mathrm{syn}} = c\gamma^2\sigma_{\mathrm{T}}U_{\mathrm{B}}, \tag{2.4.2}$$

where σ_{T} is the Thomson cross section and $U_{\mathrm{B}} := B^2/4\pi$ is the energy density of the magnetic field B. Pay attention to the fact that the formula is given in cgs units.

From this formula, one can see why synchrotron radiation is usually considered to be a leptonic process. Since $\gamma \propto m^{-1}$, where m is the mass of the emitting particle, and $\sigma_{\mathrm{T}} \propto m^{-2}$, the synchrotron power drops with the fourth power of the emitting particle's mass. Further, since $m_{\mathrm{p}} \approx 2000 m_{\mathrm{e}}$, the synchrotron power of protons is suppressed by 13 orders of magnitude compared to electrons. This simple argument demonstrates that synchrotron radiation from protons can be neglected in most astrophysical systems.

The synchrotron radiation spectrum of a single emitting relativistic electron can be seen in figure 2.3. It is peaked approximately around a characteristic frequency

$$\nu_{\mathrm{c}} = \frac{3e}{4\pi mc} B\gamma^2. \tag{2.4.3}$$

Below ν_{c}, the spectral power has the shape of a rising power law, and above ν_{c}, the spectral power drops of exponentially (Blumenthal & Gould, 1970).

The synchrotron spectrum of a population of electrons can be calculated via convolving the underlying electron distribution function with the synchrotron spectral power. One particularly notable result is that for a power law electron distribution with index α_{e}, the resulting synchrotron spectrum has a power law shape with index (Blumenthal & Gould, 1970)

$$\alpha_{\mathrm{syn}} = \frac{\alpha_{\mathrm{e}} - 1}{2}. \tag{2.4.4}$$

The general idea of this convolution is shown in figure 2.4. In reality, this power law shape cannot continue indefinitely to lower frequencies. At some frequency, the power law index becomes negative due to synchrotron self-absorption, i.e., the emitting plasma becomes opaque to its own synchrotron radiation.

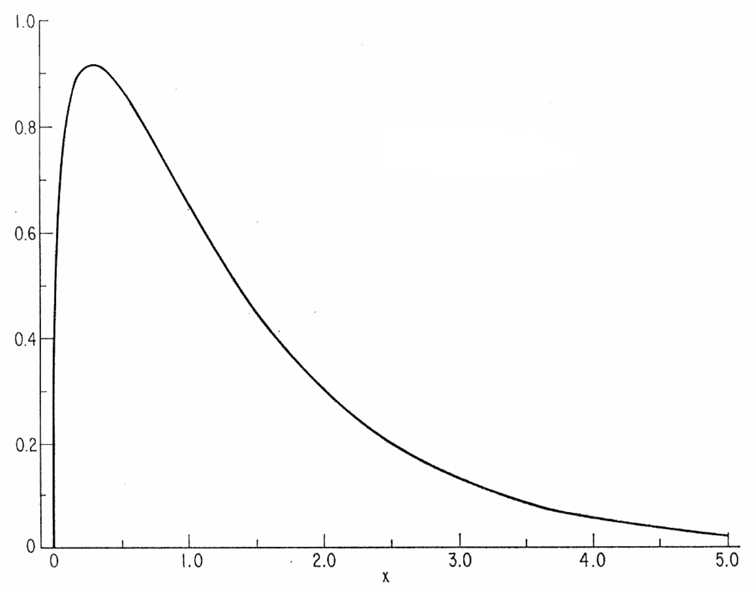

Figure 2.3: Synchrotron spectrum of a single radiating electron. The x-axis is given in $x := \nu/\nu_c$, with the frequency of the radiation ν. The y-axis is given in arbitrary units of spectral power. Adapted from Blumenthal and Gould (1970).

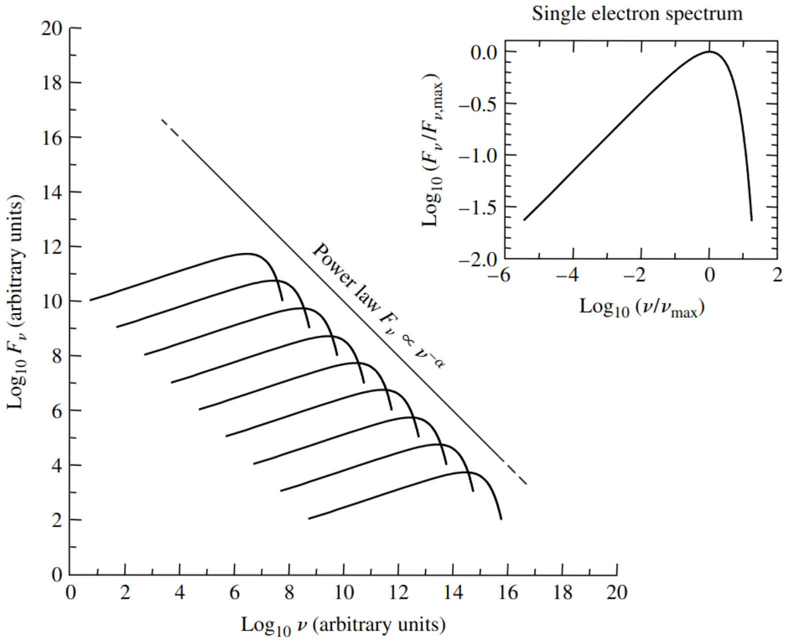

Figure 2.4: Sum of the synchrotron spectra of individual electrons producing power law spectra. For comparison, the synchrotron spectrum of a single electron is shown in the upper right corner. Adapted from Carroll and Ostlie (2014).

2.4.3 Inverse Compton Scattering

Compton scattering is the inelastic scattering of a high-energy photon from a charged particle, usually an electron. In the case of electrons, this translates to a necessary photon energy of $h\nu > m_e c^2 \approx 511\,\mathrm{keV}$, i.e., γ-photons. In the process of the scattering, the energy of the photon decreases and the energy of the electron increases.

As the name suggests, inverse Compton (IC) scattering is the inverse process in which the photon energy is smaller than the electron energy. Low-energy photons can then be upscattered to higher energies from relativistic electrons. In astrophysics, IC scattering is a common source of γ-rays in the presence of a population of relativistic electrons. Common target photon fields for this process are the CMB, the diffuse star light of the Galaxy, and the infrared background of the Galaxy.

The cross section of IC scattering depends only on the product of the energies of the participating electron and photon populations. This can be written in the form of the dimensionless parameter (Aharonian, 2004)

$$\kappa_0 := \left(\frac{E_\gamma}{m_e c^2}\right)\left(\frac{E_e}{m_e c^2}\right), \tag{2.4.5}$$

with the photon energy E_γ.

Based on this parameter, one can distinguish two different regimes. 1. In the Thomson regime, one has $\kappa_0 << 1$ and the cross section approaches the classical Thomson cross section, i.e., $\sigma_{\mathrm{IC}} \approx \sigma_{\mathrm{T}}(1 - 2\kappa_0) \approx \sigma_{\mathrm{T}}$. 2. In the ultrarelativistic Klein-Nishina regime, one has $\kappa_0 >> 1$ and the cross section drops for higher energies according to (Aharonian, 2004)

$$\sigma_{\mathrm{IC}}^{\mathrm{KN}} \approx \frac{3\sigma_{\mathrm{T}} \ln(4\kappa_0)}{8\kappa_0}. \tag{2.4.6}$$

In the Thomson regime, the energy E_{IC} of a photon emitted via the IC process can be approximated as (Aharonian et al., 1997)

$$E_{\mathrm{IC}} \approx \frac{4}{3} h\nu_0 \left(\frac{E_e}{m_e c^2}\right)^2, \tag{2.4.7}$$

where $\nu_0 = E_\gamma / h$ is the frequency of the target photon field. Assuming the CMB as the target photon field, one has a typically frequency of $\nu_0 \approx 40\,\mathrm{GHz}$ according to Wien's displacement law. Further, assuming electron energies of $\approx 100\,\mathrm{TeV}$, the resulting IC photons have typical energies of $E_{\mathrm{IC}} \sim 10\,\mathrm{TeV}$.

Finally, just like for synchrotron radiation, in the Thomson regime a power law electron distribution produces an IC spectrum with a power law shape and spectral index

$$\alpha_{\mathrm{IC}} = \frac{\alpha_e - 1}{2}. \tag{2.4.8}$$

In the Klein-Nishina regime, however, the slope of the spectrum is noticeably steeper (Aharonian, 2004).

2.4.4 Pion Production and Decay

The secondary radiation mechanisms discussed so far are the ones relevant in a leptonic scenario. However, CRs are mainly protons and helium nuclei, which are hadronic in nature. These hadrons can produce γ-rays via interactions with protons or other nuclei in the ISM. Specifically, the interaction of a hadronic CR particle with an ambient proton or nucleus can result in the creation of a pion, kaon, or hyperon, which then quickly decays afterwards.

The dominant channel is the production of pions, the lightest leptons which consist of up and down quarks and antiquarks. Specifically, there are three types of pions, negative, positive, and neutral. Their composition is (Workman, 2022)

$$\pi^+ \ : \ u\bar{d}, \qquad\qquad \pi^- \ : \ \bar{u}d, \qquad\qquad \pi^0 \ : \ (u\bar{u} - d\bar{d})/\sqrt{2}.$$

For producing a pion, the kinetic energy of a CR proton must exceed (Aharonian, 2004)

$$E_{\text{threshold}} = 2m_\pi^2 \left(1 + \frac{m_\pi}{4m_\text{p}}\right) \approx 280\,\text{MeV}, \tag{2.4.9}$$

with $m_\pi \approx 135\,\text{MeV}$ the pion mass.

Both charged and neutral pions are unstable with mean life times of $\sim 10^{-8}$ s and $\sim 10^{-17}$ s, respectively. The dominant decay channels of charged pions are

$$\pi^+ \longrightarrow \mu^+ + \nu_\mu, \tag{2.4.10}$$

$$\pi^- \longrightarrow \mu^- + \bar{\nu}_\mu, \tag{2.4.11}$$

with a branching ratio of $\approx 99.99\%$ (Workman, 2022). The muons can further decay into electrons or positrons and neutrinos. In the context of multi-messenger astronomy, this means that neutrinos can serve as additional evidence for CR acceleration and subsequent hadronic interactions. In practice, however, the association of measured neutrinos with a particular source region is hampered by the low interaction rate of neutrinos and consequently the low statistics of neutrino measurements. Indeed, the IceCube neutrino observatory only recently reported the first-ever detection of neutrino emission at the 4.5σ level from the Galactic plane (IceCube Collaboration et al., 2023).

More relevant in the context of this thesis is the decay of neutral pions, which creates photons. In particular, the dominant decay channel is

$$\pi^0 \longrightarrow 2\gamma, \tag{2.4.12}$$

with a branching ratio of $\approx 98.82\%$ (Workman, 2022).

Given the pion mass of $m_\pi \approx 135\,\text{MeV}$, in the rest frame of the pion each photon gets an energy of $m_\pi/2 \approx 67.5\,\text{MeV}$ and is thus already well in the γ-ray band. In the laboratory frame, one has to consider the additional energy which the γ-rays obtain from the neutral pion via a Lorentz boost.

Since the hadronic emission scenario via the production and the decay of pions depends on the presence of sufficient ambient gas for the CR particles to react with, it is subject to constraints on the gas density surrounding a potential source. For example, observations of the 21 cm hyper fine structure emission line of neutral hydrogen gas, called HI in astronomy, or of the CO($J = 1 - 0$) transition of carbon monoxide associated with molecular clouds can indicate the presence of sufficiently dense material for the pions to interact with.

2.5 Diffusive Shock Acceleration

In the search for explanations for how CRs are accelerated, the physical process of DSA is a particularly powerful tool. The main reason for this is the shape of the CR spectrum, as discussed in section 2.2. Despite the spectral breaks and differences between particle species discussed there, the summed up CR spectrum is still well described by a power law with a single spectral index up to the knee. The appeal of DSA lies in the fact that it predicts an accelerated particle spectrum of exactly this general shape.

The two main requirements for DSA to take place are 1. the presence of a strong shock wave and 2. the isotropization of the momentum vectors of the particle population after it crossed this shock. Shock waves are discontinuities in the properties of a fluid, e.g., density, velocity, temperature, which arise when perturbations propagate through the fluid with velocities larger than its respective signal speed. In astrophysics, shocks are usually found in collisionless plasmas. In such a case, the relevant speed is the Alfvén speed v_A of the medium, i.e., the propagation speed of perturbations of ions and the magnetic field in a plasma. A shock is then called strong if $\mathcal{M}_\mathrm{A} := U/v_\mathrm{A} >> 1$ holds for the Alfvén Mach number $\mathcal{M}_\mathrm{A}$ of the shock, where U is the velocity of the shock. Such strong shocks are ubiquitous in astrophysics and are, for example, found in SNRs, between stellar winds of massive stars, as wind termination shocks surrounding star clusters, or in the jets of active galactic nuclei. The isotropization of the particle directions usually happens by the scattering from perturbations in the magnetic field of the shock region.

The basic idea of DSA can be demonstrated using figure 2.5. The vertical black line in each panel depicts the position of the shock front, while the dark grey region to the left has already been shocked and the light grey region to the right is not shocked yet. It is common to call the region to the left downstream and the region to the right, which corresponds to the surrounding ISM, upstream.

Panel a shows the rest frame of the upstream medium. In this frame, the shock front moves to the right with velocity U as it shocks more and more of the upstream medium. Further, the downstream medium moves to the right with velocity $v_2 = 3U/4$. This can be calculated from the so-called Rankine-Hugoniot equations which relate the upstream pressure p_1, temperature T_1, and density ρ_1 to the corresponding downstream properties, marked with the index 2. In particular, these equations also imply that the compression factor $r := \rho_2/\rho_1$ approaches 4 for strong shocks.

It is convenient to analyze shocks in the rest frame of the shock front, as shown in panel b. In this frame, the upstream medium moves to the left through the shock front with the shock speed $|U|$, while the downstream medium moves to the left with $v_2 = U/4$.

Panel c illustrates a population of high-energy particles in the rest frame of the upstream medium. Their momentum vectors are randomized via the scattering from magnetic instabilities and, importantly, they are randomized with respect to the rest frame of the upstream medium. Since their velocities are random, some of these particles will advect through the shock front into the downstream medium, which moves with velocity $3U/4$ with respect to the upstream medium. Due to this change in velocity of the surrounding medium, the particles gain energy proportional to U/c. Panel d then demonstrates how this process repeats itself in the downstream medium: The particle propagation directions are randomized in the downstream rest frame, some of them return upstream and, importantly, gain energy proportional to U/c. Crucially, DSA is such a powerful acceleration mechanism because the particles gain energy upon every crossing of the shock front, no matter the direction, and they cross it repeadetly in a stochastic process.

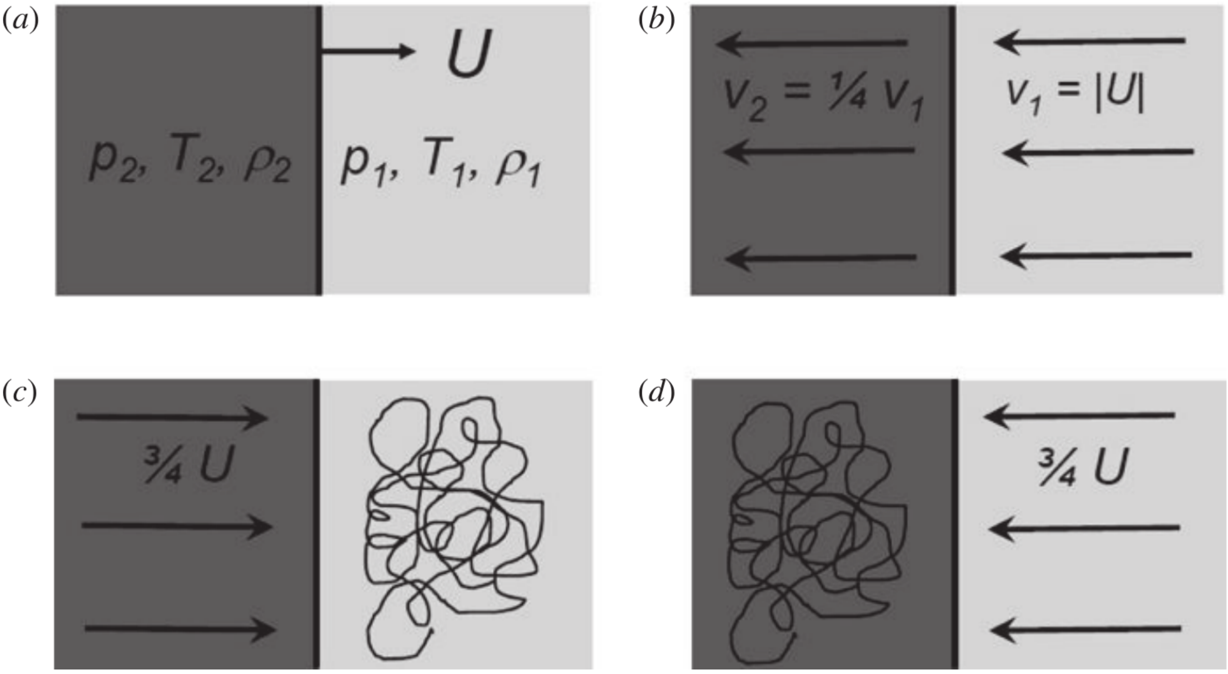

Figure 2.5: Schematic representation of the geometry of DSA. The vertical black line marks the position of the shock. The unshocked upstream medium is to the right, the shocked downstream medium to the left. Taken from Longair (2011). *Panel a:* The shock moves to the right in the rest frame of the upstream medium. *Panel b:* Both the downstream and the upstream medium move to the left in the rest frame of the shock front. *Panel c:* The momentum vectors of particles are randomized in the rest frame of the upstream medium. *Panel d:* The momentum vectors of particles are randomized in the rest frame of the downstream medium.

More explicitly, the spectrum of accelerated particles resulting from DSA can be calculated following Longair (2011). One can start with a particle with initial energy E_0 and energy E after crossing the shock two times. Then one can define the parameter β such that $E = \beta E_0$. On the other hand, each particle has a certain probability $1 - p$ of escaping from the acceleration region after crossing the shock two times. Accordingly, for N_0 the initial particle number, $N = pN_0$ particles remain in the acceleration region after two crossings.

Now considering k acceleration cycles, i.e., $2k$ crossings of the shock, the energy of a particle is $E = \beta^k E_0$ and the number of remaining particles is $N = p^k N_0$. Equating the k's in these expressions, one obtains

$$\frac{N}{N_0} = \left(\frac{E}{E_0}\right)^{\frac{\ln p}{\ln \beta}}. \tag{2.5.1}$$

Since N is defined as the number of particles remaining in the acceleration region after having reached energy E, it can also be phrased as the number of particles reaching at least energy E. The differential number of particles with exactly energy E can be found by differentiation, which yields

$$\frac{\mathrm{d}N}{\mathrm{d}E} = \kappa \left(\frac{E}{E_0}\right)^{-1+\frac{\ln p}{\ln \beta}}, \tag{2.5.2}$$

where κ is some suitable constant factor.

The index of this power law can be calculated from some basic considerations. First of all, from the appropriate Lorentz transformation into the new frame of reference after crossing the shock and from averaging over the possible orientations of the momentum vector, the average fractional energy increase of a particle with energy E after two crossings is

$$\left\langle \frac{\Delta E}{E} \right\rangle = \frac{4}{3}\frac{V}{c}, \tag{2.5.3}$$

where $V = 3U/4$. This dependence of the energy gain on the first power of V/c is why DSA is sometimes referred to as ”first-order Fermi acceleration in the presence of strong shocks”, as compared to second-order Fermi acceleration with $\Delta E/E \propto (V/c)^2$.

Next, from the definition of β one gets

$$\beta = 1 + \frac{4}{3}\frac{V}{c} = 1 + \frac{U}{c}. \tag{2.5.4}$$

On the other hand, p can be calculated from the number of particles advected away from the shock in the downstream medium. The flux of high-energy particles crossing the shock is $nc/4$, with the particle number density n (Longair, 2011). In the rest frame of the upstream medium, the shock front approaches the randomized particle distribution. In the downstream rest frame, however, the shock receeds from the downstream particle distribution with velocity $U/4$. This leads to a flux of escaping particles of $nU/4$. Overall, this gives a fraction of lost particles per acceleration cycle U/c, and thus

$$p = 1 - \frac{U}{c}. \tag{2.5.5}$$

Using the information that the shock is nonrelativistic and $U/c << 1$, one can then approximate the logarithms of β and p as

$$\ln \beta = \ln\left(1 + \frac{U}{c}\right) \approx \frac{U}{c}, \tag{2.5.6}$$

$$\ln p = \ln\left(1 - \frac{U}{c}\right) \approx -\frac{U}{c}. \tag{2.5.7}$$

Plugging these results into equation 2.5.2 yields

$$\frac{\mathrm{d}N}{\mathrm{d}E} \propto E^{-2}. \tag{2.5.8}$$

Accordingly, DSA predicts the accelerated particle distribution to be a power law with an index of 2. Regarding the spectrum of CRs, one has to note that the power law index of CRs from the GeV range to the knee is $\approx 2.7 \neq 2$. However, it is still remarkable that a relatively simple consideration of collisionless shocks leads to efficient particle acceleration and a universal power law slope in many potential astrophysical contexts. Further, as will be discussed in the next section, the discrepancy between the DSA power law index and the CR index can plausibly be explained in a scenario which also considers the CR transport in the Galaxy.

The treatment of DSA provided here gives a good idea of the general mechanism, but it suffers from several oversimplifications. For example, it assumes the simplest shock geometry, a planar shock, and it neglects energy losses due to radiation and interactions of particles. In particular, the approach discussed here is a test particle ansatz, i.e., the effect of the accelerated CRs on the surrounding fluid is neglected. For example, in a more realistic approach, CRs can induce so-called streaming instabilities in the magnetic field of the medium which they can then scatter from themselves. This can lead to a steepening of the spectral slope above the power law index of 2 (Gabici et al., 2019). These effects are discussed in greater length in, e.g., Drury (1983), but are beyond the scope of this thesis.

2.6 Isolated Supernova Remnant Paradigm

Due to its ability to produce a universal power law distribution of accelerated particles based on relatively common astrophysical phenomena, DSA suggests itself as a part of the explanation for the origin of CRs. Still, a satisfying theory also needs to address the exact nature of the acceleration sites and the transport of the particles to Earth.

In that regard, the scenario which enjoyed the greatest support in the astrophysical community up to this point is built around DSA at the shocks of SNRs. The main ideas of this standard paradigm can be summed up as follows (Gabici et al., 2019):

1. The energy for the acceleration of CRs is provided by supernova explosions in the Galactic disk.

2. CRs are accelerated from the ISM via DSA in SNRs.

3. CRs are diffusively transported in the Galactic halo.

2.6.1 Reasoning behind the Standard Paradigm

An extensive discussion of the development and reasoning of the standard paradigm is beyond the scope of this thesis. Still, I want to give an idea of some of the most important arguments surrounding the three pillars listed above.

A connection between supernova explosions and the origin of CRs was first proposed by Baade and Zwicky (1934) and the model has seen considerable development since then. A very basic but nevertheless important point is that supernovae in the Galaxy provide a sufficient amount of energy per time to explain the energy in CRs. In particular, the total energy in Galactic CRs can be estimated from their energy density $w_{\mathrm{CR}} \approx 1\,\mathrm{eV\,cm^{-3}}$ (Boulares & Cox, 1990; Webber, 1998) times the volume of the Galaxy V_{MW}. Assuming a cylindrical shape with radius $r_{\mathrm{MW}} = 10\,\mathrm{kpc}$ and height $h_{\mathrm{MW}} = 1\,\mathrm{kpc}$, this gives a total energy in CRs $W_{\mathrm{CR}} \sim 10^{55}\,\mathrm{erg}$. Dividing this by the residence time of CRs $\tau_{\mathrm{CR}} \sim 1\,\mathrm{Myr}$, as discussed in section 2.3, yields a total CR injection power of $P_{\mathrm{CR}} \sim 10^{41}\,\mathrm{erg\,s^{-1}}$.

Turning to supernova explosions now, their energy is typically assumed to be $E_{\mathrm{SN}} \sim 10^{51}\,\mathrm{erg}$. With a typical number of two to three supernovae per century in the Galaxy, the power of supernova explosions is $P_{\mathrm{SN}} \sim 10^{42}\,\mathrm{erg\,s^{-1}}$. This is an order of magnitude larger than P_{CR}, meaning that supernovae could provide the necessary energy for CRs if an average of 10% of the energy of a supernova goes into the acceleration of particles.

Regarding the transport of CRs, another important insight is provided by their residence time. Since Galactic CRs are relativistic particles, $\tau_{\mathrm{CR}} \sim 1\,\mathrm{Myr}$ corresponds to a travelled distance of $\sim 100\,\mathrm{kpc}$, which is an order of magnitude above the size of the Galaxy. This problem can be solved by assuming that CRs move diffusively through the Galaxy, i.e., stochastically via the scattering from perturbations in the Galactic magnetic field. In fact, secondary-to-primary ratios imply that CRs are not only diffusively confined in the Galactic disk, but in the larger Galactic halo (Gabici et al., 2019).

The strength of this diffusion is set by the diffusion coefficient D. For CRs with an energy of $\approx 1\,\mathrm{GeV}$, this coefficient can be estimated to be $D \sim 10^{28} - 10^{29}\,\mathrm{cm^2\,s^{-1}}$. Importantly, it is not independent of the particle energy, i.e., particles of different energy are diffused with different efficiencies and also have different escape times from the Galaxy. Roughly speaking, one gets $D(E) \propto E^{\delta}$ with $\delta \sim 0.3 - 0.6$, meaning that higher energy particles diffuse faster and thus also escape faster from the Galaxy (Gabici et al., 2019).

Combining this energy-dependent transport of CRs through the Galaxy with the observed index of the CR spectrum up to the knee, $\alpha \approx 2.7$, leads to a necessary injection spectrum of CRs with a slope of $2.1 - 2.4$. This is quite close to the predicted slope of accelerated particles derived for DSA in section 2.5. Remember that the index of DSA is exactly 2 only in the test particle approximation, but gets slightly steeper when this assumption is relaxed. Therefore, DSA seems to provide a nice fit to the observed CR spectrum.

Returning to supernovae, these explosions are not only capable of providing enough energy for CRs, but their remnants are also plausible acceleration sites. After an initial supernova explosion, an SNR arises in which the stellar ejecta of the supernova continue to expand outwards, shocking the ISM in the process. Since the ejecta are heated to high temperatures, SNRs emit mainly thermal X-rays. However, many SNRs are also observed to produce nonthermal radiation in the radio and sometimes also the X-ray band, which is well explained by synchrotron radiation produced by accelerated particles at the SNR shock front (Ballet, 2006). As discussed in section 2.4, this is expected from leptonic CRs in the presence of a magnetic field.

An example for this can be seen in figure 2.6, which shows an X-ray image of the SNR Cassiopeia A. The emission surrounding the SNR ejecta which is shown in blue is best described by nonthermal synchrotron radiation at the shock wave ahead of the stellar ejecta in the ISM.

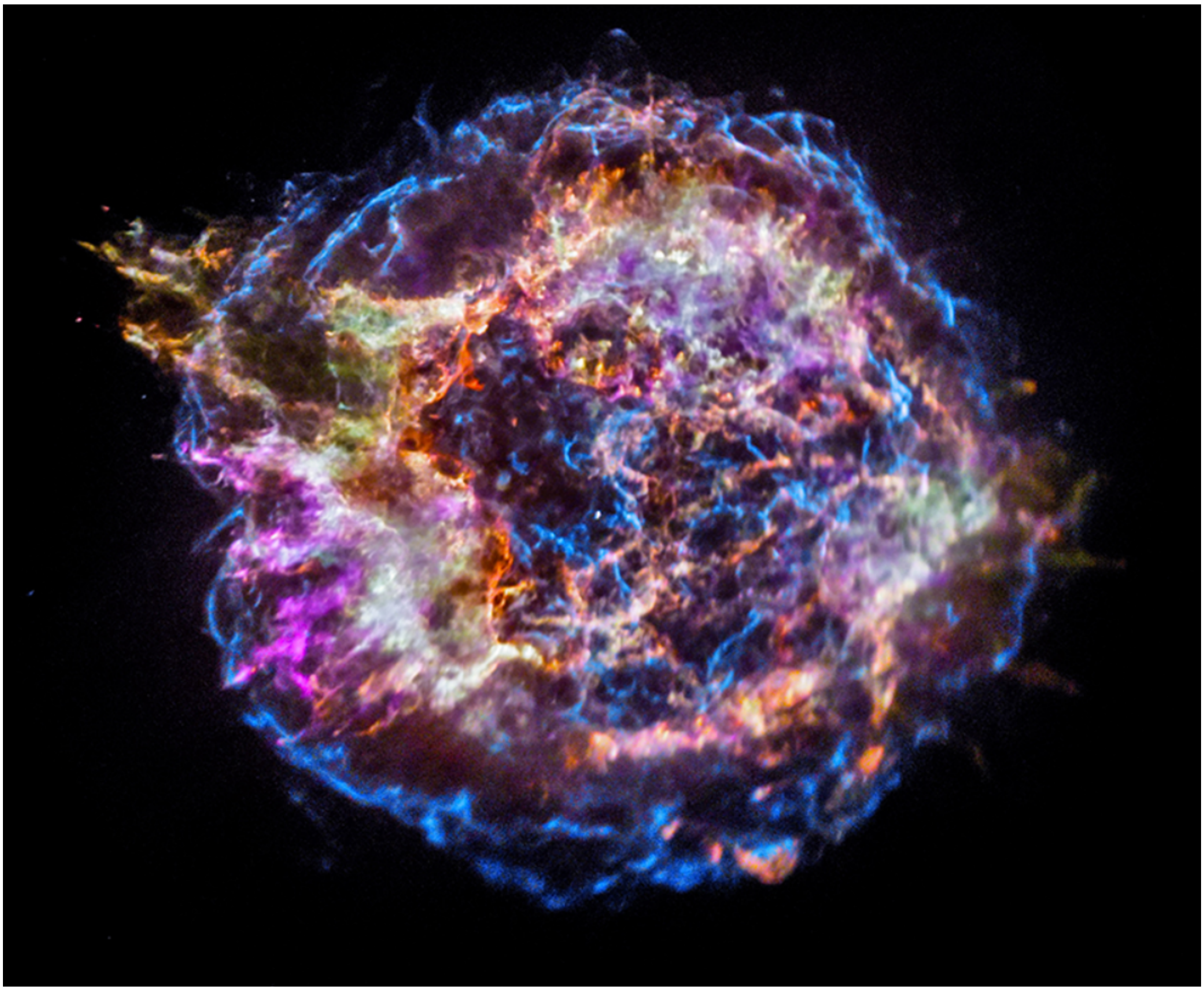

Figure 2.6: X-ray image of the SNR Cassiopeia A produced from data from the Chandra X-ray Observatory. The blue emission surrounding the SNR is nonthermal synchrotron radiation. Apart from this, different colors indicate emission from different elements: Red is silicon, yellow is sulfur, green is calcium, and purple is iron. Credit: NASA/CXC/SAO.

2.6.2 Challenges to the Standard Paradigm

The standard paradigm of CR acceleration in isolated SNRs offers a good explanation for the general characteristics of CRs. Nevertheless, it still struggles to explain some details of the observations. In particular, the standard paradigm was constructed assuming that the spectrum of CRs is well described by a featureless power law over many orders of magnitude up to the knee. As discussed in section 2.2, this is now known to not be the case, as the spectral slopes of different species differ and additional spectral breaks are observed. For example, there is still no generally accepted explanation for the spectral difference between hydrogen and helium, which might require modifications to the assumed acceleration sites or to the particle injection mechanism.

As discussed in Gabici et al. (2019), there are many more challenges to the standard paradigm, which are beyond the scope of this thesis. Still, one problem is of particular relevance for the motivation of my own analysis of a PeVatron candidate: the ability or inability of SNRs to accelerate particles to PeV energies. As CRs with PeV energies are probably still of Galactic origin, SNRs should be able to produce them if they are supposed to explain the origin of Galactic CRs.

A particularly influential criticism of the standard paradigm's ability to explain PeV CRs was put forward by Lagage and Cesarsky (1983). These authors calculated the maximum energy E_{max} which CRs could obtain via DSA at SNR shocks. They based this calculation on the limited lifetime of the remnants which are slowed down by the surrounding ISM and slowly merge into it. For the most optimistic scenario, these authors arrived at $E_{\text{max}} \sim 100\,\text{TeV}$. For a more realistic and less optimistic diffusion scenario, they stated $E_{\text{max}} \sim 10\,\text{TeV}$, two orders of magnitude below the required value.

Similar results are obtained via different approaches (Hillas, 2005). In general, a rough estimate of the maximum energy which a particle can gain via DSA can be found via the Hillas criterion. It requires the acceleration region to be significantly larger than the particle's Larmor radius and is given by (Hillas, 1984)

$$E_{\text{max}} \sim 1.5Z \left(\frac{B_{\text{u}}}{1\,\mu\text{G}}\right)\left(\frac{R_{\text{acc}}}{1\,\text{pc}}\right)\left(\frac{U}{1000\,\text{km}\,\text{s}^{-1}}\right)\text{TeV}, \tag{2.6.1}$$

with Z the particle's charge number, B_{u} the magnetic field just upstream of the shock, R_{acc} the radius of the accelerating source, and U the shock speed. For typical values for an SNR, this gives maximum energies roughly constistent with the values stated above.

In principle, it is theoretically possible to achieve higher energies via an amplification of the magnetic field strength, e.g., via streaming instabilities (Bell et al., 2013). However, the efficiency of this mechanism drops for larger spectral indices of the accelerated particle distribution. Consequently, one would have to assume a slope of 2 or harder to achieve this amplification, thus giving up the fit with the observed CR spectrum which makes DSA attractive in the first place (Gabici et al., 2019).

Besides these theoretical difficulties, there are also severe empirical challenges to the standard paradigm. In particular, as will be discussed in the next chapter, the population of recently discovered Galactic PeVatrons shows no particularly strong spatial correlation with known SNRs.

CHAPTER 3

PeVatrons

> It is not that we propose a theory and Nature may shout NO; rather, we propose a maze of theories, and Nature may shout INCONSISTENT.
>
> Imre Lakatos, The Methodology of Scientific Research Programmes

3.1 Discovery of Galactic PeVatrons

The study of the origin of CRs was drastically changed by the recent discovery of a Galactic population of PeVatron sources which accelerate particles to PeV energies. The spectra of particles accelerated in such sources are frequently modelled as power laws with exponential cutoffs

$$\Phi_{\mathrm{ECPL}} = \Phi_0 \left(\frac{E}{E_0}\right)^{-\alpha} \exp\left(\frac{E}{E_{\mathrm{c}}}\right), \tag{3.1.1}$$

with Φ_{ECPL} the differential particle number per infinitesimal energy interval, Φ_0 the normalization, E_0 some reference energy, α the power law index, and E_{c} the energy of the cutoff. Mathematically speaking, a PeVatron then is a source for which $E_{\mathrm{c}} > 1\,\mathrm{PeV}$.

In practice, PeVatrons are identified via their secondary γ-ray emission, in particular IC radiation and pion decay. As the electromagnetic spectra of these sources reflect the underlying accelerated particle distributions, $E_{\mathrm{c}} > 1\,\mathrm{PeV}$ then translates to a cutoff energy E_{c}^{γ} of the power law describing the γ-rays which satisfies $E_{\mathrm{c}}^{\gamma} \gtrsim 100\,\mathrm{TeV}$. For IC scattering, this can be seen from equation 2.4.7. For a hadronic emission scenario, this is demonstrated, e.g., in Kelner et al. (2006).

The first detection of a PeVatron was reported by HESS Collaboration et al. (2016). For this study, High Energy Stereoscopic System (H.E.S.S.) VHE data from the surroundings of the supermassive black hole Sagittarius A* at the center of the Galaxy was analyzed. The resulting spectrum has no indication of a cutoff up to tens of TeV and was best fit with a power law. Since a strong spatial correlation between the VHE emission and the density of molecular gas is present, the authors argue for a hadronic origin of the emission. Further, the authors suggest Sagittarius A* as the source of the accelerated particles and argue that it could have been more active in the past, possibly explaining the particle flux around the knee of the CR spectrum. Consequently, already the first discovery of a Galactic hadronic PeVatron stands in opposition to the standard paradigm of isolated SNRs.

The actual breakthrough in the study of PeV CRs was then achieved by the demonstration of the existence of a larger number of PeVatrons in the Galaxy. Observations by the High-Altitude Water Cherenkov Observatory (HAWC) published in Abeysekara et al. (2020) already hinted at such a population. In this analysis, the authors detected nine VHE sources above a threshold energy of 56 TeV. Three of these sources are still significant above 100 TeV. Still, their identification as PeVatrons was ambiguous since their spectra indicate cutoffs below 100 TeV.

However, shortly afterwards, the existence of twelve PeVatrons was confirmed by Cao et al. (2021). They lie along the Galactic plane and were detected well above 100 TeV by the Large High Altitude Air Shower Observatory (LHAASO), a new facility designed for the study of CRs and γ-rays. These sources are shown in figure 3.1. The spectra of these sources are well described by log-parabola fits, a common alternative to power law spectra in γ-ray astronomy. Crucially, the importance of the LHAASO result lies in the larger energy threshold and the large number of sources detected, which tripled the number of PeVatron candidates known up to this point.

Regarding the physical nature of the LHAASO sources, one of them is the Crab nebula, a PWN already known to be a leptonic PeVatron at that point (Amenomori et al., 2019). The other sources are extended in nature and are spatially correlated mainly with pulsars and PWNe, but also young massive star clusters, as well as five known SNRs (Cao et al., 2021). In principle, this leaves open the possibility that SNRs contribute to the flux of CRs with energies above 1 PeV. However, this is far from what would be expected in a scenario where the bulk of CRs is produced by these sources even at such high energies. Quite on the contrary, the association of detected PeVatrons with other sources like Sagittarius A*, PWNe, and young star clusters, combined with the unexpected complexity of the CR spectrum, sparked new interest in alternative source scenarios for CRs.

The list of sources presented here is far from comprehensive. In particular, further PeVatrons and PeVatron candidates were discovered by dedicated observations. Most important in the context of this thesis is the H.E.S.S. source J1646−458 (Aharonian et al., 2022), which is associated with the star cluster Wd 1, the object which my analysis is aimed at. It is discussed in further detail in chapter 4.

3.2 Potential Sources

Already up to this point, many different astrophysical objects were suggested as potential PeVatrons. Here, only a brief overview over some of the most frequently discussed ones is given. For completeness, SNRs are also listed since they might contribute to the flux of CRs at PeV energies. On the other hand, supermassive black holes are not listed, as there is only one in our Galaxy. Further, due to their importance for this thesis, the connection between star clusters and PeVatrons is discussed in its own section 3.3.

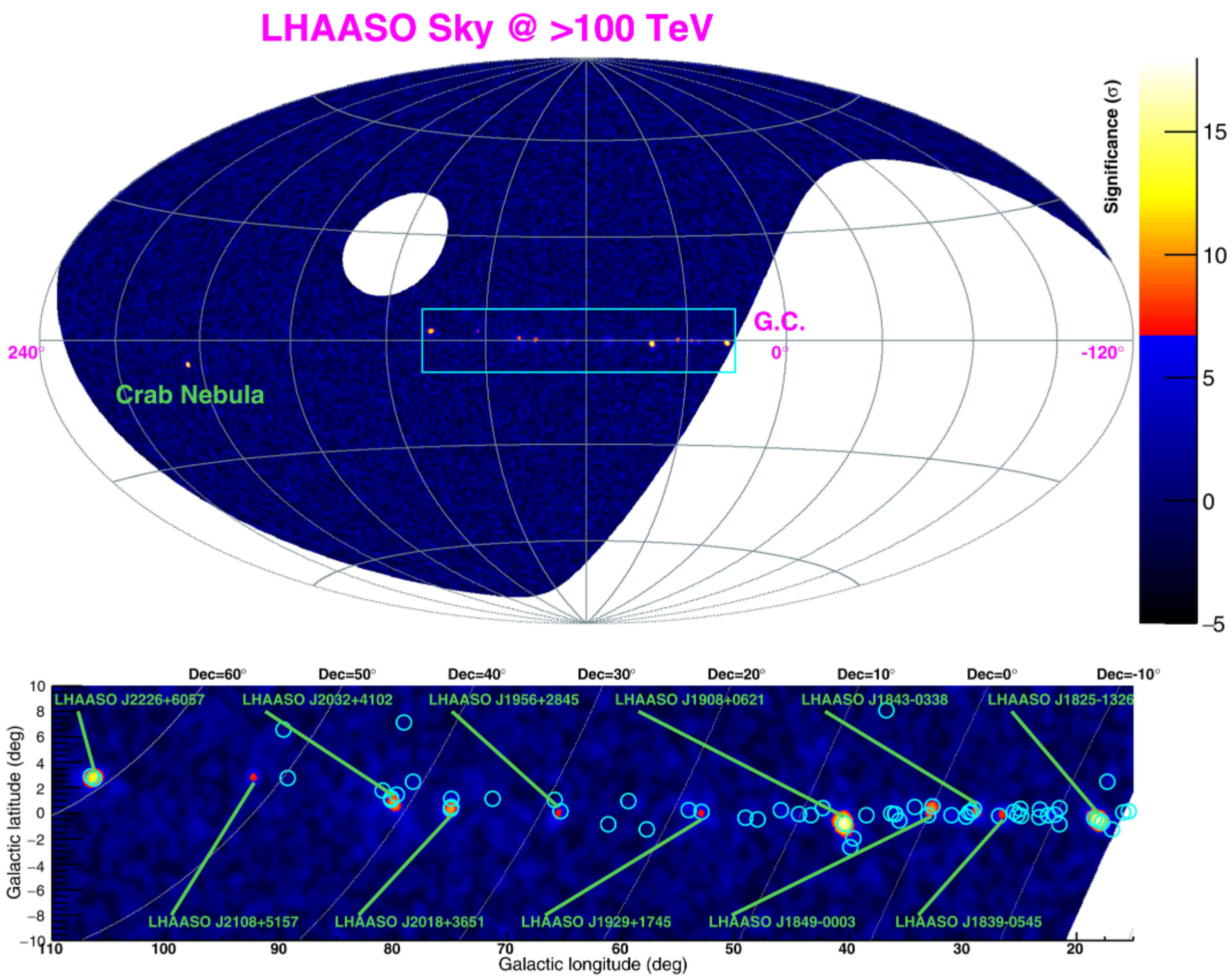

Figure 3.1: *Upper panel:* LHAASO significance map of the sky above 100 TeV in the declination range $-15^\circ < \delta < 75^\circ$. The Crab nebula is marked in green. *Lower panel:* The inset from the upper panel as indicated by the blue contours. Circles mark known VHE γ-ray sources. The remaining eleven LHAASO PeVatrons are marked in green. Taken from Cao et al. (2021).

3.2.1 Supernova Remnants

As discussed before, SNRs as sources of CRs at energies of $\sim 1\,\mathrm{PeV}$ are difficult to justify theoretically and empirically. Still, of the twelve LHAASO sources, five are spatially correlated with known SNRs and one is correlated with an SNR candidate. Further, Tibet ASγ Collaboration et al. (2021) reported the potential detection of an SNR in UHE γ-rays, so above 100 TeV.

It is important to keep in mind that none of these detections is unambiguous. In particular, except for one case, Cao et al. (2021) report other potential counterparts for all of the PeVatron candidates associated with SNRs. In addition, all VHE spectra unambiguously associated with SNRs so far seem to show cutoffs below 100 TeV (Aharonian et al., 2019). Nevertheless, it is important to stay open to the possibility that SNRs might at least contribute to the production of PeV CRs, even if they do not supply a dominant fraction.

Theoretically, one can obtain an acceleration to $\sim 1\,\mathrm{PeV}$ in the first $\approx 100\,\mathrm{yr}$ of SNR evolution for large magnetic fields $B \sim 100\,\mu\mathrm{G}$, high ambient densities $n \sim 10\,\mathrm{cm}^{-3}$, and large shock velocities $U \approx 5000\,\mathrm{km\,s}^{-1}$. These conditions seem rather restrictive and untypical for SNRs. In particular, large ambient densities often lead to smaller shock velocities (Cristofari, 2021). In Cristofari et al. (2020), an estimate for the necessary rate of such supernova explosions is presented if they were to provide the bulk of PeV SNRs. The inferred rate is about one per 10 000 yr. Considering that such a source would produce CRs up to the knee only for about the first 100 yr, it seems hard to actually test such a possibility.

3.2.2 Pulsar Wind Nebulae

As already mentioned, most of the PeVatron candidates detected by LHAASO are spatially correlated with pulsars or PWNe. The prototypical example for a PWN is the Crab nebula, which is the only firmly identified LHAASO PeVatron source and accelerates electrons to energies above 1 PeV (LHAASO Collaboration et al., 2021).

As the name suggests, PWNe are powered by pulsars, i.e., fastly rotating neutron stars. Often, these pulsars have co-rotating magnetic fields with $B \gtrsim 10^{12}\,\mathrm{G}$. The rapid change of a strong magnetic fields induces strong currents of electrons and positrons at the poles of the pulsar. In the form of a highly energetic plasma outflow, these particles collide with the surrounding medium. As a result, a termination shock between the pulsar wind and the surrounding medium is created. These termination shocks can act as sites of efficient particle acceleration, though possibly not only through DSA, but also magnetic reconnection, where particles can acquire energy from rapid changes in the topology of the magnetic field.

Since synchrotron radiation is commonly detected from radio to X-ray energies in the surroundings of PWNe, they are well confirmed to be leptonic accelerators. However, to explain a large share of CRs, the acceleration of hadrons is necessary, too. Possible scenarios for this include the extraction of ions from the surface of the central pulsar or the introduction of hadrons from the surrounding SNR into the wind nebula, though it is currently unclear whether this happens in a sufficient fashion (Mitchell & Gelfand, 2022). Further, the total energy provided by Galactic PWNe might be insufficient to explain the bulk of CRs (Cardillo & Giuliani, 2023).

3.2.3 Microquasars

Microquasars are X-ray binary systems with relativistic jets. Even though there is no association between a known microquasar and a LHAASO source, they were suggested as PeVatron candidates due to their similarities to active galactic nuclei. Powered by supermassive black holes, these objects are often assumed to be the dominant sources of extragalactic CRs.

A number of microquasars is known to emit VHE γ-rays above 1 TeV without an indication of a cutoff (e.g., HAWC Collaboration et al. (2018)), leaving open the possibility that they could contribute to the flux of PeV CRs. However, the number of known Galactic microquasars is not much larger than a dozen. Combined with their lack of association with the so-far known PeVatron candidates, this makes them implausible as dominant sources of PeV CRs in the Galaxy.

3.3 Star Clusters as PeVatron Candidates

Since this thesis focuses on the PeVatron candidate Wd 1, it is justified to grant star clusters as potential PeVatrons their own section. In general, star clusters are gravitationally bound large groups of stars. In particular, my focus lies on young massive star clusters which harbor large numbers of high mass stars with pronounced stellar winds. The cumulative power of these winds might then accelerate CRs to PeV energies. This idea is present in the literature since at least 50 years and has achieved new prominence in the wake of the discovery of Galactic PeVatrons.

Historically, shocks produced by the mass-loss of stars were first proposed as sites of CR acceleration by Casse and Paul (1980). These authors presented a semi-quantitative argument based on local observations of CRs as well as an estimate that stellar winds satisfy the total energy requirement for CRs. Interestingly, they also presented a rough estimate that acceleration at stellar wind termination shocks could reach the PeV range. This finding is also referenced by Lagage and Cesarsky (1983), who argued for the inability of SNRs to accelerate CRs up to the knee.

Nowadays, CR acceleration by massive stars is mainly considered in the context of associations of such stars in OB associations or stellar clusters. The cumulative power of these stars can excavate so-called superbubbles in the ISM which can reach dimensions greater than 100 pc. Intriguingly, these sites provide a number of potential mechanism for particle acceleration: stellar winds, the turbulent interior of the bubble itself, the stellar wind termination shock, or even the combined effects of several SNRs (Parizot et al., 2004). In addition, the acceleration of CRs from stellar winds could also offer an explanation for the enhanced ratio of the neon-22 to neon-20 isotope as compared to the average interstellar value. In the context of the standard isolated SNR paradigm, this phenomenon is not yet understood (Gupta et al., 2020).

In the following, I briefly discuss recent observations which indicate that star clusters might act as PeVatrons, and then focus on acceleration via colliding stellar winds and at the cluster wind termination shock.

3.3.1 Very-high-energy Observations of Star Clusters

Over the course of the last decade, γ-ray emission has been detected in the vicinity of several young stellar clusters. For example, three of the PeVatron candidates identified by Cao et al. (2021) are spatially correlated with young massive star clusters. However, most important in the context of this thesis is the discovery of extended emission surrounding the star cluster Wd 1 using H.E.S.S., as reported by Abramowski et al. (2012). Importantly, a newer analysis of a larger amount of H.E.S.S. data confirmes this finding and finds no significant evidence for a cutoff in the γ-spectrum, leaving open the possibility of the source being a PeVatron (Aharonian et al., 2022). Since Wd 1 is the focus of this thesis, I will discuss it in greater detail in chapter 4.

Several other young star clusters were found to be associated to HE γ-rays based on observations using Fermi LAT. Among these is Wd 1's namesake Westerlund 2. Extended emission surrounding this cluster is reported in Yang et al. (2018). The measured spectrum extends up to 250 GeV, so into the lower end of the VHE band, and it can be explained via hadronic processes from CRs accelerated in the star cluster.

Also discovered by Fermi LAT were γ-rays surrounding the OB association Cygnus OB2 (Ackermann et al., 2011). This association contains about 100 O stars which probably created the Cygnus superbubble. Ackermann et al. (2011) report the detection of a cocoon of HE emission surrounding this superbubble which might stem from secondary emission from CRs. Interestingly, Cygnus OB2 is also one of the stellar clusters associated to a LHAASO source, namely LHAASO J2032+4102 (Cao et al., 2021).

Next, in Saha et al. (2020), the authors report on the study of the star forming region NGC 3604, which contains an OB association. Using ten years of Fermi LAT data, they find a significant HE source close to the OB association which is not explained by any other known γ-ray emitter nearby. Consequently, they prefer an explanation via CR acceleration in the star forming region.

Other detections of γ-ray emission which lend plausibility to massive star associations as CR accelerators are the star forming region W40 (Sun et al., 2020) and the young massive star clusters RSGC 1 (Sun et al., 2020) and NGC 6618 (Liu et al., 2022). A more prominent example, which was detected in VHE γ-rays by H.E.S.S., is the superbubble 30 Dor C which is located in the Large Magellanic Cloud (H. E. S. S. Collaboration et al., 2015).

3.3.2 Shock Acceleration inside Star Clusters

There are two main sites and associated mechanisms of possible particle acceleration in star clusters which are discussed in the following. The first one is DSA at colliding shocks inside the star clusters, while the second one is DSA at the stellar wind termination shocks, far outside of the clusters.

Inside young stellar clusters, shocks are produced mainly through the supersonic stellar winds of massive stars and through the supernova explosions of these massive stars at the end of their lives. Since the radius of these shocks exceeds the average distance between the stars in a cluster in a time shorter than the cluster lifetime, shocks will typically collide, opening up the possibility of repeated accelerations of a particle at multiple shocks.

Analytically, this scenario was considered for two colliding shocks by Vieu et al. (2020). These authors find a self-similar solution to the problem in the test particle limit. The resulting accelerated particle spectrum is similar to the standard E^{-2} slope and does not reach significantly higher energies than 100 TeV. Similarly, Bykov et al. (2013) present a semi-analytical approach to the problem of two colliding shocks, but taking into account nonlinear effects of the accelerated CRs. They find a spectral hardening of the CRs, but still a maximum energy of about 100 TeV.

Presenting quantitative estimates of the cumulative effects of SNRs and stellar winds inside a superbubble, Parizot et al. (2004), too, find a spectral hardening of the accelerated particle distribution. Importantly, however, these authors argue that magnetic field amplification, e.g., by hydrodynamical instabilities, should be more efficient inside superbubbles. This might lead to magnetic field strengths well in excess of 10 µG and therefore enable CRs to reach the knee and potentially even the ankle of the CR spectrum.

3.3.3 Shock Acceleration at the Cluster Wind Termination Shock

The case of DSA at the cluster wind termination shock is considered by Morlino et al. (2021). The geometry of the problem is illustrated by figure 3.2. At the center lies a young massive star cluster with a core radius R_c inside which most of its stars are concentrated. Normally, these clusters contain about 100 to 1000 stars. If the stars are massive, they have typical parameter values of $\dot{M} \sim 10^{-4} M_\odot \mathrm{yr}^{-1}$ for their mass loss due to stellar winds, $v_\mathrm{w} \sim 3000\,\mathrm{km\,s^{-1}}$ for their wind velocity, and $t_\mathrm{b} \sim 10\,\mathrm{Myr}$ for their age.

The cumulative stellar wind of the cluster stars expands into the surrounding ISM and excavates a bubble. This leads to the development of two shocks: a forward shock in the ISM which propagates outward, and a wind termination shock in the wind, which propagates inward relative to the wind. The shocked ISM and the shocked wind are separated by the so-called contact discontinuity at the distance R_cd to the star cluster. Since the shocked ISM is cold and dense in comparison to the wind, it is compressed in a thin layer. Therefore, one can write $R_\mathrm{fs} \approx R_\mathrm{cd}$ for the position of the forward shock.

On the other hand, the position of the wind termination shock can be written as

$$R_\mathrm{S} \approx 48.6 \left(\frac{\dot{M}}{10^{-4} M_\odot \mathrm{yr}^{-1}}\right)^{3/10} \left(\frac{v_\mathrm{w}}{1000\,\mathrm{km\,s^{-1}}}\right)^{1/10} \left(\frac{n_\mathrm{ISM}}{1\,\mathrm{cm^{-3}}}\right)^{-3/10} \left(\frac{t_\mathrm{b}}{10\,\mathrm{Myr}}\right)^{2/5} \mathrm{pc}, \tag{3.3.1}$$

with n_ISM the particle density of the ISM surrounding the star cluster. The shocked wind at $R > R_\mathrm{S}$ moves with velocity u_2, while the unshocked wind at $R < R_\mathrm{S}$ moves with velocity $u_1 = v_\mathrm{w}$.

From this basic consideration of the geometry of the problem, one can already see an advantage of DSA at the cluster wind termination shock: Since the wind termination shock is a reverse shock, the upstream region is completely surrounded by the shock. Different from the forward shocks of SNRs, particle escape directly from the upstream region is impossible.

Indeed, Morlino et al. (2021) find a spectral index of the accelerated particle distribution somewhat steeper than 2, as required by CR observations, and a possible energy of acceler-

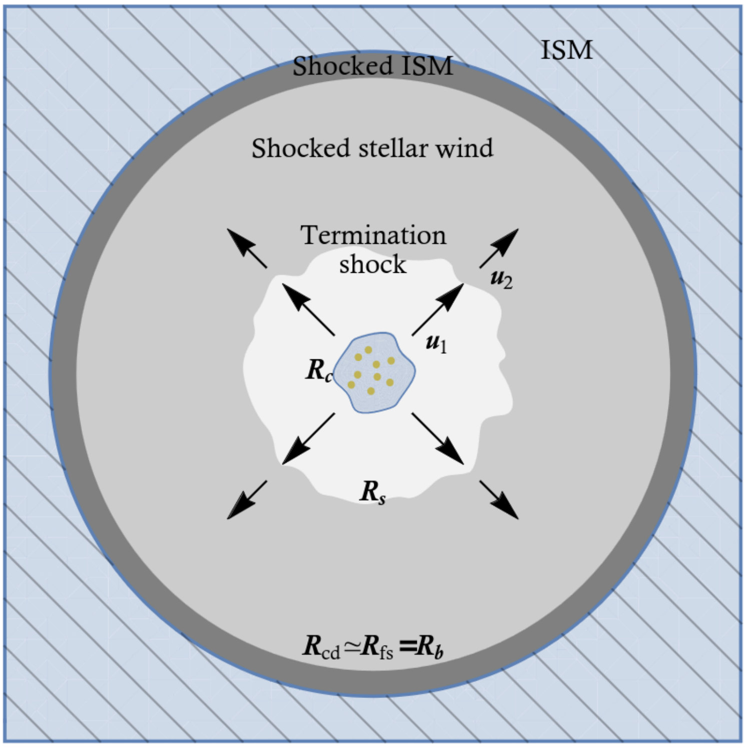

Figure 3.2: Schematic geometry of a star cluster with the shocks produced by its cumulative stellar winds. R_c is the cluster core radius, R_S the radius of the wind termination shock, $R_{cd} \approx R_b$ the position of the contact discontinuity, $R_{fs} =: R_b$ the position of the forward shock, and u_1 and u_2 are the velocities of the unshocked and the shocked wind, respectively. Taken from Morlino et al. (2021).

ated particles above 1 PeV. Specifically, for bright clusters with parameters $\dot{M} \approx 10^{-4} M_\odot \mathrm{yr}^{-1}$, $v_w \approx 3000\,\mathrm{km\,s^{-1}}$, and $t_b \approx 10\,\mathrm{Myr}$, CRs should be able to reach the knee. Further, the derived maximum energy depends almost linearly on $\dot{M}$, meaning that for some clusters with inferred mass loss rates of $\sim 10^{-3} M_\odot \mathrm{yr}^{-1}$, energies of $\sim 10\,\mathrm{PeV}$ should be possible.

3.4 Breaking the Hadronic-leptonic Degeneracy

The often cited aim of the study of PeVatrons is to understand the origin of Galactic CRs with energies at least up to the knee. As described in section 2.3, CRs are mainly hadronic in nature and have only a relatively small leptonic component. Consequently, this raises the question whether a specific source or source population can accelerate hadrons up to the knee or only leptons. Phrased differently, and borrowing the terminology of Cardillo and Giuliani (2023), the question is whether a PeVatron in general, which accelerates some kind of particles to the knee, is also a hadronic PeVatron.

In general, this question is not easy to answer since most PeVatron candidates are identified in the VHE γ-ray bands. In principle, the different secondary emission mechanism in this energy range point to the nature of the source: hadronic for pion decay, leptonic for IC scattering and bremsstrahlung. However, VHE data is frequently degenerate with respect to these two scenarios, i.e., the same data can equally be fitted with hadronic or leptonic emission.

Consequently, additional information is required to argue for one scenario or the other. For example, a spatial correlation of γ-rays with the distribution of cold and dense gas is often invoked as an argument for a hadromic scenario, since the efficiency of the production of pions depends on the density of the target material the CRs can interact with. Alternatively, one can corroborate a leptonic emission scenario via the detection of synchrotron radiation. Since synchrotron radiation from hadrons is highly supressed, this would indicate the presence of accelerated electrons in the source region.

In that regard, a particularly interesting study is the analysis of the superbubble 30 Dor C by Kavanagh et al. (2019). 30 Dor C is not only a PeVatron candidate, as found by H.E.S.S., but it also exhibits a bright X-ray shell of synchrotron emission. In a leptonic emission scenario where the γ-rays stem from IC scattering, the X-ray and the γ-ray spectra are coupled since the underlying electron distribution is the same. The main difference between the two components is that for IC scattering, the target photon field is an additional parameter, and for the synchrotron component, the magnetic field strength is an additional parameter.

This basic idea is well illustrated by figure 3.3, which shows the spectral energy distribution (SED) of 30 Dor C as found in Kavanagh et al. (2019). An SED is a plot of the differential flux of a source's radiation over many orders of magnitude in energy E. Typically, the flux is multiplied with E^2 for better readability and to provide a proxy for the energy flux from the source.

The SED shows VHE energy data collected by H.E.S.S., HE upper limits by Fermi LAT, and X-ray data by the Suzaku X-ray telescope. Different line colors indicate different radiation components in the SED fit: Blue is the synchrotron component, red the leptonic IC component, and black the hybrid component, i.e., IC plus hadronic emission from pion decay. Different line styles indicate different magnetic field strengths and different contributions of the IC component to the γ-rays as indicated in the legend.

The main take away is the following: Looking only at the VHE data, one can see how different combinations of leptonic and hadronic emission can fit the data equally well: The dotted purely leptonic scenario works about as well as the solid line scenario, where the leptonic share is only 10%. This is the degeneracy of the data with respect to these models.

However, now paying attention to the synchrotron radiation, one can see that the IC and the synchrotron component are coupled. This is because the underlying electron distributions are the same one. Crucially, choosing a γ-ray model with a low leptonic share, e.g., 10%, influences the fit to the X-ray data: For a 10% leptonic scenario, corresponding to a lower normalization of the underlying electron distribution, one has to increase the magnetic field strength to 50 μG to preserve an acceptable fit to the synchrotron data. On the other hand, a large share of leptons of 100%, corresponding to a large normalization of the electron distribution, requires a smaller magnetic field of 15 μG.

This way, one can obtain a constraint on the combination of the magnetic field strength and the share of the leptonic emission to the γ-ray flux by analyzing X-ray data from CR accelerators. In the case of Kavanagh et al. (2019), the authors also provide an independent estimate of the

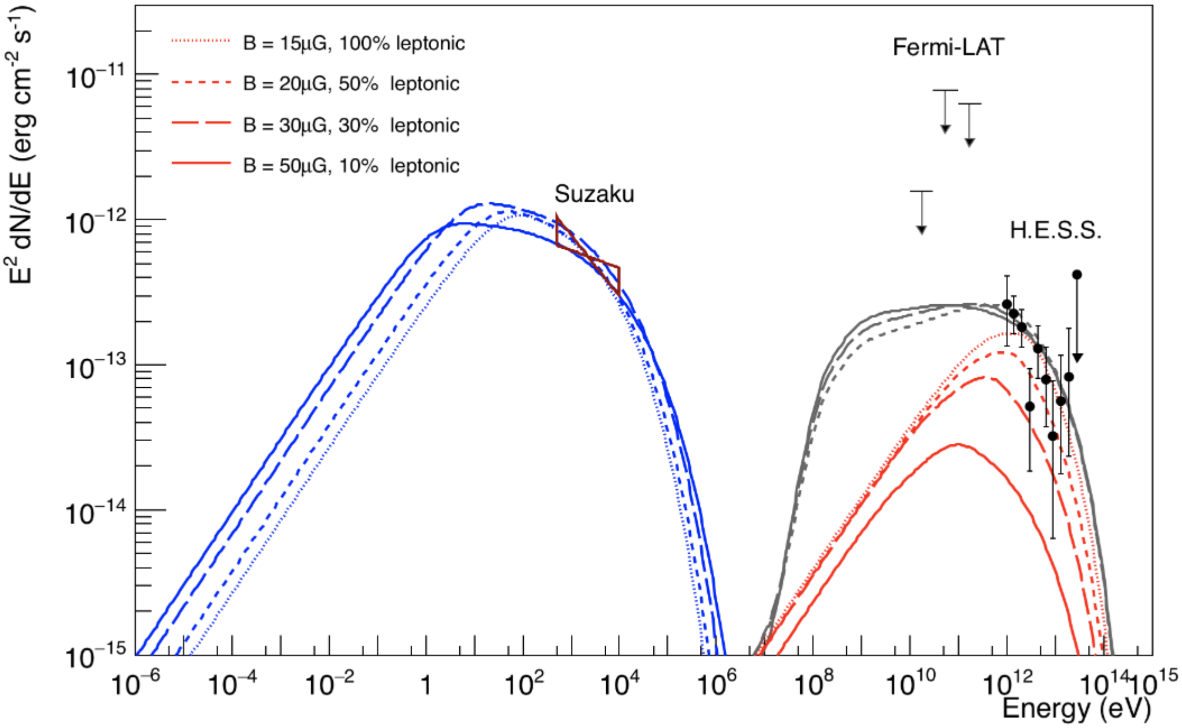

Figure 3.3: SED of 30 Dor C. Blue lines show the fitted synchrotron component, red lines the IC component, and black lines the hybrid component combining IC emission with pion decay. Different line styles indicate different magnetic field strengths and different contributions of the IC component as indicated in the legend. Taken from Kavanagh et al. (2019).

magnetic field via measurements of the width of the synchrotron filaments of 30 Dor C. They obtain $B \lesssim 20\,\mu\mathrm{G}$, which suggests a mainly leptonic origin of the VHE emission.

Relating this back to my own analysis of Wd 1, my goal was to constrain the origin of the VHE emission surrounding this PeVatron candidate. For this, I analyzed eROSITA data in the surroundings of the star clusters to search for synchrotron emission. Similar to the study of Kavanagh et al. (2019) on 30 Dor C, this can then be used for an SED fit from X-rays up to γ-rays and thus provide constraints on the emission scenario and the magnetic field strength.

CHAPTER 4

Westerlund 1

> Wohin kannst du mich noch führen,
> dem längst die Sterne entfacht,
> die Weiten atmen und spüren
> die ganze Tiefe der Nacht?
>
> Gottfried Benn, Wohin

4.1 Basic Overview

The focus of this thesis lies on the PeVatron candidate Westerlund 1 (Wd 1), one of the most massive young star clusters in the Milky Way galaxy. Clark et al. (2005), based on the masses of spectroscopically identified stars in the cluster, derive a lower mass limit of $1.5 \cdot 10^3 M_\odot$ for it. Further, assuming a standard Kroupa (2002) initial stellar mass function, they derive a mass of Wd 1 in excess of $10^5 M_\odot$. Based on this, Wd 1 is often claimed to be the single most massive known young star cluster in the Galaxy.

Historically, Wd 1 was discovered by the Swedish astronomer Bengt Westerlund in 1961. He reported on the discovery of a ”heavily reddened cluster” in the constellation of Ara, ”the Altar”, located in the southern hemisphere (Westerlund, 1961). This reddening is clearly visible in figure 4.1, which shows an optical image of Wd 1. The visible diameter of the cluster is about 3 arcmin (Morales et al., 2013). The reddening is likely caused by dust extinction in the direction of Wd 1 (Westerlund, 1987). Indeed, Wd 1 is located at a right ascension $\alpha_{\mathrm{J2000}} = 16^{\mathrm{h}}47^{\mathrm{m}}02.4^{\mathrm{s}}$ and a declination $\delta_{\mathrm{J2000}} = -45^\circ 51' 07''$ (Tarricq et al., 2021), translating to a longitude $l \approx 339.55^\circ$ and a latitude $b \approx -0.40^\circ$ in Galactic coordinates. Therefore, the cluster is located on the Galactic plane, where dust extinction is the highest. In fact, it is not too far away from the direction of the Galactic center.

Typically, the stars inside Wd 1 are assumed to stem from a single star burst and therefore to have a single age. Most age estimates lie in the range of $3-5$ Myr (Brandner et al., 2008; Clark et al., 2005; Crowther et al., 2006). However, the luminosities of cool supergiants indicate that these might have a different age of $\approx$ 10 Myr, challenging the single-age hypothesis (Beasor et al., 2021).

Figure 4.1: Optical image of Wd 1 taken with the Wide Field Imager on the MPG/ESO 2.2-metre telescope at ESO's La Silla Observatory in Chile. The interstellar reddening of the stars in the cluster is clearly visible. Credit: ESO.

4.1.1 Distance Estimates

Determinations of distances are among the most difficult measurements in astronomy and Wd 1 is no exemption from this. However, obtaining a reliable estimate is important as the distance to the cluster influences its inferred physical parameters, e.g., its extent and luminosity. Previous distance estimates of Wd 1 are somewhat uncertain and have varied over the years, though most of the times they arrive at values between 2 and 5 kpc.

One of the first estimates comes form Westerlund (1987) who determined the spectral types and luminosity classes of cluster member stars and calculated the average distance modulus of nine of them. From this, he arrived at a distance of $\approx$ 5 kpc. Similarly, Piatti et al. (1998) matched isochrones to the color-magnitude diagram of the cluster, but they found a distance of (1.1 ± 0.4) kpc, much smaller than Westerlund (1987).

In a different approach, Kothes and Dougherty (2007) measured the radial velocity of neutral hydrogen gas associated with Wd 1 and compared it to a model of the Galaxy's rotation curve. In the end, they arrive at (3.9 ± 0.7) kpc. In addition, they determine the radial velocity of Wd 1 to be $-(55 \pm 3)\,\mathrm{km\,s^{-1}}$. Consistent with their distance estimate, Clark et al. (2005) obtain a lower limit of 2 kpc based on the non-detection of cluster WR stars in the radio band and an upper limit of 5.5 kpc based on calibrated luminosities of yellow hypergiant stars in Wd 1.

The newest estimations employ parallaxes of cluster members published in the Early Data Release 3 of the Gaia mission. This way, Negueruela et al. (2022) arrive at a distance to Wd 1 of $4.23^{+0.21}_{-0.23}$ kpc and Navarete et al. (2022) arrive at $4.06^{+0.36}_{-0.34}$ kpc.

For the rest of this thesis, I will assume a distance to Wd 1 of 3.9 kpc to be consistent with recent γ-ray studies (Aharonian et al., 2022; Härer et al., 2023). At this distance, the optical diameter of the cluster of 3 arcmin corresponds to a physical diameter of $\approx$ 3.4 pc.

4.1.2 Stellar Population

Wd 1 is frequently studied for its unusual population of high mass stars. In particular, it contains a remarkable number of stars in different intermediate evolutionary stages which are only rarely observed due to their short duration. Over all, this makes Wd 1 a promising target for studying the properties and the evolution of high mass stars and their feedback effects on the galaxy containing them.

The newest census of the stellar population of Wd 1 comes from Clark et al. (2020). These authors find a total number of at least 166 stars with initial masses between 25 and $50 M_\odot$ in the cluster. A large number of these are early type OB stars. In particular, they find Wd 1 to contain more than 100 OB giants and supergiants and 10 OB hypergiants.

Particularly interesting about Wd 1 is its population of stars in short-lived transitional evolutionary stages. In total, Clark et al. (2020) list eleven such stars. First of all, there are four red supergiants, which are post-main sequence stages of high mass stars that will end their lives in core-collapse supernova explosions. Among these red supergiants, Wd 1 contains the star W26. With a radius of $\approx 1550 R_\odot$, it is one of the largest known stars in the Universe.

In addition, Wd 1 contains one luminous blue variable. These rare stars are a late evolutionary stage of massive super- or hypergiants. Even more notably, Wd 1 contains six yellow hypergiant stars. In total, only about twice as many of these stars are known in the entire Milky Way (Clark et al., 2005). Yellow hypergiants are often assumed to be in a transitional post-red supergiant phase of stellar evolution. However, it is noteworthy that the claim of yellow hypergiants in Wd 1 is contested as Beasor et al. (2023) classify these stars as yellow supergiants based on their spectra and luminosities.

Particularly interesting in the context of this thesis is Wd 1's large population of WR stars. In total, Clark et al. (2020) report on at least 24 of these in the cluster, at least 70% of which are bound in binary star systems (Clark et al., 2008). Typical characteristics of WR stars are broad emission lines of ionized helium, carbon, and nitrogen, and a depletion of hydrogen. These stars are often interpreted as post-main sequence massive stars which have shed their hydrogen hulls. Most importantly in the context of PeVatrons, WR stars regularly exhibit pronounced stellar winds with mass loss rates of $\dot{M}_{\mathrm{WR}} \sim 6 \cdot 10^5 M_\odot \mathrm{yr}^{-1}$ and wind velocities of $v_{\mathrm{WR}} \sim 1700\,\mathrm{km\,s^{-1}}$ (Leitherer et al., 1992).

From this, the wind power of a typical WR star can be calculated according to

$$L_\mathrm{w} = \frac{1}{2}\dot{M}v_\mathrm{w}^2, \tag{4.1.1}$$

which yields a value of $\sim 5 \cdot 10^{37}\,\mathrm{erg\,s^{-1}}$. Since WR stars are expected to dominate the wind output of the cluster (Muno et al., 2006), the total cluster wind power is simply the sum of the wind powers of the 24 WR stars. This yields a mechanical output in excess of $10^{39}\,\mathrm{erg\,s^{-1}}$.

Such a strong cluster wind suggests that Wd 1 should produce a pronounced cluster wind termination shock, as discussed in section 3.3. Crucially, this might serve as a site of particle acceleration. Indeed, Kothes and Dougherty (2007) find a bubble-like structure in the neutral hydrogen gas surrounding Wd 1 which might stem from a cavity created by the cluster wind. Its diameter is about 50 pc at a distance of 3.9 kpc.

Finally, Wd 1 contains one magnetar called CXOU 164710.2−455216 (Clark et al., 2008). Magnetars are neutron stars with extremely large magnetic field strengths above 10^{14} G. Interestingly, this magnetar is the only known compact object inside the star cluster. Even more, it is the only known remnant of a supernova explosion in Wd 1. In particular, no SNRs are found to be associated with the cluster. Still, this might not be regarded as surprising, since Wd 1 seems to have cleared away the surrounding ISM, removing the dense medium necessary for an SNR to be visible in radio or X-ray observations (Muno et al., 2006).

4.2 γ-ray Observations

In the context of this study, Wd 1 is interesting because of its spatial association with the VHE γ-ray source J1646−458. This extended sources was first detected by H.E.S.S., as reported in Abramowski et al. (2012). Using 33.8 h of H.E.S.S. data, these authors find an extended VHE γ-ray source with a radius of $\approx 0.5^\circ$, as can be seen in figure 4.2. Wd 1, marked with a green star, lies very close to the center of the VHE emission, marked with a white cross.

In general, the source morphology of J1646−458 is rather complex with two particularly bright regions: Region A to the north and region B to the south. Nevertheless, Abramowski et al. (2012) find no significant indication for an energy dependence of the morphology of the emission region. Note that the particularly bright source to the south-west, HESS J1640−465, is most likely not associated with J1646−458. The impression that it seems to contaminate the spectral analysis region, marked with a dashed white line in figure 4.2, is mainly an artifact of the smoothing of the image.

In this study, the authors do not perform fits to the underlying leptonic or hadronic particle distribution of J1646−458, but only to the secondary γ-ray spectrum. Using a standard power law shape

$$\frac{\mathrm{d}N}{\mathrm{d}E} = \Phi_0 \left(\frac{E}{1\,\mathrm{TeV}}\right)^{-\Gamma}, \tag{4.2.1}$$

they arrive at $\Gamma = 2.19 \pm 0.08_{\mathrm{stat}} \pm 0.20_{\mathrm{sys}}$ and $\Phi_0 = (9.0 \pm 1.4_{\mathrm{stat}} \pm 1.8_{\mathrm{sys}}) \cdot 10^{-12}\,\mathrm{TeV}^{-1}\,\mathrm{cm}^{-2}\,\mathrm{s}^{-1}$. In total, they find a VHE luminosity between 0.1 TeV and 100 TeV of $L_\gamma = 1.9 \cdot 10^{35}\,\mathrm{erg\,s}^{-1}$ for a distance of 4.3 kpc.

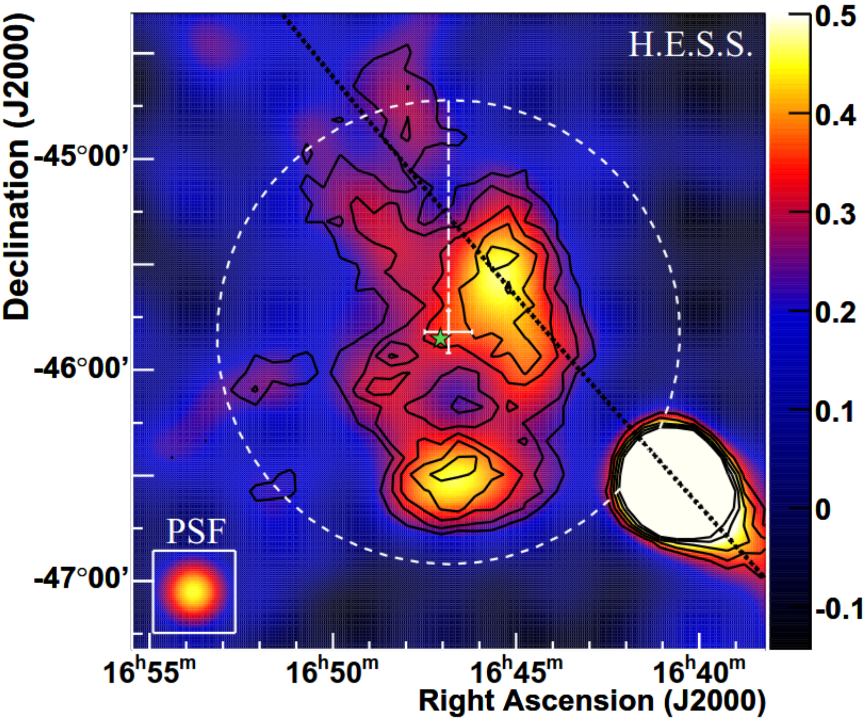

Figure 4.2: H.E.S.S. excess map around Wd 1 in units of γ-ray events per arcmin^2, smoothed with a Gaussian kernel with variance 0.12°. Black lines are 4σ to 8σ significance contours. The position of Wd 1 is marked with a green stara and the Galactic plane with a dashed black line. The inset to the bottom left is the size of a comparable H.E.S.S. point spread function. The dotted white circle with a radius of 1.1° marks the region chosen for the spectral analysis. The bright source to the south-west is HESS J1640−465. Taken from Abramowski et al. (2012).

A more detailed analysis is presented by Aharonian et al. (2022) who take advantage of newer H.E.S.S. observations with a total observing time of 164.2 h. In general, these authors, too, find a complex morphology, as can be seen in figure 4.3. The diameter of the emission region is about 1° and while Wd 1 lies close to the center, the emission is not peaked at its position, but rather shell-like in shape. As before, these authors notice the presence of the two bright emission regions A and B, as well as a third region C to the east of Wd 1. Further, they extracted radial profiles of the emission region in different energy bands and for different radial directions from the white circle seen in figure 4.3. These profiles are consistent between all bands and directions tested and confirm the energy-independent morphology of J1646−458. Further, they confirm the shell-like shape of the emission region with an emission peak at a distance of $\approx 0.5^\circ$ from the center, corresponding to 34 pc at a distance of 3.9 kpc.

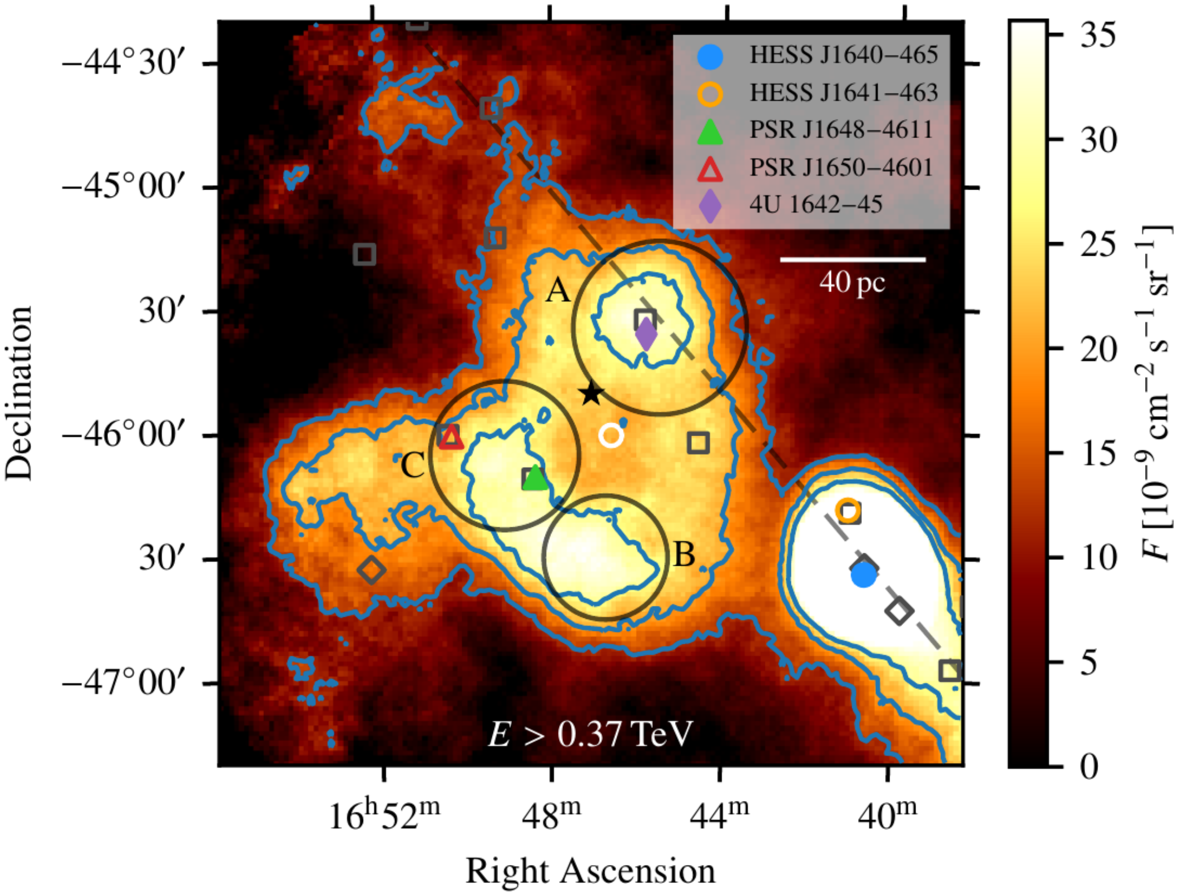

Figure 4.3: H.E.S.S. flux map around Wd 1 above an energy threshold of 0.37 TeV. Blue contour lines are at flux levels of 12.5, 20, and $27.5 \cdot 10^{-9}\,\mathrm{cm}^{-2}\,\mathrm{s}^{-1}\,\mathrm{sr}^{-1}$. The position of Wd 1 is marked with a black stara and the Galactic plane with a grey dashed line. Colored symbols mark sources as indicated in the legend. Grey symbols mark sources found in the Fermi LAT 4FGL-DR2 source catalog. The white line below the legend indicates the angular extent of 40 pc at a distance of 3.9 kpc. The white circle marks the position used as the center for the extraction of radial profiles. Taken from Aharonian et al. (2022).

Further, Aharonian et al. (2022) also present a spectral analysis of J1646−458. For this, they first defined 16 rectangular subregions with an angular extent of $0.45^\circ \times 0.45^\circ$ and performed individual power law fits according to equation 4.2.1 to each of them. The spectra obtained this way are similar to each other and in fact, the power law indices are consistent except for one outlier with a significance of $\approx 4\sigma$. Summed up, this result strengthens the assumption of an energy-independent morphology.

These individual power law fits can be seen in figure 4.4 in blue. Their sum is indicated by a dashed blue line. However, Aharonian et al. (2022) find a standard power law to not provide a good description of the summed up emission of all regions. Instead, they employ an exponential cutoff power law

$$\frac{\mathrm{d}N}{\mathrm{d}E} = \Phi_0 \left(\frac{E}{1\,\mathrm{TeV}}\right)^{-\Gamma} \exp\left(-\frac{E}{E_\mathrm{c}}\right), \tag{4.2.2}$$

shown in orange in figure 4.4. Here, E_c is the cutoff energy of the model.

This fit results in $\Gamma = (2.30 \pm 0.04)$, $\Phi_0 = (1.00 \pm 0.03) \cdot 10^{-11}\,\mathrm{TeV}^{-1}\,\mathrm{cm}^{-2}\,\mathrm{s}^{-1}$, and $E_\mathrm{c} = 44^{+17}_{-11}\,\mathrm{TeV}$. This amounts to a VHE luminosity between 0.37 TeV and 100 TeV of $L_\gamma = 9 \cdot 10^{34}\,\mathrm{erg\,s^{-1}}$ at a distance of 3.9 pc. Importantly, Aharonian et al. (2022) note that the highest energy flux points with their large uncertainties do not provide a clear indication for the presence of a cutoff. Following this line of reasoning, the energy spectrum might extend well beyond 100 TeV, as required for a PeVatron.

4.2.1 Possible Sources of the Very-high-energy Emission

Both Abramowski et al. (2012) and Aharonian et al. (2022) discuss astrophysical sources near Wd 1 as potential sources of the VHE γ-ray emission of J1646−458. Among these are the low mass X-ray binary (LMXB) GX 340+0, two nearby pulsars, the magnetar CXOU 164710.2−455216, and the star cluster Wd 1 itself.

First of all, the LMXB GX340+0, also called 4U 1642−45, is located to the north-west of Wd 1. Its location inside emission region A is marked by a purple diamond in figure 4.3. The source is a neutron star which accretes matter from a low mass companion star. Both Abramowski et al. (2012) and Aharonian et al. (2022) exclude this source as the origin of the VHE based on three arguments: 1. LMXBs are not known to emit VHE γ-rays. 2. At the distance of GX 340+0 of 8.5 to 11.8 kpc, J1646−458 would have an extent of 320 to 450 pc, way larger than what would be expected from particle acceleration in the jet of an accreting neutron star. 3. Emission from LMXBs typically shows temporal variation which is not found in the VHE data.

Second, the magnetar CXOU 164710.2−455216 is probably located inside Wd 1. Its spin-down power is estimated to be $\approx 3 \cdot 10^{31}\,\mathrm{erg\,s^{-1}}$ and therefore insufficient to explain the VHE luminosity of $L_\gamma \sim 1 \cdot 10^{35}\,\mathrm{erg\,s^{-1}}$. While the magnetar's X-ray luminosity is reported to be $\approx 3 \cdot 10^{33}\,\mathrm{erg\,s^{-1}}$, indicating another source of energy in the object, this still falls short of the energy requirement.

The positions of two pulsars, PSR J1648−4611 and PSR J1650−4601, are marked in figure 4.3 with a green and a red triangle, respectively. They are located in emission region C. As discussed in section 3.2, pulsars are known to be VHE sources. In principle, the spin-down power of the two pulsars satisfies the energy requirement, as PSR J1648−4611 has $\approx 2.1 \cdot 10^{35}\,\mathrm{erg\,s^{-1}}$ and PSR J1650−4601 has $\approx 2.9 \cdot 10^{35}\,\mathrm{erg\,s^{-1}}$. However, explaining J1646−458 this way would require a remarkably high energy conversion efficiency close to 100%.

In addition, the γ-ray emission detected from the pulsars is variable and has a steep spectrum above 10 GeV. Finally, the large size of J1646−458 speaks against the pulsars as sources just like the lack of energy-dependent morphology does: Pulsars are expected to be leptonic emitters and electrons are subject to considerable cooling losses from synchrotron radiation, implying an energy dependent shape of the emission region.

Finally, Abramowski et al. (2012) consider Wd 1 to be the most likely source of J1646−458 in a single source scenario. The star cluster coincides with the center of the emission region

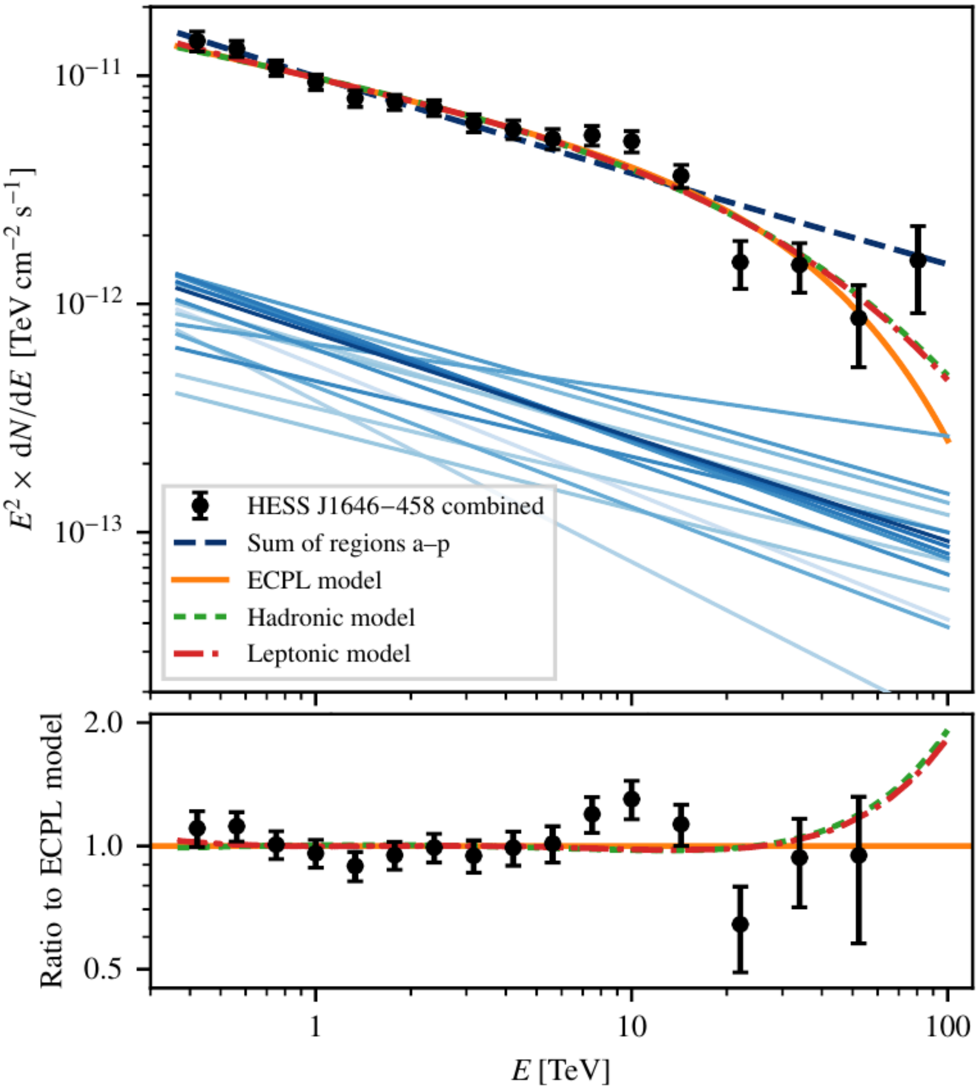

Figure 4.4: *Upper panel:* Spectrum of J1646−458 as measured by H.E.S.S.. Solid blue lines depict power law fits to the 16 individual regions as described in the text. Darker shades indicate a smaller distance to Wd 1. The dashed blue line is the sum of these regional contributions. The orange, green, and red lines indicate an exponential cutoff power law fit, a hadronic model fit, and a leptonic model fit, respectively. *Lower panel:* Ratio of the data points and the model values to the exponential cutoff power law model values. Note that the highest energy data point is not visible since it is outside the plot boundary. Taken from Aharonian et al. (2022).

and fulfills the energy requirement. Using a cluster evolution model, Abramowski et al. (2012) estimate the energy dissipated by Wd 1 over its lifetime to be $\approx 3 \cdot 10^{53}$ erg, explaining the energy of CRs of $\approx 2.1 \cdot 10^{50}$ erg in a hadronic scenario with a conversion factor of 0.1%. In addition, the authors also note the possibility of a multi-source scenario. In this case, one of the bright subregions could stem from a PWN powered by PSR J1648−4611.

Aharonian et al. (2022), too, conclude that Wd 1 is the most likely source of J1646−458. In principle, the energy requirement is met by past supernovae in the cluster, wind-wind interactions inside the cluster, acceleration in turbulences inside a superbubble, or acceleration at the cluster wind termination shock. Among these ideas, the problem with SNRs is that none are observed around Wd 1. This might be expected given the low gas density surrounding it, but it makes a confirmation of this hypothesis difficult. Further, the estimated extent of a superbubble around Wd 1 exceeds the extent of J1646−458, disfavouring this hypothesis. Therefore, the preferred acceleration sites are wind-wind interactions inside the cluster and the cluster wind termination shock

4.2.2 Very-high-energy Emission Scenarios

Since the aim of this thesis is the derivation of new constraints on the emission scenario of J1646−458, it makes sense to discuss the existing constraints. First of all, Abramowski et al. (2012) favor a hadronic emission scenario based on the source morphology and the energetic argument provided above. In particular, these authors argue that the large cooling losses of energy in electrons would prevent them from reaching the extent observed in the H.E.S.S. data. This argument certainly holds for CR acceleration inside the cluster itself. Crucially, however, Abramowski et al. (2012) do not consider the possibility of particle acceleration at the cluster wind termination shock, which provides a natural explanation for the source morphology.

Aharonian et al. (2022) provide a more extensive discussion of the potential emission scenarios. In particular, they do not only offer an exponential power law fit to the γ-ray spectrum, but also fits of underlying electron and proton particle distributions. For this, they used the `Naima` fitting code. Just like for the spectrum itself, the particle distributions are assumed to be described by exponential cutoff power laws according to equation 4.2.2.

For a hadronic scenario, they arrive at $\Phi_0^{\mathrm{p}} = (1.28 \pm 0.17) \cdot 10^{38}\,\mathrm{eV}^{-1}$, $\Gamma = (2.33 \pm 0.06)$, and $E_{\mathrm{c}} = 400^{+250}_{-130}\,\mathrm{TeV}$. Note that the dimension of the normalization is different than before since it refers to a particle distribution, not a photon spectrum. The fit can be seen in figure 4.4 in green. Importantly, this fit assumes a distance to the source of 3.9 kpc and a density of target material for pion production of $1\,\mathrm{cm}^{-3}$. The required energy in protons in this scenario is $W_{\mathrm{p}} = 6 \cdot 10^{51}$ erg.

For obtaining additional constraints on the hadronic scenario, Aharonian et al. (2022) also compare HI and CO data to the VHE map, tracing neutral hydrogen and molecular gas, respectively. This would indicate the presence of target material for the production of pions. Interestingly, they find no clear correlation between the target material and the VHE flux. In fact, the particularly bright emission regions A, B, and C seem to contain a particularly small amount of gas, speaking against a hadronic scenario.

Similarly, Aharonian et al. (2022) also fitted an electron distribution to the VHE spectrum.

They arrive at $\Phi_0^{\mathrm{e}} = (4.7 \pm 0.5) \cdot 10^{35}\,\mathrm{eV}^{-1}$, $\Gamma = (2.97 \pm 0.07)$, and $E_{\mathrm{c}} = 180^{+200}_{-70}\,\mathrm{TeV}$. As indicated by the red line in figure 4.4, the fit itself is hard to distinguish from the hadronic one. As target photon fields for IC scattering in the leptonic scenario, Aharonian et al. (2022) assume the CMB, diffuse infrared emission, diffuse optical light, and the radiation field of Wd 1 itself. The minimum required power in electrons for this scenario is $W_{\mathrm{e}} = 4.1 \cdot 10^{35}\,\mathrm{erg\,s^{-1}}$.

The leptonic scenario is subject to constraints from other wavelengths than γ-rays due to the expected production of synchrotron radiation. To this end, Aharonian et al. (2022) use archival data from the Planck satellite measured at 30 GHz. The inferred intensity around Wd 1 at this frequency is $0.55\,\mathrm{MJy\,sr^{-1}}$, resulting in an upper limit on the magnetic field strength of 10 μG.

Overall, Aharonian et al. (2022) discuss the feasibility of a leptonic and a hadronic scenario for two different acceleration sites: First, if particles are accelerated inside Wd 1 itself, the hadronic scenario is preferred. The main reason is that electrons are expected to cool down to quickly to reach the observed extent of J1646−458. In particular, leptonic emission should peak at the site of acceleration and this is not observed in this scenario. On the other hand, protons are transported more efficiently and their emission morphology could produce the observed shell-like shape for a suitable distribution of target gas. However, this scenario suffers from the lack of observed correlation with HI and CO data.

Second, particle acceleration at the cluster wind termination shock leaves open the possibility of a leptonic scenario since it provides a natural explanation for the shell-like source morphology. In fact, in a theoretical investigation of different source morphologies for different emission scenarios, Bhadra et al. (2022) find the observations to agree with acceleration at the cluster wind termination shock.

Up to this point, the most detailed analysis of the potential emission scenarios for acceleration at the cluster wind termination shock comes from Härer et al. (2023). These authors estimate key parameters of Wd 1 starting from a toy model of the star cluster populated via an initial mass function. They arrive at a cluster wind power of $L_{\mathrm{w}} \sim 10^{39}\,\mathrm{erg\,s^{-1}}$ and a position of the termination shock 20.4 pc away from the cluster. Interestingly, this corresponds to 0.3° at a distance of 3.9 kpc, coinciding with the distance of maximum flux in the data of Aharonian et al. (2022).

Importantly, Härer et al. (2023) also estimate the magnetic field strength in the acceleration region B_{acc}. Using Hillas' criterion (equation 2.6.1), they arrive at a lower limit on the magnetic field of 0.7 μG in a leptonic scenario and 3 μG in a hadronic scenario. Further, requiring a strong shock with a wind speed greater than the ambient Alfvén Mach number leads to an upper limit on the magnetic field of 4.5 μG, in agreement with the limit of Aharonian et al. (2022) using Planck data. Overall, this means $0.7\,\mu\mathrm{G} < B_{\mathrm{acc}} < 4.5\,\mu\mathrm{G}$.

Turning now to the hadronic scenario, Härer et al. (2023) find that for acceleration at the cluster wind termination shock, protons are transported too quickly to explain the observed morphology. Either advectively or diffusively, they are expected to fill the entire cluster superbubble in less than the cluster lifetime. In addition, a spectral fit to the H.E.S.S. data using a hadronic model yields a too high energy required in protons, corresponding to at least 26% of the cluster wind power.

On the other hand, since electrons cool more efficiently, they are transported more inefficiently. This makes it easier to reproduce the observed shell-like morphology in the case of acceleration of electrons at the wind termination shock. In addition, a leptonic spectral fit requires a conversion efficiency of the wind power of only up to 0.28%, depending on the precise assumptions. On a final note, this electron distribution is expected to have a cutoff at $E_c^e \approx 170$ TeV from the requirement of the equality of cooling and acceleration times, assuming a magnetic field strength of 2 μG.

To sum up, the preferred emission scenario seems to be a leptonic one at the cluster wind termination shock. This is based on the morphology of J1646−458, the energetic requirements of the different scenarios, and the lack of correlation between VHE and HI and CO data. However, as noted in Aharonian et al. (2022), such a scenario is subject to constraints from synchrotron emission. This is precisely where the aim of this thesis lies: In obtaining constraints on the X-ray synchrotron emission around Wd 1 using eROSITA.

4.2.3 High-energy γ-ray Observations

Apart from VHE γ-rays, Wd 1 was also observed in HE γ-rays by Fermi LAT. The results of the analysis of this data are reported by Ohm et al. (2013). These authors find an extended HE γ-ray source, called J1651.6−4621, about 1° south of the cluster. Note that this is well beyond the emission maximum of the J1646−459 shell at a cluster distance of about 0.5°. This complex source morphology leads the authors to consider 1. a scenario in which the HE emission stems from a PWN, and 2. a hadronic scenario, in which protons diffuse from the cluster to the observed emission region.

Interestingly, Ohm et al. (2013) also provide upper limits on the HE flux of J1646−458 in a region given by the VHE template used by Abramowski et al. (2012). This upper limit is given in black in figure 4.5. In the case of the dashed line, emission from J1651.6−4621 is included in the upper limit, while it is excluded in the case of the solid line.

4.3 X-ray Observations

X-ray observations of the region of J1646−458 could provide additional constraints on the VHE emission scenario due to the potential detection of synchrotron radiation. Unfortunately, such studies do not seem to be present in the literature. However, some authors studied the cluster Wd 1 itself using X-ray telescopes. This might help with understanding the physics of J1646−458, if acceleration happens inside the star cluster itself. In addition, it offers information on the stellar population and the stellar winds inside the cluster. Specifically, young star clusters are expected to produce X-rays through 1. the magnetic activity of young stellar objects, 2. shocks in the stellar winds of OB stars, 3. colliding winds of OB stars and WR stars, and 4. compact objects, e.g., magnetars and X-ray binaries (Clark et al., 2005).

The first study of the diffuse X-ray emission of Wd 1 comes from Muno et al. (2006). These authors used 60 ks of observations of the stellar cluster with the Chandra X-ray Observatory. After subtracting point sources, they find extended diffuse emission with a half-width at half-maximum of ≈ 25 arcsec, consistent with the distribution of stars in the cluster reported by Clark et al. (2005). Interestingly, this diffuse emission of Wd 1 extends up to at least 5 arcmin

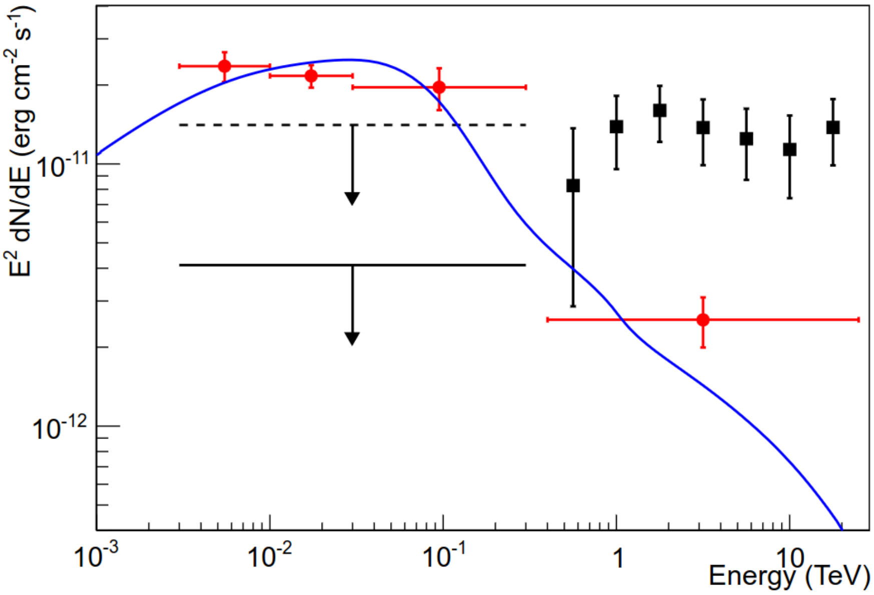

Figure 4.5: HE spectrum of FGL J1651.6−4621 in red, with TeV emission estimated as described in Ohm et al. (2013). Black points give the spectrum of J1646−458 as measured by Abramowski et al. (2012). The upper limits were determined inside the template given by the same study. For the dashed upper limit, J1651.6−4621 is included, while for the solid one it is excluded. The blue line gives an IC model in a PWN scenario. Taken from Ohm et al. (2013).

from the cluster center.

Further, these authors extracted spectra for four regions in the energy band from 2 to 8 keV. The regions are a circle from the cluster center up to a distance of 1 arcmin as well as three annuli of radii $1 - 2$ arcmin, $2 - 3.5$ arcmin, and $3.5 - 5$ arcmin. The resulting spectra can be seen in figure 4.6. They were fitted using the `Xspec` spectral fitting software.

Muno et al. (2006) find that these spectra are equally well fitted by a model with two thermal equilibrium emission components and by a model with a thermal and a nonthermal power law component. Either of the two employed models contains an astrophysical plasma emission code (APEC) component with a temperature of ≈ 0.7 keV in the two innermost regions and ≈ 1 keV in the second outermost region. The metal abundance of this component is fixed to $2Z_\odot$, with $Z_\odot$ the Solar abundance, since it is poorly constrained. The contribution of this component to the overall flux decreases outwards from 15% in the central region and becomes undetectable in the outermost annulus.

Interestingly, the rest of the emission can either be fitted with an additional hotter APEC component or a nonthermal power law component. For the thermal component, the temperature varies between 3.2 keV and 11 keV, depending on the annulus. The main reason for the degeneracy between the models is the non-detection of a helium-like iron emission like around 6.7 keV expected from a hot plasma. Consequently, for the hot APEC component, the metal abundance would have to be rather low, below $\approx 0.5Z_\odot$. The total luminosity between 2 and

8 keV inferred for a distance to Wd 1 of 5 kpc is $(3 \pm 1) \cdot 10^{34}\,\mathrm{erg\,s^{-1}}$.

Next, Muno et al. (2006) discuss potential sources of the observed diffuse X-ray emission. While they find stellar winds inside the cluster to fulfill the energy requirement with an expected luminosity in X-rays of about $3 \cdot 10^{34}\,\mathrm{erg\,s^{-1}}$, they do not predict the observed extended diffuse halo out to a radius of $\approx$ 5 arcmin. In particular, X-ray emission from stellar winds is expected to be concentrated inside the cluster. Consequently, the energy requirement remains problematic on closer inspection since the observed X-ray luminosity of the cluster inside the central 2 arcmin falls short of the predicted value.

Finally, Muno et al. (2006) consider an explanation via nonthermal emission from accelerated

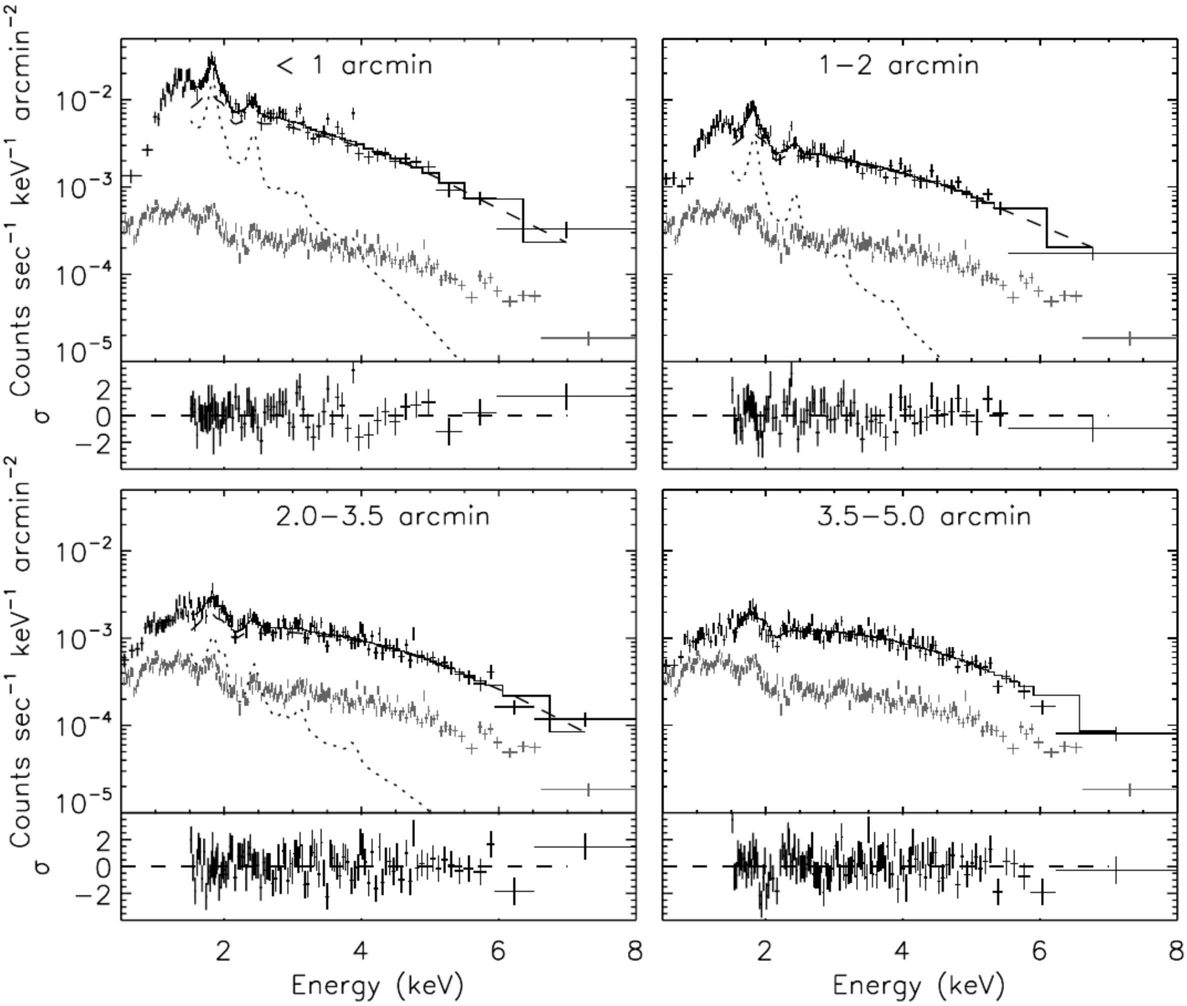

Figure 4.6: Diffuse X-ray emission spectra for four circular regions around Wd 1, as measured by Chandra. The spectra are still convolved with the telescope's response function. Grey data points indicate background emission expected from the Galactic plane. The overall model used to fit the data is given as a solid black line. The dotted line indicates the thermal component of the model, the dashed line the nonthermal component. Taken from Muno et al. (2006).

particles. These could be transported away from the cluster, explaining the extent of the X-ray emission. For the mechanism producing the secondary emission, these authors prefer IC scattering over synchrotron radiation, since the latter would require an unusually strong magnetic field of $\gtrsim 400\,\mu\mathrm{G}$.

To put these results into context, a newer analysis of the diffuse X-ray emission from Wd 1 was performed by Kavanagh et al. (2011). These authors employed 48 ks of observations with the X-ray Multi-mirror Newton (XMM Newton) telescope. An image of Wd 1 as obtained by these authors is given in figure 4.7. In the left panel, stray light contamination from the nearby LMXB GX 340+0 is visible to the north-west. In the right panel, several point sources are visible inside the cluster, most notably the magnetar CXOU 164710.2−455216 in its south-east.

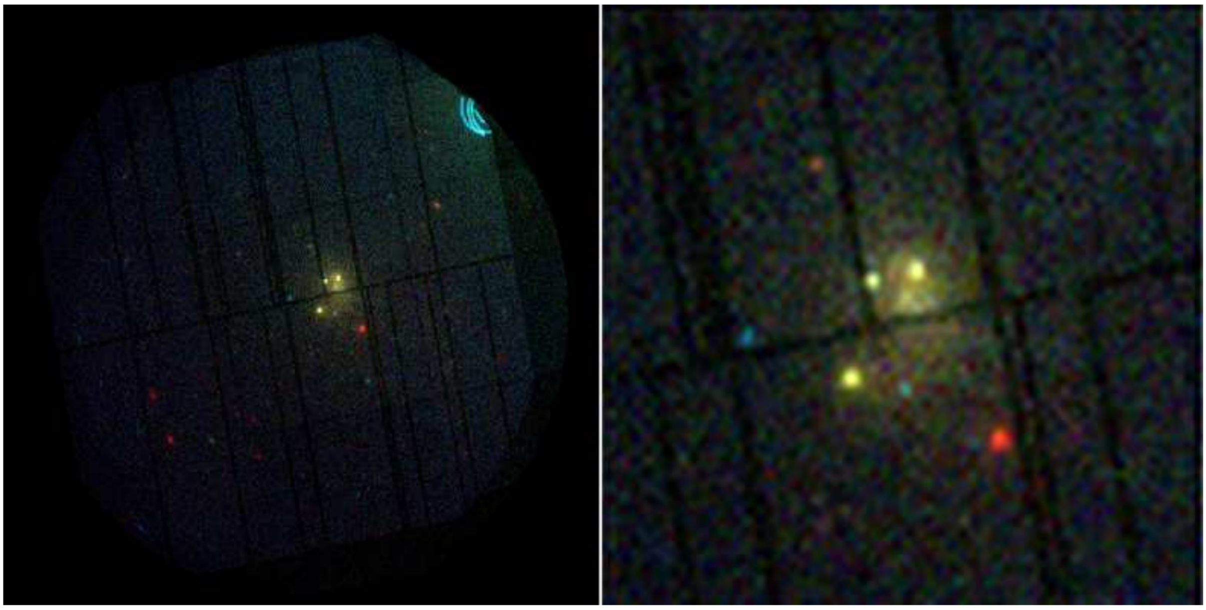

Figure 4.7: XMM Newton images of Wd 1 and its surroundings. The red color corresponds to the $0.3 - 2$ keV band, green to $2 - 4.5$ keV, and blue to $4.5 - 10$ keV. *Left:* The full field of view with a diameter of ≈ 30 arcmin. Visible to the nort-west is stray light contamination from the LMXB GX 340+0. *Right:* Closer view of Wd 1 with an extent of 5 arcmin × 5 arcmin. The bright soft source to the south-west is a foreground star. The bright source in the south-east of the cluster is the magnetar CXOU 164710.2−455216. Taken from Kavanagh et al. (2011).

For their spectral analysis, Kavanagh et al. (2011) only used the two MOS cameras of the XMM Newton telescope, since detector gaps of the PN camera masked parts of Wd 1. After masking point sources and subtracting a suitable background of similar stray light contamination as the cluster itself, these authors achieve fits consistent with those of Muno et al. (2006) in regions identical to the ones from the first study. In particular, similar fits are achieved using a model with two thermal components and a model with one thermal component and a nonthermal one.

However, using a larger region of radius 2 arcmin centered on Wd 1, Kavanagh et al. (2011)

obtain a spectrum between 2 and 8 keV as shown in figure 4.8. Now clearly visible is an emission line around 6.7 keV, which is attributed to a K-shell transition of helium-like iron. This confirms a dominant thermal origin of the diffuse emission at least in the inner 2 arcmin region of the cluster. Following this, the best model fit using two APEC components has a temperature of 0.69 keV at a fixed metal abundance of $2Z_\odot$ for the first component, and 3.07 keV and $0.62Z_\odot$

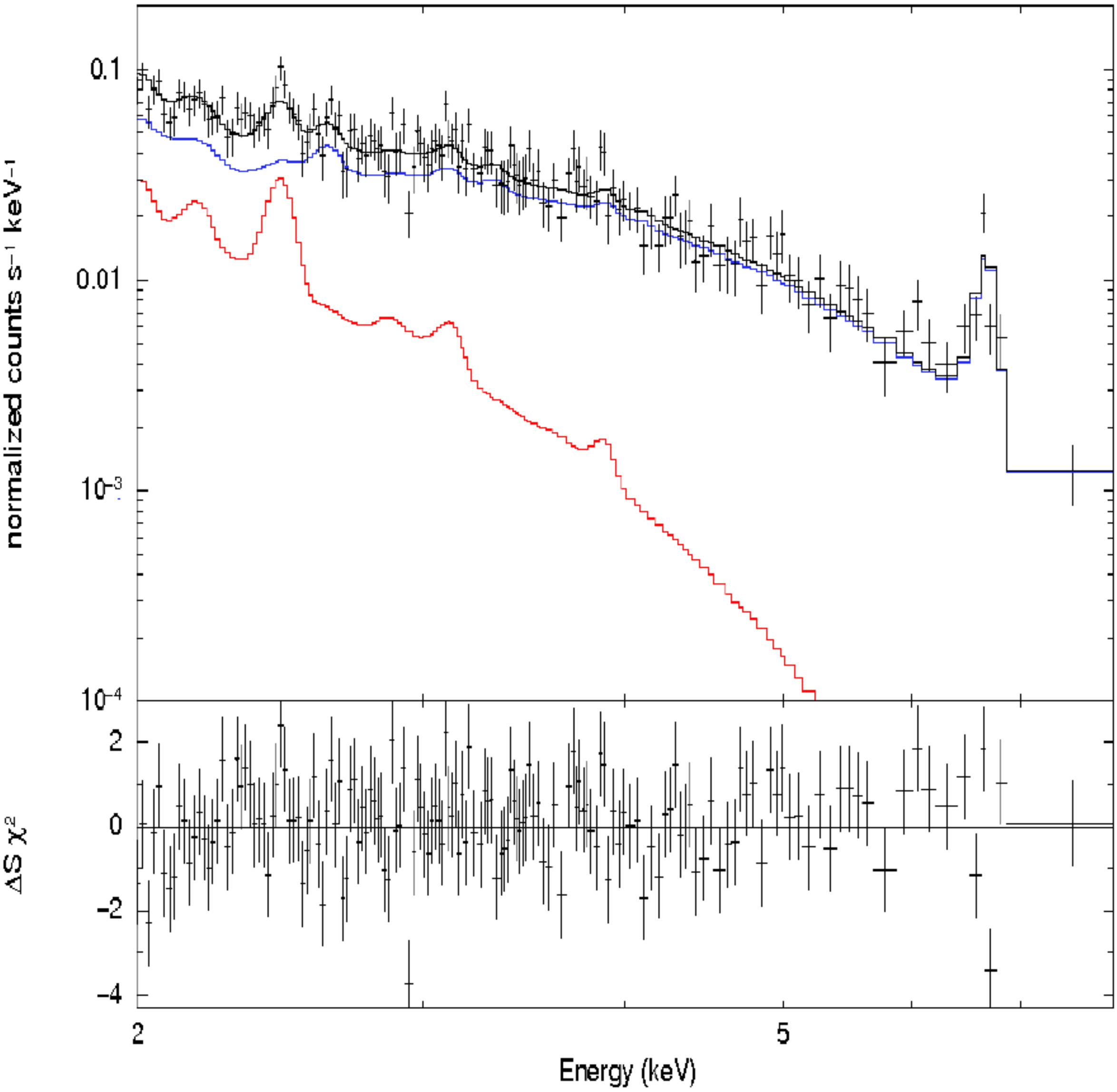

Figure 4.8: X-ray spectrum of the inner 2 arcmin region of Wd 1 as measured with the MOS cameras of the XMM Newton telescope. Clearly visible is the helium-like iron emission line around 6.7 keV. The total fitted model is given in black. It consists of a cooler thermal component, given in red, and a hotter one, in blue. Taken from Kavanagh et al. (2011).

for the second component. Outside of this central region, no significant 6.7 keV emission line is found. Still, this result provides a clear preference for the purely thermal model at least inside the cluster itself. Effectively, this rules out accelerated particles as the main source of the diffuse X-ray emission.

Discussing the origin of the thermal diffuse emission from Wd 1, Kavanagh et al. (2011) argue against SNRs as they are not observed in the cluster. Similarly, emission from unresolved pre-main sequence (PMS) stars is disfavoured as they are not expected to provide sufficient power for the observed X-ray luminosity. On the other hand, stellar winds from the cluster's stars are able to meet the energy requirement. In the analysis of Kavanagh et al. (2011), the expected X-ray luminosity from the cluster winds is in excellent agreement with the observation even considering only the central 2 arcmin. The reason is their lower adopted distance to Wd 1 of 3.55 kpc compared to the 5 kpc of Muno et al. (2006). This reduces the inferred observed X-ray luminosity to $\approx 2 \cdot 10^{33}\,\mathrm{erg\,s^{-1}}$, in agreement with the predicted cluster wind X-ray luminosity of $1.7 \cdot 10^{33}\,\mathrm{erg\,s^{-1}}$.

CHAPTER 5

Data Reduction and Images

> In der Wissenschaft gibt es keine „Tiefen“; überall ist Oberfläche: alles Erlebte bildet ein kompliziertes, nicht immer überschaubares, oft nur im einzelnen faßbares Netz. Alles ist dem Menschen zugänglich; und der Mensch ist das Maß aller Dinge.
>
> Verein Ernst Mach, Wissenschaftliche Weltauffassung

5.1 eROSITA on board SRG

For the study of diffuse X-ray emission around Wd 1, I used data from the extended Roentgen survey with an imaging telescope array (eROSITA). eROSITA is particularly well suited for this since its main purpose is the performance of all-sky surveys in the X-ray band from 0.2 to 10 keV. Consequently, the full coverage of the entire emission region of J1646−458 is guaranteed. This is in contrast to Chandra, XMM Newton, and Suzaku, which are limited by their field of view sizes.

The scientific purpose, the technical details, and the mission planning of eROSITA are explained in Predehl et al. (2021), which serves as the basis for the following discussion. eROSITA was planned and developed at the German Max Planck Institute for Extraterrestrial Physics and is mounted on the Russian Spektr-Roentgen-Gamma (SRG) satellite. Besides eROSITA, SRG also contains the Russian X-ray telescope Mikhail Pavlinsky Astronomical Roentgen Telescope – X-ray Concentrator (ART-XC) (Pavlinsky et al., 2021).

eROSITA is designed to perform eight all-sky surveys in the $0.2 - 10$ keV energy band, thus succeeding the ROSAT all-sky survey which was performed in 1990. In the hard band between

2.3 and 8 keV, eROSITA performs the first-ever imaging all-sky survey. This is complemented by the all-sky surveys of ART-XC, which is sensitive in the band between 4 and 30 keV.

The scientific goals of eROSITA are explained in detail in Merloni et al. (2012). They are as follows:

1. The main goal of the eROSITA mission lies in the detection of $\sim 10^5$ galaxy clusters, increasing the known number of these objects by at least an order of magnitude. These clusters are gravitationally bound groups of hundreds to thousands of galaxies embedded in a hot intracluster medium which emits soft X-rays. Importantly, via galaxy clusters, eROSITA will provide constraints on the growth of cosmological structures and therefore also on cosmological models. In particular, eROSITA is designed to test different models of dark energy, e.g., via providing constraints on the equation of state parameter w_{DE}.

2. eROSITA is planned to detect $\sim 10^6$ active galactic nuclei powered by supermassive black holes. Such a large sample allows statistical studies of active galactic nucleus populations, in particular of the accretion history of black holes over cosmic time.

3. eROSITA is expected to discover $\approx 10^4$ compact X-ray emitting sources, mainly X-ray binaries. This allows to determine the spatial distribution and luminosity function of these sources. Further, since eROSITA observes each position in the sky multiple times, it also provides information on the time variability of a large number of these sources.

4. The most abundant X-ray source population observed by eROSITA are stars. As previously discussed, high mass stars emit X-rays through shocks in their stellar winds, while low mass stars emit X-rays via magnetic activity. eROSITA is expected to provide a volume-complete sample of X-ray emitting stars in the Solar neighborhood, allowing unprecedented population studies.

5. Finally, due to its all-sky survey nature, eROSITA allows large-scale studies of the properties of the ISM in the Milky Way and in the nearby Magellanic Clouds. In particular, it is expected to allow insights into the nature of a large number of SNR candidates.

5.1.1 Telescope Modules and Cameras

The eROSITA telescope has a diameter of ≈ 1.9 m and a height of ≈ 3.2 m. It consists of seven telescope modules (TMs), each with an individual mirror assembly and an individual camera assembly. A schematic view of this structure can be seen in figure 5.1.

Since X-rays are only reflected under shallow reflection angles, X-ray telescopes require special mirror geometries to focus the incoming light. In the case of eROSITA, a so-called Wolter-I geometry was chosen. In a Wolter-I mirror assembly, photons are first reflected from a paraboloid shaped mirror and then from a hyperboloid mirror before they are focused onto the camera. Each of the seven mirror assemblies of eROSITA consists of 54 nested Wolter-I mirrors with a focal length of 1.6 m to increase the collecting area of the telescope. The mirrors consists of nickel with a gold coating. The angular resolution of each of the TMs is 26 arcsec when averaged over the field of view with a circular diameter of 1.03°.

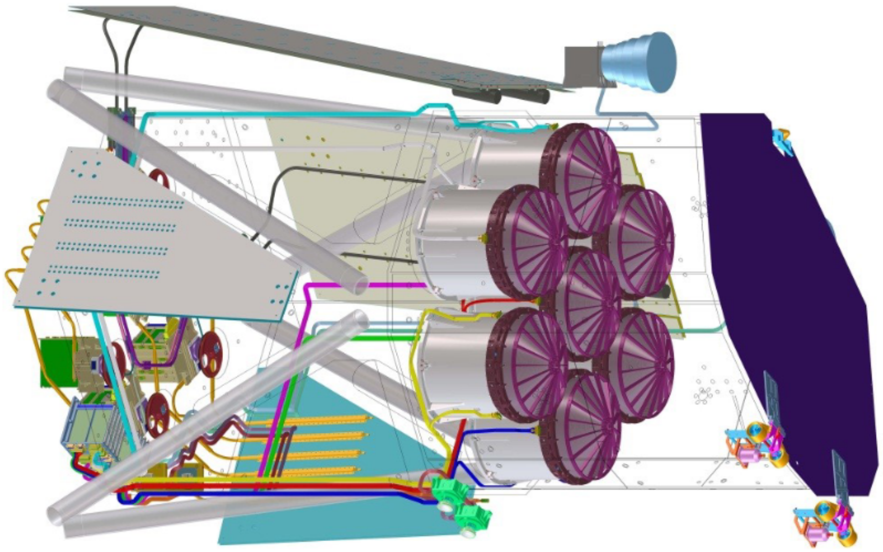

Figure 5.1: Schematic view of the eROSITA telescope. From right to left, one can see the front cover (dark blue), the seven mirror assemblies (purple), the filter wheels (red), and the camera assemblies (green). Taken from Predehl et al. (2021).

Each of the seven mirror assemblies has a charge-coupled device (CCD) at its focus. These CCDs have a rectangular shape with 384 × 384 pixels and an image area of 28.8 mm × 28.8 mm. For noise reduction, the CCDs are cooled to a temperature of ≈ -90 °C. At an energy of 1.5 keV, the resulting energy resolution of eROSITA is about 80 eV.

Further, each CCD of eROSITA is equipped with a filter wheel, visible in red in figure 5.1. These filter wheels have four different settings: 1. OPEN, used for outgassing the telescope after its launch. 2. FILTER for the standard observing mode. 3. CLOSED, which blocks incident X-rays and allows measurements of the intrinsic background of the CCDs. 4. CALIB, which places a radioactive source in front of the CCDs to allow calibration measurements.

In addition, each CCD except the ones associated with the TMs 5 and 7 possesses an on-chip filter consisting of an aluminum foil. The purpose of this filter is to prevent optical light from reaching the detector. It is absent for TMs 5 and 7 since these were planned to be used for low-energy spectroscopy. However, shortly after the launch of SRG it was noticed that these TMs suffer from optical light leak correlated with the orientation of the telescope with respect to the Sun. For this reason, TM5 and TM7 are usually excluded from data analysis. This is also the case for this thesis.

Finally, two other sources of undesired events measured by the CCDs are worth mentioning: First, the CCDs do not only register incident astrophysical X-ray photons, but also primary and secondary charged particles and their induced X-ray emission. This particle background can be measured in the CLOSED filter wheel setting. In general, it is described by individual power laws with Gaussian emission lines for the different TMs (Yeung et al., 2023). Due to the way of measurement, these models are also called filter wheel closed (FWC) models.

Second, normally, X-ray photons are reflected two times under shallow angles in the Wolter-I mirror assemblies before being measured on the CCDs. However, it is also possible for photons to reach the CCDs after single scatterings under steeper angles. In this case, the reflectivity of the mirrors differs from the nominal value, softening the spectrum of a source observed in such a way. This stray light is typically prominent for bright point sources and can hit the detector at pointing angles up to about 3° from a source. A stray light halo resulting from this single reflection effect is also prominent around the LMXB GX 340+0, significantly contaminating the eROSITA observation of Wd 1.

5.1.2 eROSITA All-sky Surveys

SRG was launched on July 13, 2019 from the Baikonur cosmodrome in Kazakhstan using a Proton-M rocket. In October 2019 it reached the second Lagrange point L2 of the Sun-Earth system where the mission's orbit lies. Lagrange points are equilibrium points in the combined gravitational potential of two masses orbiting each other. For any such system, there are five Lagrange points. In the case of the Sun and the Earth, L1 lies at a distance of $1.5 \cdot 10^6$ km from the Earth in the direction of the Sun, while L2 lies at the same distance in the opposite direction. L3 lies opposite of Earth as seen from the Sun, while L4 lies 60° ahead of Earth on its orbit and L5 lies 60° behind Earth on its orbit. In particular, L2 is a handy place for the placement of satellite missions since it allows to keep a fixed position relative to Earth with minimal course corrections.

eROSITA is planned to complete eight all-sky surveys, called eROSITA all-sky survey (eRASS), over the course of its lifetime. The survey strategy is as follows: In addition to its orbit around L2, SRG also rotates around its own axis with a rotation period of about 4 h. Consequently, eROSITA observes a complete great circle across the sky with the width of its field of view in this 4 h time frame, which is also called an "eRODay".

In addition to this first rotation around its own axis, a second rotation around an axis perpendicular to the first one is superimposed. Consequently, over the course of an eROday, the pointing of SRG drifts perpendicularly to the extent of the observed great circle at a rate of 10 arcmin per 4 h. Therefore, eROSITA performs a complete all-sky survey within a time frame of about half a year. The rotation axis of this drift is orientated in such a manner that the ecliptic poles of the Solar system are observed every eROday. As a result, the final exposure time of eROSITA varies over the sky and is two orders of magnitude larger at the ecliptic poles as compared to the ecliptic plane. For example, after the first all-sky survey, the exposure time at the poles was $\approx 10\,000$ s while it was only ~ 100 s in the ecliptic plane.

eROSITA started its first all-sky survey eRASS1 on December 13, 2019. At the time of writing of this thesis, it has completed four eRASSs in total and begun the fifth one. For data analysis purposes, it is common to combine data from the different survey. In that regards, the nomenclature "eRASS:n" stands for the combined data of all all-sky surveys up to eRASSn. Further, for an easier handling of the data, the sky as seen by eROSITA is split into different overlapping sky tiles of size 3.6° × 3.6°.

Finally, it is noteworthy that the data ownership of eROSITA is split equally between the Russian and the German half of the SRG mission. On the Russian side, Roscosmos holds the rights to the data of the eastern half of the sky in Galactic coordinates. On the German side, the Max Planck Institute for Extraterrestrial Physics has ownership of the data of the western half of the sky. The demarcation line is the great circle of constant galactic longitude passing through the position of the central supermassive black hole Sagittarius A*, roughly at a Galactic longitude of $l \approx 0$. The German eROSITA consortium plans to eventually publish all its data in a series of subsequent data releases. In June 2021, the first of these releases contained the data of the calibration and performance verification phase prior to eRASS1.

5.2 Data Reduction

For obtaining the necessary eROSITA data for the analysis of Wd 1 and its surroundings, I used the web page DATool which is available to eROSITA members. It allows to request data in several possible processing stages for different sky tiles. For this project, I obtained data from eRASS1 to eRASS4 for the four adjacent sky tiles 249138, 250135, 254135, and 254138. Wd 1 lies roughly at the point where these sky tiles meet each other. For orientation on the sky, the eRASS1 all-sky map in Galactic coordinates is presented in figure 5.2. In this figure, the rough position of Wd 1 is indicated with a red circle.

For my analysis, I downloaded the necessary data in the form of event files. These are tables containing information on measured photon events and their energies for different times and coordinates on the detector. The data was processed using the newer 020 eROSITA pipeline, formerly called 948. Among other things, this pipeline removes hot pixels from the event files, performs an energy calibration for determining the energies of the events, and performs attitude calculations necessary for determining where the telescope looked at a specific time.

I performed the data reduction, image creation, and spectrum extraction via the eROSITA Science Analysis Software System (eSASS). eSASS provides tasks for the reduction of eROSITA data, the creation of calibrated data products, and for data analysis. As a first step of the data reduction, I performed the task `evtool` to merge the separate event files of the four different sky tiles and of eRASS1 to eRASS4 into a single event file.

After merging the event files, I recentered the resulting combined file to the position of Wd 1, i.e., $(\alpha, \delta) = (16^{\mathrm{h}}47^{\mathrm{m}}02.4^{\mathrm{s}}, -45°51'07")$, using the `radec2xy` task. Next, again using the task `evtool`, I filtered the event file using the flag 0xc00f7f30 which, among other things, discards pixels next to bad pixels, bright pixels, as well as pixels lying on bad columns. As a final step, I also performed good time interval (GTI) filtering using the FLAREGTI flag. This serves two main purposes: 1. It discards rows in the event file which do not lie in a so-called GTI, i.e., a time when the telescope did not meet some specified quality parameters. 2. Since I did not choose the GTI flag, but FLAREGTI, it also filtered out time intervals containing potential flare-like events based on the lightcurve of the event file. An investigation of the spectra described in the next section shows that the additional flare filtering reduced their exposure times by $\approx 2\%$ to $\approx 7\%$. In addition, I also performed the search for synchrotron radiation without flare filtering and confirm that this process doesn't change the analysis results described in the next chapter.

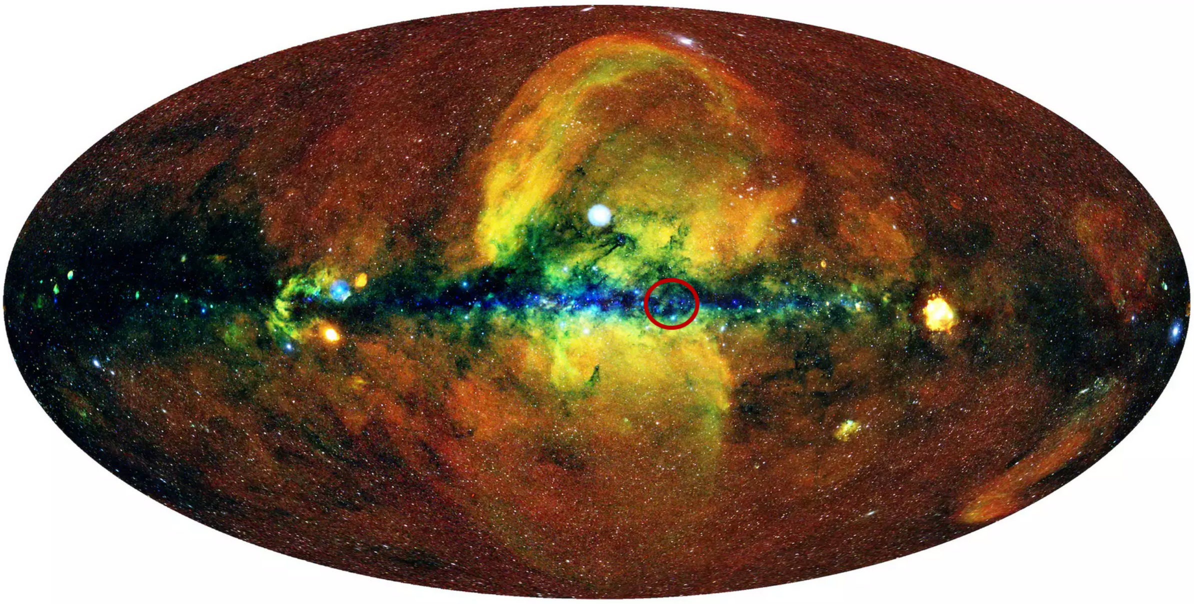

Figure 5.2: X-ray all-sky map as obtained with eRASS1 in Galactic coordinates and an Aitoff projection. Red color indicates $0.3-0.6\,\mathrm{eV}$, green $0.6-1.0\,\mathrm{keV}$, and blue $1.0-2.3\,\mathrm{eV}$. Wd 1 is roughly located at the center of the red circle. Credit: MPE/IKI.

5.3 Images of Westerlund 1

After preparing the combined event file, I used it for creating images of the surroundings of Wd 1 for a visual inspection. Again, this was done using the eSASS command `evtool`, this time using the flag `image=yes`. This command requires to set two main parameters determining the properties of the resulting image: `rebin` and `size`.

The `rebin` parameter sets the angular size of the pixels in the produced image. Specifically, it is an integer number which determines the number of virtual pixels in the event file which are to be combined into a single image pixel. I chose `rebin=100`, corresponding to an image pixel size of 5 arcsec. Note that this is about a factor 5 smaller than the average angular resolution of eROSITA of 26 arcsec.

Next, the `size` parameter sets the size of the produced image. It takes an integer number as its argument which determines the extent of the image in one direction in units of image pixels. Specifically, I chose `size=7000`, which corresponds to an image side length of $7000\cdot 5\,\mathrm{arcsec} \approx 9^\circ$. As a result, the final image has an extent of roughly $9^\circ \times 9^\circ$. Note that this is bigger than the angular extent of the four sky tiles combined into a single square, which is roughly $8^\circ \times 8^\circ$. Consequently, the final image contains the complete data of all four sky tiles used.

As a final note, I did not perform exposure correction in the creation of the images, i.e., I did not normalize each pixel to the same exposure time. The reason for this is that the exposure of the produced image is already quite uniform, as revealed by an inspection of the corresponding exposure map. In general, fluctuations in the exposure time between different pixels are at a level below 3%. The main exception to this is vignetting, an effect caused by the effective area of

X-ray telescoped being smaller for sources further removed from its line of sight. In the images, this effect is visible as a drop in exposure at the image edges. However, since the region of interest for this study lies at the center of the image, I deem vignetting effects to be negligible.

The inner part of the final image surrounding Wd 1 is given in 5.3. For this image, all energy bands were combined, thus giving the total flux in the 0.2 – 10 keV band. The position of Wd 1 is marked with a dashed white circle with a radius of 3 arcmin, corresponding to its optical radius. In the south-east of the star cluster, the magnetar CXOU J164710.2−455216 is visible as a point source. The image size was chosen in such a way as to encompass the emission region of J1646−458 (compare to figure 4.3). Clearly visible to the north-west of Wd 1 and marked with a dashed orange circle is the LMXB GX 340+0. Actually a point source, this objects looks strongly extended in the image due to its pronounced stray light halo.

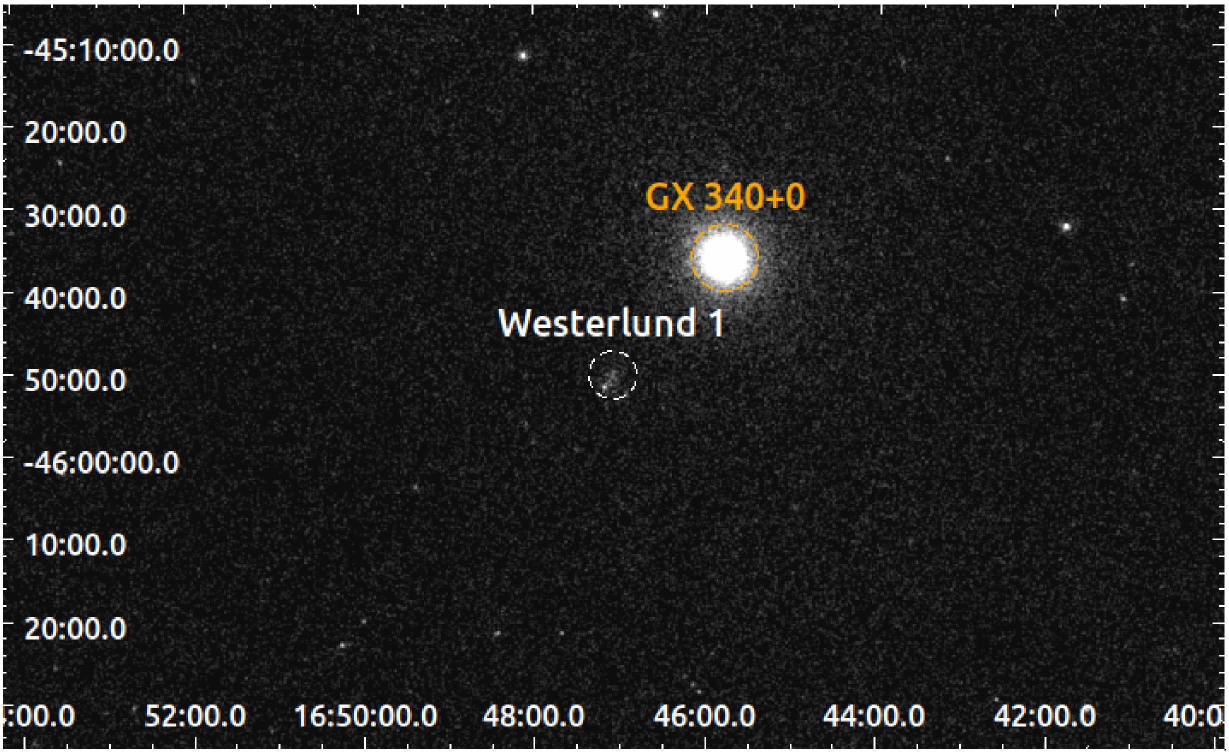

Figure 5.3: eROSITA image of Wd 1 and its immediate surroundings in the band from 0.2 keV to 10 keV. The x-axis gives the right ascension in hour angles while the y-axis gives the declination in degrees. The image was smoothed using a Gaussian kernel with a standard deviation of 1.5 arcsec.

In addition, a false-color RGB image of the same region is shown in figure 5.4. The red color corresponds to the band between 0.7 and 1.1 keV, green to 1.1 to 2.3 keV, and blue to 2.3 to 10 keV. Softer energies were omitted because they revealed the least details about the region. As can be seen from its green color, Wd 1 emits mostly in the band between 1.1 and 2.3 keV. The same is the case for the magnetar CXOU J164710.2−455216 to its south-east. On the other hand, the LMXB GX 340+0 is a particularly hard source which strongly emits beyond 2.3 keV.

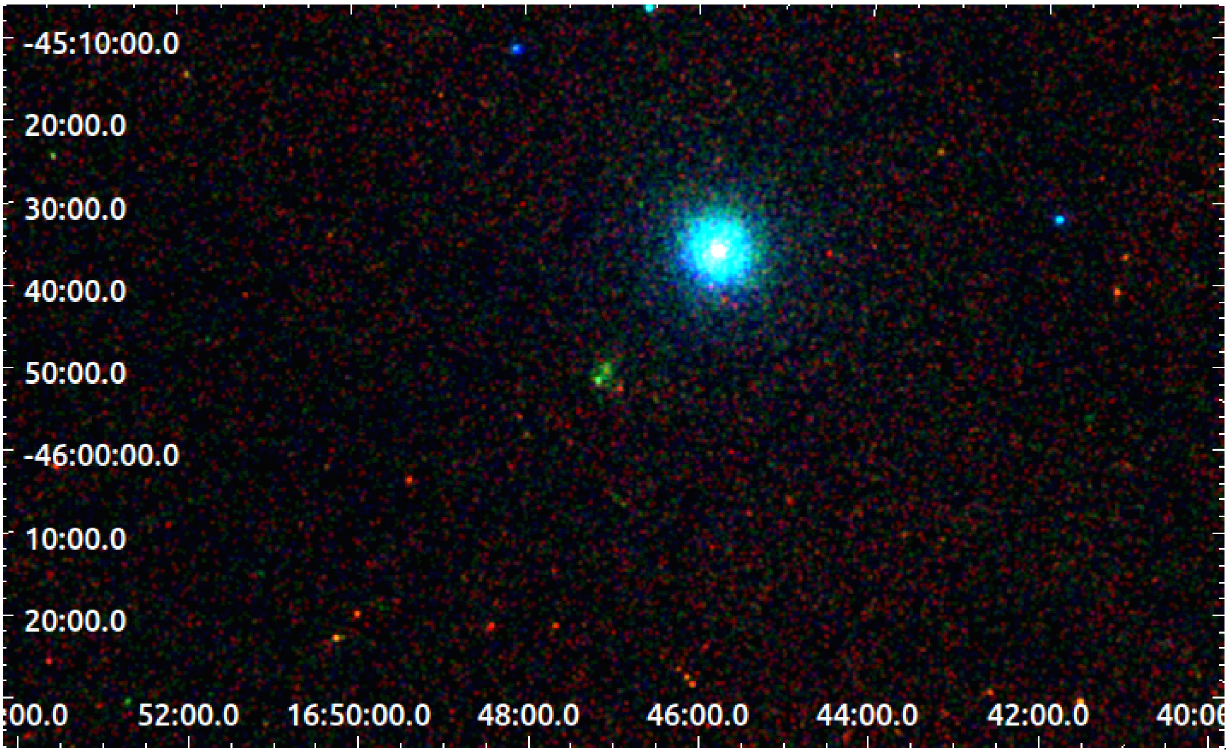

Figure 5.4: False-color RGB eROSITA image of Wd 1 and its immediate surroundings. The red color corresponds to $0.7-1.1$ keV, green to $1.1-2.3$ keV, and blue to $2.3-10$ keV. As before, the x-axis gives the right ascension in hour angles while the y-axis gives the declination in degrees. The image was smoothed using a Gaussian kernel with a standard deviation of 2.5 arcsec.

Finally, since my spectral analysis focuses on the diffuse emission of Wd 1 and its surroundings, I masked point sources from the combined event file to reduce their contaminating effect in the obtained spectra. For doing this, I used the script `select_regions.py` provided by Jonathan Knies[1]. This script writes a region file containing all point sources in the image which are listed in an eRASS4 source catalog. I found a radius of 50 arcsec around the point sources to be the lowest value still removing most of their emission.

In addition, I manually removed bright point sources with extents beyond 50 arcsec as well as a few extended sources by using circular masks. Most of these bright point sources are X-ray binaries with pronounced stray light halos. Note that I also proceeded like this for GX 340+0, for which I used a mask of radius 1.08 arcmin. This still leaves a significant amount of stray light from this source in the event file, but choosing a larger mask would remove too much of the region of interest corresponding to J1646−458. A list with the coordinates and radii of all manually selected masks is given in table A1.1 in the appendix.

---

[1] Private communication

CHAPTER 6

Analysis of the Diffuse Emission around Westerlund 1

> [L]ook at the story of Man, and come to your senses! It is not the destination, but the trip that matters. What you do *today* influences tomorrow, not the other way around. Love Today, and seize All Tomorrows!
>
> Nemo Ramjet, All Tomorrows

6.1 Stray Light from GX 340+0

This chapter focuses on the search for nonthermal radiation in the region around Wd 1 coinciding with J1646−458. In this analysis, the biggest challenge was the proximity to the LMXB GX 340+0 to Wd 1, which causes a strong stray light contamination of the source region. This is especially tricky to deal with since, to my knowledge, no models for stray light spectra in eROSITA are available so far.

To get a better idea of the nature of this contamination, I extracted spectra of the point source GX 340+0 and of its stray light halo. In that regard, it is important to note that the scientific aim of this thesis only relates to diffuse emission, i.e., it is not aimed at using the spectra of GX 340+0 or its halo to draw conclusions about its physical or astronomical nature. Therefore, the fits I performed to the LMXB and its halo are phenomenological in nature and were not checked for the reasonability of the resulting fit parameters. Rather, their only purpose is to help with the proper consideration of the stray light contamination around Wd 1.

Keeping this in mind, a point source spectrum of GX 340+0 as produced from eRASS:4 data can be seen in figure 6.1. This spectrum was extracted using the eSASS command `scrtool`, developed for extracting spectra of point sources and extended regions. In this case, I chose the source extent type ”`POINT`” and did not specify a point spread function. The source position is $(\alpha, \delta) = (251.449°, -45.611°)$. Further, I did not subtract a background since GX 340+0 is bright enough to dominate over its background.

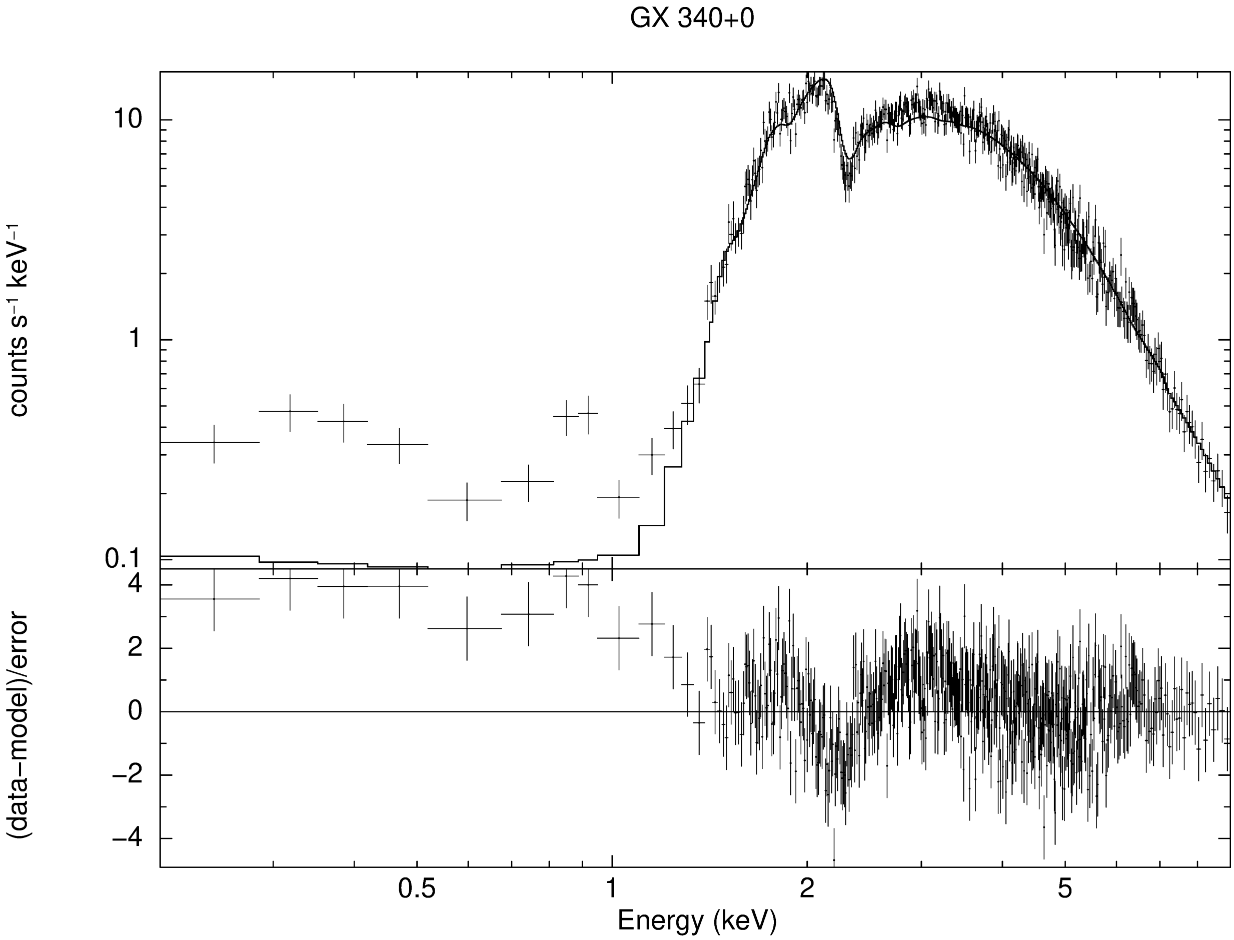

Figure 6.1: *Upper panel:* Point source spectrum of the LMXB GX 340+0. The data is binned to a minimum detection significance of 5σ. Pay attention to the fact that the shown spectrum is still convolved with the instrument's response. The black line is an `Xspec` model consisting of a `diskbb` and a `compTT` component. *Lower panel:* Residua of the fit divided by the uncertainty of each data bin.

As specified, `srctool` extracted the spectrum of the point source and produced the corresponding ancillary response files (ARFs) and redistribution matrix functions (RMFs) for each of the eight TMs. These two files are necessary for relating quantities measured by X-ray telescopes, i.e., count numbers in energy bins, to the physical properties of a source. In particular, the ARF relates the number of count to a source flux, using information on the effective area of the telescope mirrors, the detector's quantum efficiency, the aspect history of the telescope, as well as on the point spread function. On the other hand, the RMF relates the energy bins of the detector to the energy of measured photons by providing a probability for a photon with a specific energy E to be measured in an energy bin E_i (Davis, 2001).

The spectrum given in figure 6.1 then results from combining the spectrum obtained by `srctool` with the RMF. For this, I used all TMs except TM5 and TM7, which suffer from light leak. Note that the spectrum is still convolved with the ARF, as is the case for all other eROSITA X-ray spectra shown in this thesis. Importantly, this also explains the spectrum's prominent absorption edge slightly above 2 keV, which stems from absorption in the telescope mirrors' gold coating.

Inspired by earlier studies of GX 340+0 (Lavagetto et al., 2004; Miller et al., 2016), I fitted its spectrum with a phenomenological model to obtain a rough spectral shape for the latter analyses of contaminated regions. As for all X-ray analyses in this thesis, I used the spectral fitting software `Xspec`[1], version 12.13.1. In this case, the model consists of a thermally emitting accretion disk component `diskbb` plus IC upscattered photons in a hot plasma described by a `compTT` component (Titarchuk, 1994). Both components are absorbed by a shared Tübingen-Boulder ISM absorption component `tbabs`. This model considers absorption from atomic matter, molecular hydrogen, and dust. It requires to set Solar metal abundances for reference for which the values provided by Wilms et al. (2000) were chosen. This is the case for the entire thesis. Finally, the photoionization cross sections used by `Xspec` were always set to the values given by Verner et al. (1996).

The fit parameters are given in table 6.1 whereas the resulting fit can be seen in figure 6.1. The parameters are the column density N_H of absorbing material for `tbabs`, the temperature at the inner edge of the accretion disk T_in and a normalization η_diskbb for `diskbb`, as well as the target photon temperature $k_\mathrm{B}T_\gamma$, the plasma temperature $k_\mathrm{B}T_\mathrm{plasma}$, the optical depth t, and a normalization η_comp for `compTT`.

Overall, the fit provides a good description of the shape of the spectrum. Still, there are strong residua around 2 keV and around 3 keV. As these positions coincide with the gold-coating absorption edge of the ARF and the flux maximum of the spectrum, respectively, they might be caused by inaccuracies in the energy calibration. Further, the plateau-like feature below 1 keV is not described by the model at all. As it is likely no background radiation, it might stem from calibration issues with the RMF.

Further, I also extracted two spectra of GX 340+0's stray light halo. This is especially informative since the process of single scatterings in the Wolter-I mirror has a different reflectivity than the nominal double scatterings. In particular, the reflectivity decreases especially for higher energies, leading to a softening of the stray light spectrum compared to the source spectrum.

For the first spectrum, an annulus centered on GX 340+0 with an inner radius of 4.156 arcmin and an outer radius of 8.311 arcmin was chosen. For the second spectrum, an inner radius of 8.311 arcmin and an outer radius of 16.623 arcmin was used. Note that the latter outer radius corresponds to the distance from GX 340+0 to the edge of a circle with radius 3 arcmin around Wd 1. As before, I used `srctool` for extracting the spectra, this time with the source extent type TOPHAT. Different from the other spectra discussed in the following, I did not use the event file with masked point sources for spectrum extraction, as the stray light halo is masked in it.

---

[1] https://heasarc.gsfc.nasa.gov/xanadu/xspec/

Table 6.1: Fit parameters for the `diskbb + compTT`-model used to describe the spectrum of GX340+0. For `compTT`, the standard analytic method for the determination of the optical depth was used.

Component	Parameter	Unit	Value	Confidence Interval (90%)
`tbabs`	N_H	$10^{22}\,\mathrm{cm}^{-2}$	$5.63^{+0.13}_{-0.13}$	$(5.50, 5.76)$
`diskbb`	$k_\mathrm{B}T_\mathrm{in}$	keV	$1.23^{+0.10}_{-0.10}$	$(1.13, 1.33)$
	η_diskbb	$10^{-2}\,\mathrm{km}^2\,\mathrm{kpc}^{-2}$	$57.5^{+0.9}_{-0.9}$	$(56.6, 58.4)$
`compTT`	$k_\mathrm{B}T_\gamma$	keV	$9.273^{+29.204}_{-9.079}\cdot 10^{-3}$	$(1.94\cdot 10^{-4}, 3.8477\cdot 10^{-2})$
	$k_\mathrm{B}T_\mathrm{plasma}$	keV	135^{+21}_{-17}	$(118, 156)$
	τ		$4.71^{+0.16}_{-0.17}$	$(4.54, 4.87)$
	η_comp	kpc^{-2}	$3.28^{+0.14}_{-0.15}\cdot 10^{-2}$	$(3.13\cdot 10^{-2}, 3.42\cdot 10^{-2})$

The resulting spectra of the stray light halo of the LMXB are given in figure 6.2.

First looking at panel a, the spectrum shown there seems softer in comparison to the one in figure 6.1. This is particularly clear when comparing the peak flux below the 2 keV absorption edge with the peak flux above it. This effect is even more pronounced for panel b, where stray light further removed from GX 340+0 was extracted. This might be due to the relative increase of X-ray background flux as compared to the stray light flux, but also due to the spectral softening expected from the change in reflectivity for single scattering stray light. Overall, the `diskbb + compTT` above cannot necessarily be expected to provide a good fit to the stray light

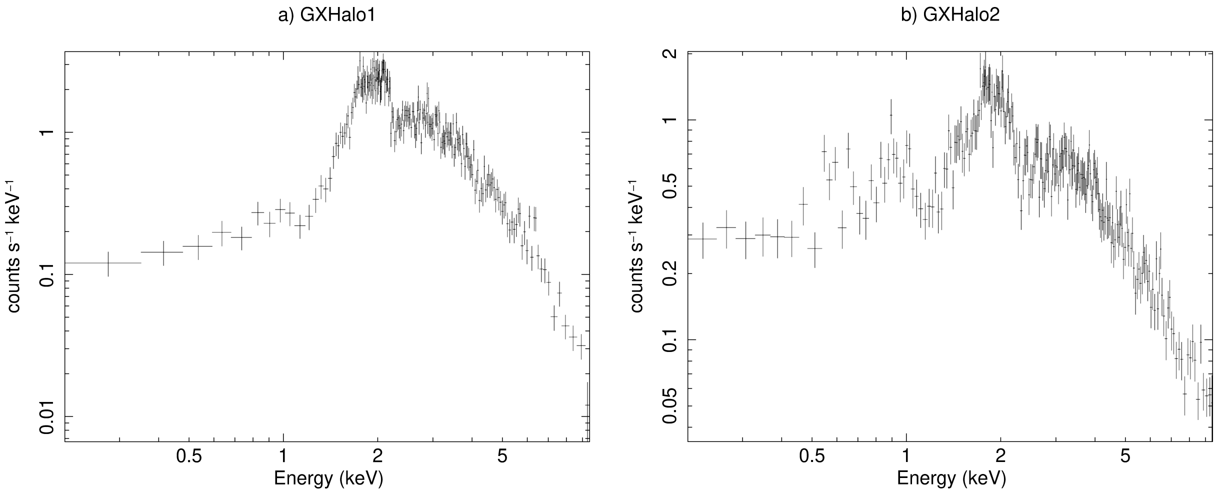

Figure 6.2: *Panel a:* Spectrum of an annulus around GX 340+0 with an inner radius of 4.156 arcmin and an outer radius of 8.311 arcmin. The data is binned to a minimum detection significance of 5σ. *Panel b:* Like panel a, but the inner radius is 8.311 arcmin and the outer radius is 16.623 arcmin. Pay attention to the fact that both spectra are still convolved with the instrument's response.

around GX 340+0. Instead, I will use this model as a starting point for the individual fits to the stray light contamination in the following analysis.

6.2 Search for Synchrotron Radiation

The main part of this study is the search for signs of nonthermal radiation in the vicinity of Wd 1. The flux maximum of the shell-like structure J1646−458 found by Aharonian et al. (2022) lies at a distance of $\approx 0.5^\circ$ from the position of Wd 1. Therefore, I decided to analyze the surroundings of Wd 1 up to a radius of 40 arcmin.

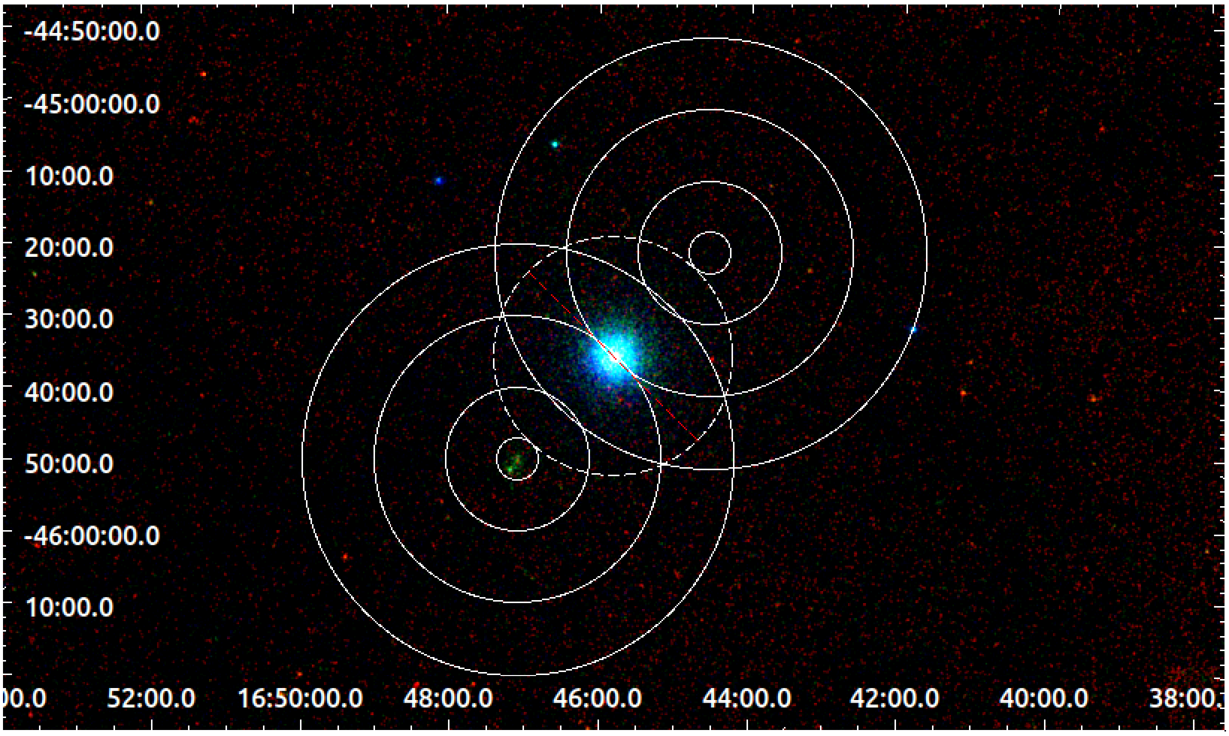

Figure 6.3: The spectral analysis regions Wd10, Wd20, and Wd30 can be seen in white around the star cluster Wd 1 (in green). The masked region around GX 340+0 is marked by a red line. To the north-west of GX 340+0, the mirrored test regions WdT10, WdT20, and WdT30 can be seen. The image was smoothed using a Gaussian kernel with a standard deviation of 2.5 arcsec. Note that for the actual spectrum extraction, the masked event file was used.

More specifically, I defined four analysis regions in the shape of annuli centered on Wd 1, i.e., a position of $(\alpha, \delta) = (251.767^\circ, -45.851^\circ)$. These annuli were labeled Wd10, Wd20, Wd30, and Wd40, corresponding to radii of $3-10$ arcmin, $10-20$ arcmin, $20-30$ arcmin, and $30-40$ arcmin, respectively. In other words, the label "Wdn" marks an outer radius of the respective annulus of n arcmin.

As the resulting regions encompass areas very close to GX 340+0, the surroundings of the LMXB were masked for each region. For Wd10, Wd20, and Wd30, the masked region is centered on $(\alpha, \delta) = (251.449°, -45.611°)$ and has a radius of 16.623 arcmin, reaching to the edge of the 3 arcmin radius circle around Wd 1. The resulting regions and the masks can be seen around Wd 1 in figure 6.3, whereas the additional test regions visible in the figure will be discussed in the following. Only in the case of Wd40, a larger radius of the mask of 30 arcmin was chosen, as can be seen in figure 6.4. This is justified by the larger area of Wd40, ensuring better statistics even for such a large mask.

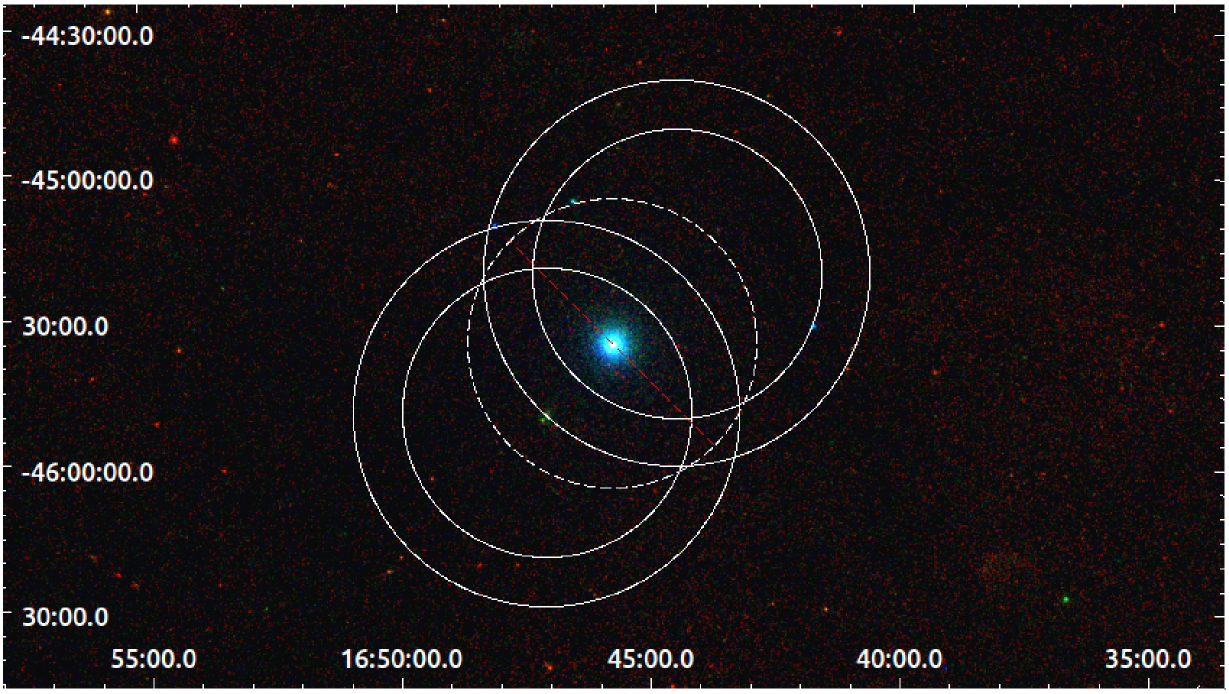

Figure 6.4: The spectral analysis region Wd40 can be seen in white around the star cluster Wd 1 (in green). The masked region around GX 340+0 is marked by a red line. To the north-west of GX 340+0, the mirrored test region WdT40 can be seen. The image was smoothed using a Gaussian kernel with a standard deviation of 2.5 arcsec. Note that for the actual spectrum extraction, the masked event file was used.

Even though the masks were defined to remove as much contamination from stray light as possible while keeping the statistics of the analysis regions high, this does not guarantee a negligible amount of contamination in Wd10 to Wd40. As explained in Freyberg et al. (2020), the stray light contamination from bright sources can extend out to $\approx 3°$ away from them, i.e., well beyond the furthest point of Wd40 from GX 340+0. Further, to my knowledge, no method for spectrally modelling stray light contamination in eROSITA is available in the literature, making a spectral search for a nonthermal synchrotron component in the analysis regions difficult. Indeed, initial attempts to do so suffered from the difficulty to distinguish the particle background, the X-ray background, the stray light contamination, and a potential nonthermal source component. For this reason, I decided to compare Wd10, Wd20, Wd30, and Wd40 to suitable test regions as a first step.

There are three requirements for such test regions: 1. They should be close enough to the analysis regions to have a comparable X-ray background. 2. They should contain a comparable amount of stray light contamination. 3. They should be far enough removed to not contain a significant amount of a possible nonthermal source component.

In particular, requirement 2 lead me to define these test regions, labeled WdT10, WdT20, WdT30, and WdT40, as shown in figures 6.3 and 6.4. In essence, the analysis regions Wd10, Wd20, Wd30, and Wd40 were mirrored on the position of the LMXB GX 340+0. This ensures that their distance to the source of stray light contamination is identical to the respective distance of the analysis regions, making a similar contamination likely under the assumption of a spherical stray light halo.

Regarding requirement 1, these test regions are relatively close to the analysis regions with a distance of less than 1°. Finally, regarding requirement 3, a comparison to the extent of J1646−458 in figure 4.3 shows that the test regions should contain significantly less VHE emission than the analysis regions. In a leptonic scenario, this also applies to synchrotron radiation which should stem from the same electron population as the γ-rays. Similarly, in a hybrid hadronic-leptonic scenario, the X-ray synchrotron should come from a less extended region than the γ-rays since electrons have smaller cooling times than hadrons and are not transported as far as them.

6.2.1 Visual Comparison to Test Regions

Using the masked event file, spectra of all eight analysis and test regions were extracted via `srctool` with the usual settings for an extended source. The resulting spectra of all TMs except number 5 and 7 combined can be seen in figure 6.5. The four panels correspond to the four sets of an analysis region in black and the corresponding test regions in red. All eight spectra are binned to a minimum detection significance of 2σ per bin. Judging by eye sight, no particularly strong difference between analysis and test regions is visible.

For a better comparison, figure 6.6 gives the difference of the analysis regions minus the test region for each of the four pairs. The upper part of each panels gives the absolute difference, while for the lower panels the difference is normalized wit the uncertainty of the data. Again judging by eye, the resulting residua seem to be consistent with zero. If anything, Wd20 − WdT20 (panel b) and Wd40 − WdT40 (panel d) seem to tend to negative values, indicating higher fluxes in the test regions than in the analysis regions.

6.2.2 Gaussian Fits and t-tests

For a more rigorous analysis of the differences between the analysis and test regions, I first fitted the histograms of the residua in figure 6.6 with Gaussian distributions and then performed statistical t-tests to test the hypothesis of more photon counts in the analysis than in the test region. For plotting the residua histograms, I first subtracted the count value in each energy bin of a test spectrum from the count value in the corresponding bin of the analysis spectrum.

Note that this analysis was performed on the level of count numbers, not photon fluxes as for figures 6.5 and 6.6. The fluxes are derived by dividing the photon counts by the exposure times

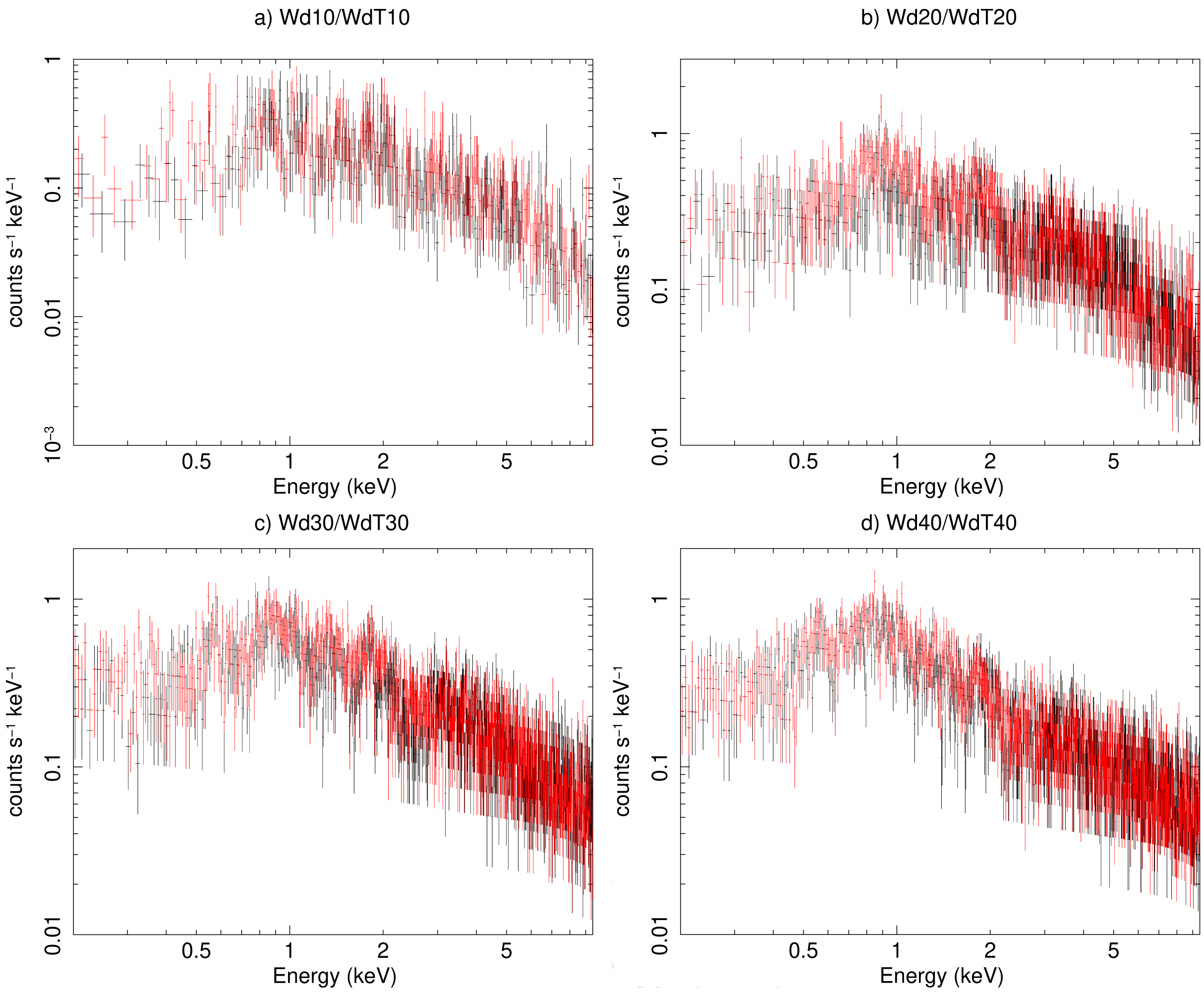

Figure 6.5: Black data shows the X-ray spectrum of an analysis region and red data shows the X-ray spectrum of the corresponding test region. All spectra are binned to a minimum significance of 2σ. The different spectra are Wd10 and WdT10 (*panel a*), Wd20 and WdT20 (*panel b*), Wd30 and WdT30 (*panel c*), and Wd40 and WdT40 (*panel d*).

of the spectra. Consequently, the analysis of the residua histograms assumes identical exposure times for each pair of an analysis and a test region. The exposure times as given in the headers of the spectral fits files are given in table 6.2. As one can see, for each of the four pairs the exposure time of the test region is higher than the exposure time of the analysis region. Nevertheless, the absolute differences are small and of the order of 10 s. The last row of the table gives the relative differences, calculated as (Exposure Test − Exposure Analysis)/Exposure Analysis. The largest relative difference, the one for Wd10 and WdT10, is about 1%. For the three other pairs, the relative differences are even smaller. Therefore, I conclude that the effect of the difference in exposure times on the following analysis is negligible.

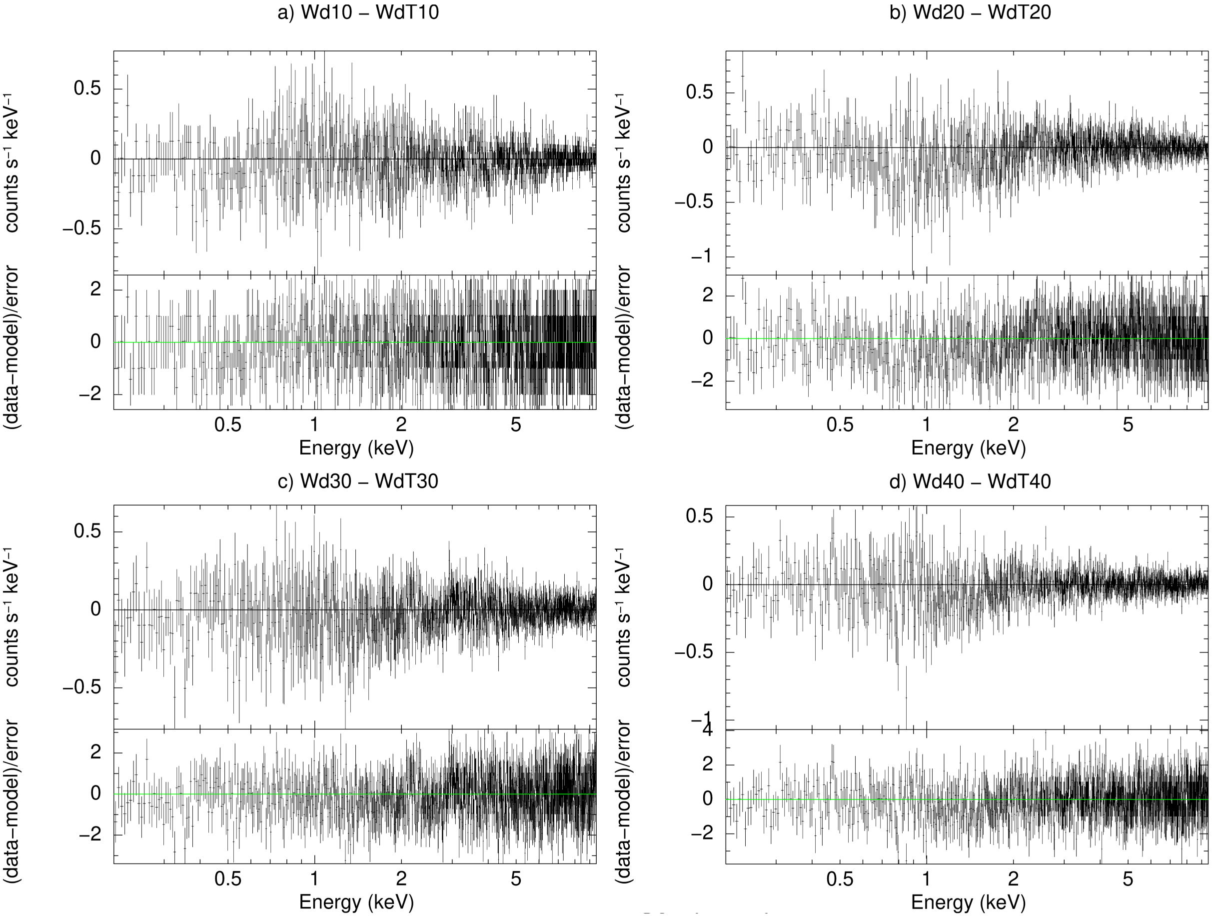

Figure 6.6: Each panel shows the spectrum of an analysis region minus the spectrum of the corresponding test region in its upper part and the same difference normalized by the uncertainty of the data in the lower part. The different spectra are Wd10 and WdT10 (*panel a*), Wd20 and WdT20 (*panel b*), Wd30 and WdT30 (*panel c*), and Wd40 and WdT40 (*panel d*).

Table 6.2: Comparison of the exposure times of the analysis and test regions. The last row is the exposure time of a test region minus the exposure of the corresponding analysis region, divided by the exposure of the analysis region.

Exposure times [s]	Wd10/WdT10	Wd20/WdT20	Wd30/WdT30	Wd40/WdT40
Analysis region	1498.010	2332.244	3467.828	4494.751
Test region	1513.712	2348.294	3484.578	4507.162
Relative difference	0.0104	0.00683	0.00481	0.00275

The resulting histograms of the residua can be seen in figure 6.7 in red. In these plots, the x-axis gives the count difference between an energy bin of the analysis region and the corresponding test region bin, and the y-axis gives the number of differences with the value given by the x-axis. The rough shape of these histograms seems similar to Gaussian distributions with a maximum value close to a count difference of zero and a symmetric decline on both sides. Note that a skewness of the distributions to the right would indicate more counts in an analysis region, and a skewness to the left would indicate more counts in the test region.

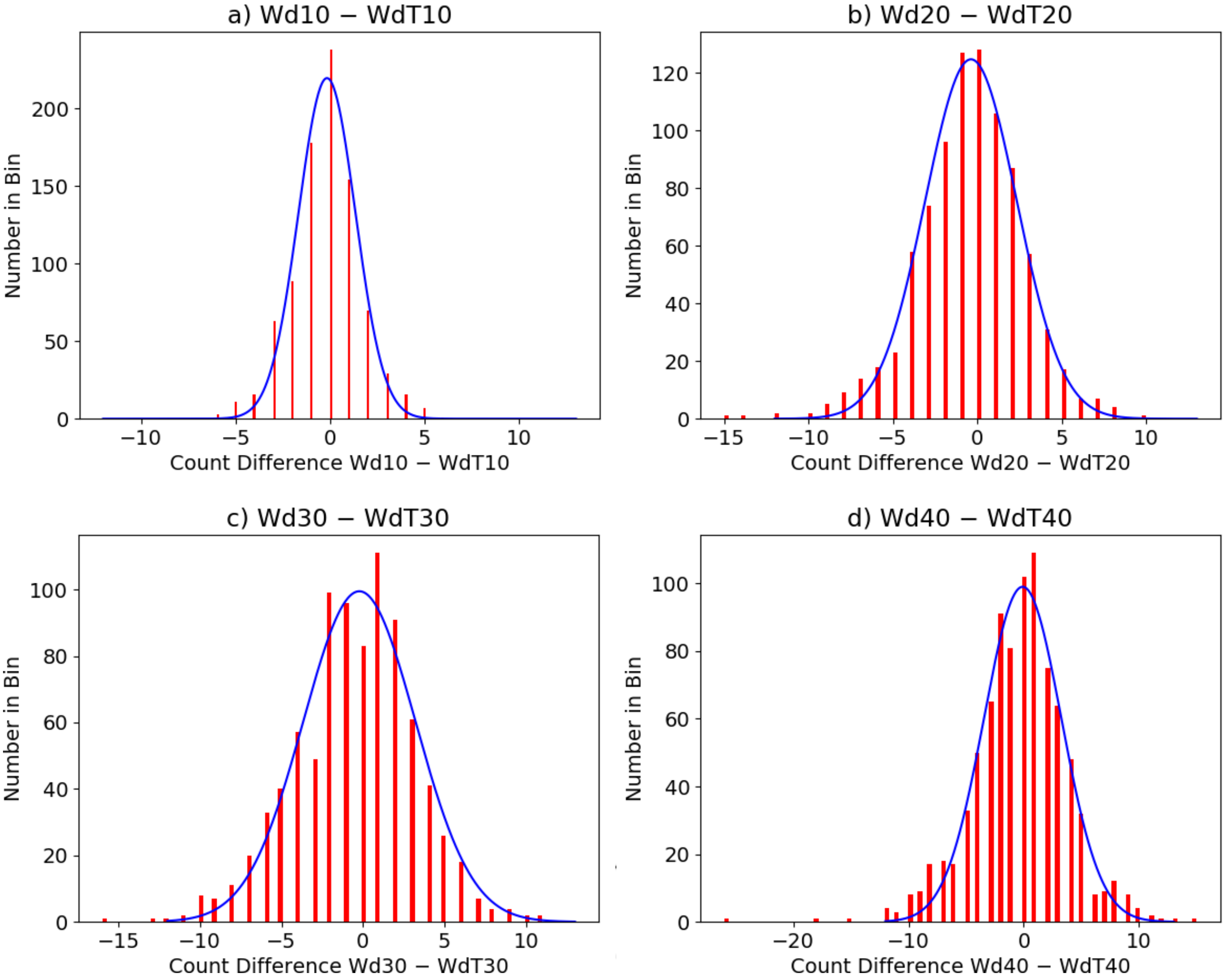

Figure 6.7: The red data shows the histograms of the residua of the subtraction of test region spectra from the corresponding analysis region spectra. The blue lines are Gaussian fits and are explained in the text. The different panels are: *a* – Wd10/WdT10, *b* – Wd20/WdT20, *c* – Wd30/WdT30, *d* – Wd40/WdT40.

To better understand the nature of these histograms, I performed fits to them. The histograms were obtained by subtracting two X-ray spectra, which generally have a scatter described by Poisson distributions. The distribution of the difference of two Poisson-distributed variables is given by the so-called Skellam distribution or Poisson difference distribution (Skellam, 1946). It is a discrete distribution with the probability mass function

$$P(k;\mu_1,\mu_2) = \mathrm{e}^{\mu_1+\mu_2}\left(\frac{\mu_1}{\mu_2}\right)^{k/2} I_{|k|}(2\sqrt{\mu_1\mu_2}), \tag{6.2.1}$$

where μ_1 and μ_2 are the expected means of the two Poisson variables and $I_k(z)$ is the modified Bessel function of the first kind.

The underlying Poisson distributions can be approximated with Gaussian distributions for $\mu_1, \mu_2 \gtrsim 100$, which is the case here. Further, since the difference between two Gaussian distributions is again a Gaussian distribution, the Skellam distribution can be approximated with a Gaussian distribution. Specifically, I fitted the residua histograms with

$$P(k;A,\mu,\sigma) = \frac{A}{\sqrt{2\pi\sigma^2}}\exp\left(-\frac{(k-\mu)^2}{2\sigma^2}\right), \tag{6.2.2}$$

with a mean value μ and a standard deviation σ. In addition, the normalization constant A was introduced to account for the fact that the histograms are not normalized.

The resulting Gaussian fits can be seen in blue in figure 6.7. Overall, they seem to provide good descriptions of the data. The resulting fit parameters for each of the four pairs can be found in table 6.3. The mean of the fitted distribution is negative for each of the four pairs, indicating less counts in the analysis regions closer to Wd 1 than in the test regions. This result seems to be in line with the negative trend visible for some of the residua plots in figure 6.6.

Finally, I also performed t-tests to check whether the mean of the measured residua histogram is significantly negative, indicating more counts in the test than in the analysis regions. t-tests can be used to compare either the averages of two samples or to test whether the average of one sample significantly deviates from a given null hypothesis sample mean. Strictly speaking, they require the tested samples to be normally distributed, which is approximately valid here. Specifically, I use the t-test for one sample, in this case the residua histograms. The t-statistic is given by

$$t = \frac{\mu_{\text{sample}} - \mu_{\text{pop}}}{\sigma_{\text{sample}}/\sqrt{n}}, \tag{6.2.3}$$

where μ_{pop} is the population mean given by the null hypothesis, μ_{sample} is the observed sample mean, and σ_{sample} is the estimated sample standard deviation. This t-statistic can then be compared to the number of degrees of freedom ν to derive a p-value for the null hypothesis.

Here, ν always equals 874. I define the null hypothesis as $\mu_{\text{pop}} \geq 0$ with the alternative hypothesis $\mu_{\text{pop}} < 0$. I choose a confidence level of 0.997, corresponding to about 3σ. Consequently, for a p-value $p < 0.003$ the null hypothesis has to be abandoned in favor of the alternative hypothesis, indicating that the test regions do contain significantly more counts than the analysis regions.

The resulting t-statistics and p-values for each pair of an analysis and test region are given in the last two columns of table 6.3. The p-values are smaller than 0.003 in each case except for Wd40 and WdT40, which are relatively close with ≈ 0.006. In the case of Wd20 and WdT20 the

Table 6.3: Resulting fit parameters of Gaussian fits to the residua histograms in figure 6.7. The parameters are the normalization A, the mean value μ, and the standard deviation σ. The two last columns give the t-statistic and the p-value of a one-sample left-sided t-test testing the null hypothesis that the mean of the distribution underlying the residua is equal to at least 0. The number of degrees of freedom is 874 in each case.

	A	μ [counts]	σ [counts]	t	p
Wd10/WdT10	827 ± 27	-0.17 ± 0.06	1.50 ± 0.06	-3.664	$1.316 \cdot 10^{-4}$
Wd20/WdT20	848 ± 16	-0.37 ± 0.07	2.71 ± 0.07	-5.333	$6.160 \cdot 10^{-8}$
Wd30/WdT30	860 ± 40	-0.22 ± 0.18	3.44 ± 0.18	-4.235	$1.265 \cdot 10^{-5}$
Wd40/WdT40	834 ± 29	-0.10 ± 0.14	3.36 ± 0.14	-2.506	$6.201 \cdot 10^{-3}$

significance even reaches more than 5σ. Following this overall result, I reject the null hypothesis and accept the alternative hypothesis, which states that the test regions contain more photon counts than the analysis regions. Importantly, this result is also in line with the visual inspection of the residua in figure 6.6 as well as with the Gaussian fits having negative means.

Keeping in mind the assumptions which lead to these results, i.e., the test regions being far enough removed from the analysis regions, the negligible effect of exposure times, and the Gaussian approximation to the Skellam distributions, I conclude that no significant evidence for a nonthermal synchrotron component around Wd 1 is present in the eRASS:4 data. This result for the four analysis regions is in line with an additional analysis of two larger regions discussed in appendix 2. Specifically, these larger regions are constructed from combining the four analysis regions.

Finally, regarding the higher count numbers in the test regions compared to the analysis regions, there are different possible explanations for this. For example, the higher exposure times in the test regions probably cause them to have correspondingly more photon counts. Further, as will be seen in table 6.4 in the next section, the test regions have somewhat smaller column densities of absorbing material than the corresponding analysis regions, even though the values agree within their standard deviations. Quite possibly, this results in an increased X-ray flux in the test regions.

6.3 Background Fits

Following the main result that no significant evidence of a nonthermal component is present in the data, it should be possible to fit the spectra of the analysis regions with pure background models. In fact, such fits are highly informative as they would allow the derivation of upper limits on the flux of a potential synchrotron source component. Therefore, I performed spectral fits to the regions Wd10, Wd20, Wd30, and Wd40, using the `Xspec` software. In general, the contributions to the fit spectra can be separated into three categories:

1. The particle background is not produced by astrophysical X-ray photons incident on the detectors, but by charged particles, e.g., CRs. Luckily, it can be measured in isolation via

the filter wheel CLOSED setting. From such measurements, FWC models were produced for each of the seven TMs as discussed in Yeung et al. (2023). In general, they consist of broken power laws with exponential cutoffs and several Gaussian emission lines. These models should only weakly depend on the analyzed region in the sky and are normalized to a source area of $1\,\mathrm{deg}^2$. Therefore, their normalization factors can be set to the BACKSCAL keywords of the respective spectral fits files, which give the average source area incident with the detector during the good time intervals in deg^2. I list the employed normalization factors in table A1.3.

2. The astrophysical X-ray background is subject to more uncertainty than the particle background as it cannot be measured in isolation from potential source components. Its main contributions are diffuse emission from hot gas in the Galaxy and around it as well as unresolved extragalactic sources. It will be discussed in detail in the next subsection.

3. The stray light contamination from GX 340+0 is specific to this analysis. As discussed before, the point source spectrum of the LMXB can be fitted with an absorbed `diskbb` + `compTT` model. However, figure 6.2 indicates that the shape of the stray light spectrum changes at larger distance from the source. From fits to the background region used for the star cluster Wd 1 itself, I found that the stray light at the distance of Wd 1 to GX 340+0 can be described using a simple `tbabs`·`diskbb` model without the `compTT` component. This will be described in section 7.2. The fit parameters are $N_\mathrm{H}^\mathrm{stray} = 4.32 \cdot 10^{22}\,\mathrm{cm}^{-2}$ and $k_\mathrm{b}T_\mathrm{in} = 9.73\,\mathrm{keV}$. For the background fits to the analysis regions, I used this model with fixed N_H and $k_\mathrm{B}T_\mathrm{in}$ while leaving the normalization η_diskbb free.

6.3.1 X-ray Background

The diffuse X-ray background as seen by eROSITA was studied by Ponti et al. (2023). These authors analyzed the region of the eROSITA Final Equatorial Depth Survey (eFEDS), performed during the calibration and performance verification phase of the telescope. The region has an area of $\approx 142\,\mathrm{deg}^2$ and its position is at a Galactic latitude of $b \approx 220 - 235^\circ$ and a Galactic longitude of $l \approx 20 - 40^\circ$. Consequently, the region is removed from the Galactic plane. In comparison, Wd 1 lies almost exactly on the Galactic plane, making a higher background than found in Ponti et al. (2023) plausible.

In general, these authors achieve a good fit to the background using, apart from the particle background, a model with the following components:

1. **Local hot bubble (LHB):** The Solar system is located inside a bubble filled with hot gas, called the LHB. This cavity was likely produced by past supernova explosions. The LHB extends to a maximum distance of $\approx 100\,\mathrm{kpc}$ from the Sun. Due to its proximity, this component is assumed to be unabsorbed. Regarding its X-ray spectrum, the thermally emitting gas was fitted with an APEC model, i.e., collisionally ionized gas in thermal equilibrium. `Xspec`'s `apec` model has three main parameters: the plasma temperature, which is $k_\mathrm{B}T_\mathrm{LHB} \approx 0.11\,\mathrm{keV}$ for the LHB, the metal abundance with $Z_\mathrm{LHB} = 1Z_\odot$, as well

as a normalization factor. For this study, the temperature and the abundance were fixed to the values given here.

2. **Circumgalactic medium (CGM):** The CGM is assumed to surround the Milky Way in a roughly spherical halo extending to its virial radius of $r_{\mathrm{vir}} \approx 280\,\mathrm{kpc}$. In Ponti et al. (2023), it is fitted with an absorbed `apec` component with temperature $k_{\mathrm{B}}T_{\mathrm{CGM}} = 0.153 - 0.178\,\mathrm{keV}$ and abundance $Z_{\mathrm{CGM}} = 0.05 - 0.10 Z_{\odot}$. Here, these values were set to $k_{\mathrm{B}}T_{\mathrm{CGM}} = 0.16\,\mathrm{keV}$ and $Z_{\mathrm{CGM}} = 0.08 Z_{\odot}$.

3. **Corona:** In addition, Ponti et al. (2023) require the presence of a hotter thermal component, possibly associated with a Galactic corona. The corona's morphology is assumed to be a disk with a scale height of $\sim 1\,\mathrm{kpc}$ around the stellar disk of the Galaxy. Assuming an absorbed `apec` model and $Z_{\mathrm{cor}} = 1 Z_{\odot}$, the authors find a temperature of $k_{\mathrm{B}}T_{\mathrm{cor}} = 0.4 - 0.7\,\mathrm{keV}$. Interestingly, they also discuss a possible contribution of unresolved M dwarf stars expected to reside in the Galactic disk. For this analysis, the chosen values are $k_{\mathrm{B}}T_{\mathrm{cor}} = 0.65\,\mathrm{keV}$ and $Z_{\mathrm{cor}} = 1 Z_{\odot}$.

4. **Cosmic X-ray background (CXB):** The CXB is the component of the diffuse X-ray background stemming from unresolved extragalactic point sources, mainly active galactic nuclei. Due to the distribution of these sources, it is largely isotropic in nature, i.e., its normalization can be fixed in advance. Following Ponti et al. (2023), it was modelled using a `powerlaw` component with a photon index of $\Gamma = 1.46$ and a normalization of $\eta_{\mathrm{CXB}} = 8.88 \cdot 10^{-7}\,\mathrm{keV}^{-1}\,\mathrm{cm}^{-2}\,\mathrm{s}^{-1}\,\mathrm{arcmin}^{-2}$.

5. **Solar wind charge exchange (SWCX):** Further, Ponti et al. (2023) find evidence for X-ray emission from SWCX in their eRASS3 data. SWCX is a process in which highly ionized atoms in the Solar wind ionize neutral atoms in the interplanetary space, followed by the emission of X-rays from the newly ionized particles. Since I considered eRASS:4 data for my analysis, I added SWCX to my model in the form of the `Xspec` `AtomDB` charge exchange component `acx2`[2].

6.3.2 Absorption

The resulting background model contains four components affected by absorption: the CGM, the Galactic corona, the CXB, and the stray light contamination component. The LHB and the SWCX are close enough for absorption to be negligible. Further, the stray light `tbabs` component is set by the phenomenological model described above. For the other three components, I used the HEASARC tool `nh` to determine the column density of neutral hydrogen gas in the four different analysis regions. `nh` uses data from the HI 4 Pi survey described in Dickey and Lockman (1990).

Specifically, `nh` was used to determine the neutral hydrogen column density N_{H} at different locations of roughly equal distance along the annuli of Wd10, Wd20, Wd30, Wd40. For Wd10,

---

[2] https://acx2.readthedocs.io

five positions were chosen, while seven positions were used for each of the other three regions. Following this, the arithmetic mean for each of the four regions was calculated. The results can be found in table 6.4. In addition, the table also gives the identically determined column densities for the test regions WdT10, WdT20, WdT30, and WdT40. They are consistently smaller than the corresponding analysis region values.

I used `Xspec`'s `tbabs` component to model the absorption. For the CXB component, the N_{H} value was fixed to the determined Galactic value, as this X-ray component should be completely extragalactic. Initially, I tried the same for the CGM and the Galactic corona, but this lead to large residua in the final fit and to large differences in the normalizations of the three `apec` components, which were in strong disagreement with the results of Ponti et al. (2023). Therefore, I resorted to using the N_{H} values in table 6.4 as upper limits in the case of the CGM and the corona. Astrophysically, this is justified since Wd 1 lies on the Galactic plane. Therefore, the contribution of Galactic emission, e.g., from M dwarf stars, should be higher than for the eFEDS field.

Table 6.4: Arithmetic means and standard deviations of the neutral hydrogen column densities N_{H} in $10^{22}\,\mathrm{cm}^{-2}$ as well as areas A in arcmin^2 of the eight analysis and test regions. For the areas, the effect of the masking of GX 340+0 is considered.

	Wd10	Wd20	Wd30	Wd40	WdT10	WdT20	WdT30	WdT40
N_{H}	2.02±0.09	1.99±0.17	1.94±0.26	1.81±0.3	1.94±0.05	1.92±0.13	1.86±0.24	1.73±0.4
A	203.39	657.17	1217.1	1488.07	203.39	657.17	1217.1	1488.07

Apart from N_{H}, table 6.4 also gives the areas A of the different analysis regions, taking into consideration the stray light masks. Using these values, the four spectral fits were normalized to a source area of $1\,\mathrm{arcmin}^2$. Therefore, the resulting parameters of the spectral components are more easily comparable to each other.

6.3.3 Resulting Fits

Due to the large extent of the analyzed areas and the high resulting count statistics, I decided not to combine the data from the different TMs. Instead, all TMs were fitted separately, with numbers 5 and 7 being excluded as usual. The parameters of the models used for this were coupled, i.e., could not differ between the different TMs. Still, the X-ray model of each TM is multiplied with a constant weighing factor w given in table A1.3 to account for the different sensitivities of the different cameras.

The data was fitted in the energy range from 0.2 to 9.5 keV to include the high-energy drop off of the FWC models. For TM2 and TM4, a lower threshold of 0.25 keV was used since their FWC models are unreliable below this energy.

For the fit statistic, I chose the Cash statistic (Cash, 1979), and for the test statistic the Pearson

χ^2-statistic

$$\chi_\mathrm{P}^2 = \sum_{i=1}^{N} \frac{(d_i - m_i)^2}{m_i}, \tag{6.3.1}$$

as recommended by the `Xspec` manual. Here, d_i are the data points, m_i are the corresponding model values, and N is the number of data points.

The free parameters of the fits were the column densities of the CGM and the corona, $N_\mathrm{H}^\mathrm{CGM}$ and $N_\mathrm{H}^\mathrm{cor}$, and the normalizations of the LHB, CGM, corona, stray light, and SWCX, η_LHB, η_CGM, η_cor, η_diskbb, η_SWCX. As η_SWCX was consistently set to a normalization ≈ 0 in all fits, I decided to remove the `acx2` component from the fits. As the strength of SWCX depends on the orientation of the telescope during the observation and on the time of the observation, SWCX might indeed be subdominant in the spectra analyzed here.

Following this, the fits were repeated without SWCX and 90% confidence intervals were determined for the fit parameters using the `Xspec` command `error`. Whenever the `error` command found a new best fit, the new fit was accepted and the procedure repeated. Finally, the quality of each fit was calculated using the `Xspec` command `goodness` with settings `sim` and `fit`. This command simulates a number of spectra based on the best fit model and performs new fits to these simulated spectra. Its output is the percentage P of these fits which have a test statistic lower than the initial best fit. The null hypothesis that the initial fit is the correct model can then be rejected at a confidence level P. Consequently, values around $P \approx 50\%$ indicate good fits.

The resulting fit parameters can be seen in figure 6.5 together with the reduced χ_P^2's and the goodness values of the fits. In general, P lies between 0.49 and 0.90, indicating good fits. Regarding the parameters, for Wd10, $N_\mathrm{H}^\mathrm{cor}$ ran into its upper limit of $2.02 \cdot 10^{22}\,\mathrm{cm}^{-2}$ during the calculation of confidence intervals. Also note the large uncertainty on η_CGM, probably related to the large uncertainty on the corresponding column density.

Table 6.5: Fit parameters of background fits to the four analysis regions Wd10, Wd20, Wd30, and Wd40 with 90% confidence intervals. All N_H values are in $10^{22}\,\mathrm{cm}^{-2}$ and all η except for η_diskbb are in $10^{-14}\,\mathrm{cm}^{-5}$. η_diskbb is in $10^{-2}\,\mathrm{km}^2\,\mathrm{kpc}^{-2}$. χ_P^2/ν is the fit's Pearson χ^2 divided by the degrees of freedom and P is the goodness as described in the text.

	Wd10	Wd20	Wd30	Wd40
η_LHB	$6^{+5}_{-6} \cdot 10^{-7}$	$1.03^{+0.28}_{-0.26} \cdot 10^{-6}$	$6.0^{+2.5}_{-2.5} \cdot 10^{-7}$	$8.5^{+2.2}_{-2.7} \cdot 10^{-7}$
$N_\mathrm{H}^\mathrm{CGM}$	$0.9^{+0.4}_{-0.9}$	0.416	$0.26^{+0.20}_{-0.13}$	$0.42^{+0.18}_{-0.21}$
η_CGM	$7^{+70}_{-7} \cdot 10^{-4}$	$5.2^{+1.9}_{-1.8} \cdot 10^{-5}$	$3.2^{+6}_{-1.6} \cdot 10^{-5}$	$1.0^{+1.5}_{-0.7} \cdot 10^{-4}$
$N_\mathrm{H}^\mathrm{cor}$	$1.3^{2.02}_{-0.4}$	$0.94^{+0.15}_{-0.14}$	$1.02^{+0.12}_{-0.10}$	$1.01^{+0.16}_{-0.14}$
η_cor	$1.3^{+1.0}_{-0.7} \cdot 10^{-5}$	$6.1^{+1.8}_{-1.5} \cdot 10^{-6}$	$8.2^{+1.6}_{-1.4} \cdot 10^{-6}$	$7.1^{+1.4}_{-1.2} \cdot 10^{-6}$
η_diskbb	$8.4^{+1.0}_{-0.9} \cdot 10^{-4}$	$2.41^{+0.15}_{-0.15} \cdot 10^{-3}$	$3.35^{+0.19}_{-0.19} \cdot 10^{-3}$	$2.41^{+0.18}_{-0.18} \cdot 10^{-3}$
χ_P^2/ν	$\frac{4485.82}{4349}$	$\frac{4369.06}{4350}$	$\frac{4467.34}{4349}$	$\frac{4456.76}{4349}$
P	0.90	0.49	0.90	0.85

In the case of Wd20, the fit was particularly unstable. In particular, it tended to set $N_{\mathrm{H}}^{\mathrm{CGM}}$ to very low values. This resulted in the CGM component dominating over the LHB component even at very low energies, and therefore in negligibly low values for η_{LHB}. Since the existence of the LHB is well confirmed, this result seems unphysical. Therefore, I fixed the ill constrained $N_{\mathrm{H}}^{\mathrm{CGM}}$ value of Wd20 to $0.416 \cdot 10^{22}\,\mathrm{cm}^{-2}$. This value was obtained from the fit to Wd40, the region with the best statistics.

Otherwise, the fit parameters are consistent within their 90% confidence intervals between the different regions. The only exception is η_{diskbb}, which has particularly small uncertainties. This is likely because this component is still prominent above 3 keV, where all other contributions except for the fixed particle background are negligible.

Comparing the parameters to Ponti et al. (2023), these authors find η_{CGM} to be about an order of magnitude larger than η_{LHB}, while η_{cor} is an order of magnitude lower. For my fits, η_{LHB} is the smallest normalization, with η_{CGM} about one to two and η_{CGM} two to three orders of magnitude larger. This could indicate a stronger contribution from the Galactic disk for my spectra, as might be expected due to the position of the analysis regions.

Indeed, this is in line with the fact that $N_{\mathrm{H}}^{\mathrm{CGM}}$ and $N_{\mathrm{H}}^{\mathrm{cor}}$ are below their upper bounds, indicating emission from within the Galaxy. In particular, for the Galactic corona, a contribution from M dwarf stars is possible. For the CGM, the particularly low values $N_{\mathrm{H}}^{\mathrm{CGM}} \approx 0.3 \cdot 10^{22}\,\mathrm{cm}^{-2}$ indicate that in my model, this component might dominantly describe softly emitting hot gas inside the Galactic disk.

The spectra of the analysis regions Wd10, Wd20, Wd30, Wd40 with their corresponding fits can be seen in figure 6.8. In these plots, the different colors correspond to the data and the models for the five TMs used for this analysis. The FWC models are characterised by power laws with an almost constant slope over the entire ranges of the spectra. As indicated by the residua in the lower part of each panel, the fits provide a reasonable description of the data.

Since the data and the models in figure 6.8 are quite crowded, I also plotted the data and the model of a single TM in figure 6.9. In this case, it is data from Wd40 using only TM1. The overall X-ray and FWC models can be seen in blue. For a better understanding of the different components of the model, they are marked in different colors. The red component prominent at low energies is the `apec` model of the LHB with a temperature of 0.11 keV. Orange is the absorbed CGM `apec` component with a higher temperature of 0.16 keV, while at even higher energies, the absorbed Galactic corona with 6.5 keV dominates. Its `apec` component is marked in green. In this figure, one can clearly see the higher contribution of the CGM and the Galactic corona in comparison to the LHB. Further, the CXB, described by an absorbed `powerlaw` component, is given in purple, and at the highest energies the stray light component is given in yellow.

Overall, reasonable fits to all four analysis regions were achieved using pure background models without additional source components. This corroborates the main result that the eROSITA data does not contain significant evidence for synchrotron radiation in the vicinity of Wd 1.

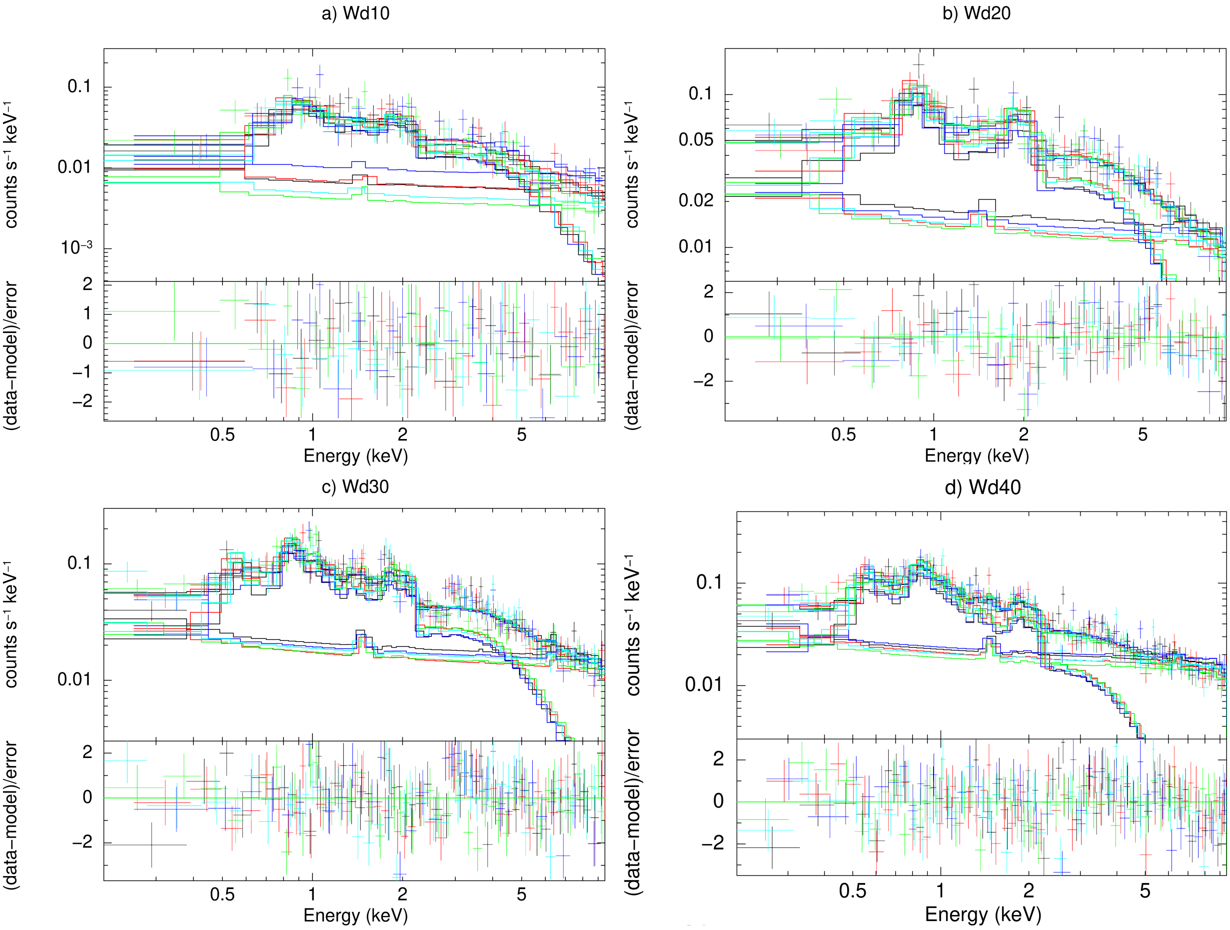

Figure 6.8: Each panel shows the spectrum of an analysis region with the corresponding background fit. The different colors correspond to the data and models for the five different TMs. The lower part of each panel shows the normalized residua of the fit. In each panel, one can clearly distinguish the X-ray background models, which follow the data closely between 0.5 and 2 keV, and the FWC models, which dominate above 4 keV. The different spectra are Wd10 and WdT10, binned to a 3σ significance per bin (*panel a*), Wd20 and WdT20, binned to a 4σ significance per bin (*panel b*), Wd30 and WdT30, binned to a 5σ significance per bin (*panel c*), and Wd40 and WdT40, binned to a 5σ significance per bin (*panel d*).

6.4 Upper Limits

For deriving new constraints on CR acceleration around Wd 1 from SED fits, I calculated upper limits on the flux in energy bands other than VHE γ-rays. In particular, upper limits on the X-ray synchrotron flux were derived from the background fits presented here. Apart from this, upper limits on the radio flux as determined by Aharonian et al. (2022) with Planck data as well as upper limits on the VHE flux as determined by Ohm et al. (2013) were employed.

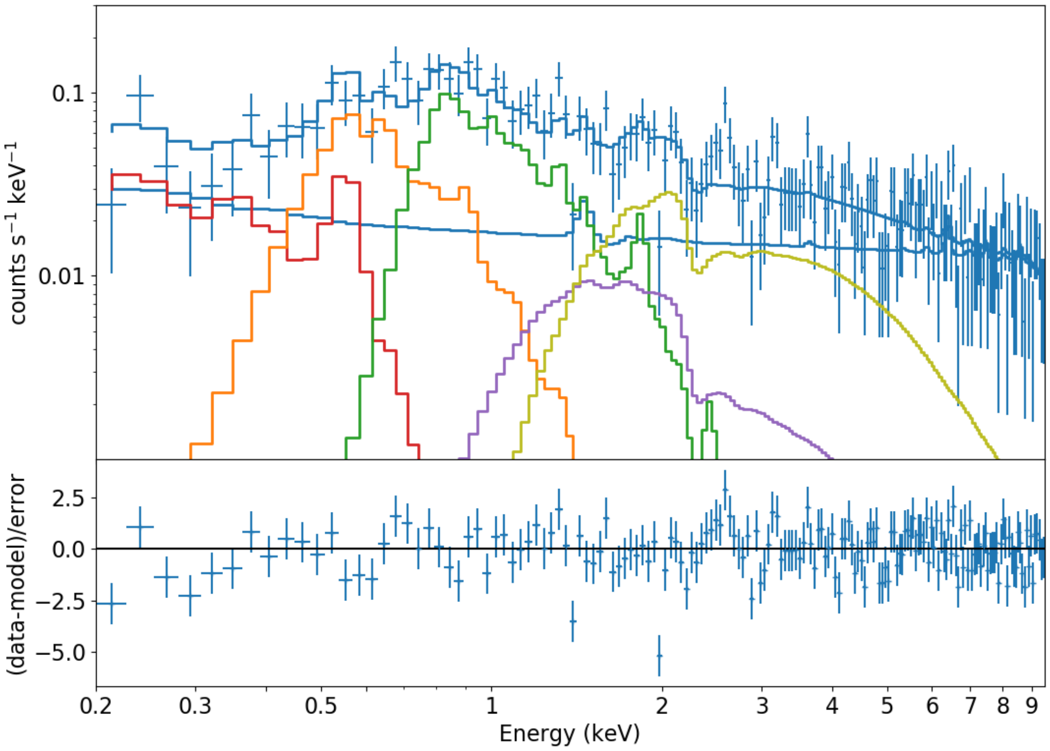

Figure 6.9: Spectrum and background model of the Wd40 region, employing only data from TM1 for a better visibility of the model components. The data is binned to a minimum significance of 5σ per bin. The data, the overall X-ray background model, and the FWC model are given in blue. The LHB is red, the CGM orange, the Galactic corona green, the CXB purple, and the stray light model yellow.

6.4.1 X-ray Upper Limit

For deriving an upper limit on the X-ray synchrotron flux, the four background fits to the analysis regions Wd10, Wd20, Wd30, and Wd40 described in the previous section were used. First, all free parameters were fixed to the best fit parameters listed in table 6.5. Next, I added a power law component to each of the four models. In `Xspec`, a power law is characterized by two parameters: 1. Its photon index Γ and 2. its normalization η_Γ in keV^{-1} cm^{-2} s^{-1}.

Typically, power law indices describing synchrotron emission have values of roughly $\Gamma \approx 2$, as predicted by DSA. Therefore, for each of the four analysis regions, three different fixed values for Γ were considered: 1.5, 2, and 2.5. In total, this results in twelve different cases: four regions with three indices each. For each of these cases, I ran `Xspec`'s `steppar` command on η_Γ. This command varies the specified parameter's value and gives out the resulting fit statistic for each variation.

The results of this can be seen in figure 6.10. One can clearly see how the fit statistics stay approximately constant up to some values η_Γ, corresponding to the parameter values where the additional power law component is subdominant compared to the background model parameters. Above this values, the fit statistics increase rapidly, indicating worse fits. This corresponds to power law components so strong that the models do not longer provide good fits to the data.

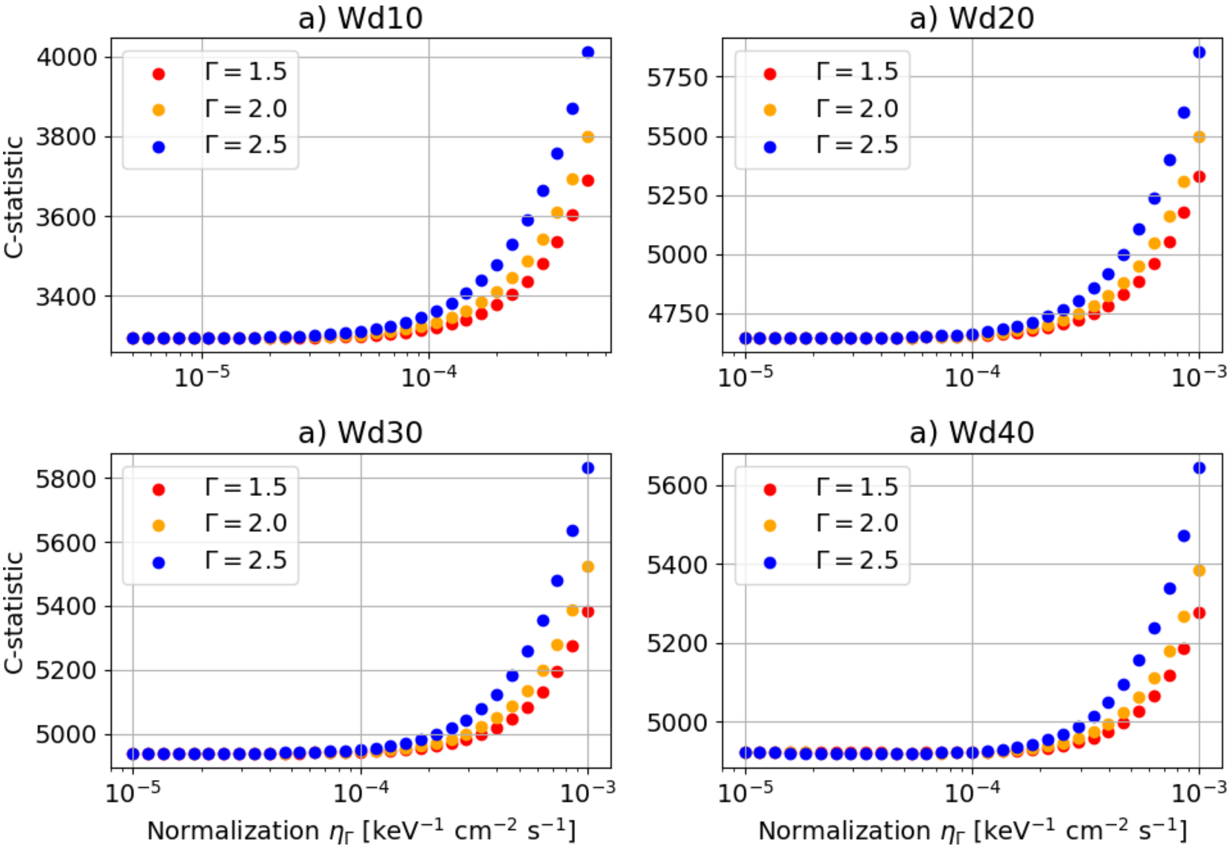

Figure 6.10: Fit statistics for the fixed background models from section 6.3 in dependence on the normalization of an additional `powerlaw` component. Different colors indicate different values of the power law index Γ as indicated in the legends. The four panels *a*, *b*, *c*, and *d* refer to the four analysis regions Wd10, Wd20, Wd30, and Wd40, respectively.

Second, different colors in the figure correspond to the different power law indices: red to $\Gamma = 1.5$, orange to 2.0, and blue to 1.5. For all four regions, lower power law indices indicate larger possible normalizations η_Γ before the fit statistic worsens notably. Most probably, the reason is that the normalization η_Γ gives the power law flux at an energy 1 keV. For large values η_Γ, discrepancies with the data first appear below this energy. As smaller values of Γ corresponds to harder spectra, i.e., shallower slopes, they have lower fluxes below 1 keV and higher fluxes above it than power laws with larger indices.

For the upper limits on the flux of the nonthermal components, I use the upper limits of the 90% confidence ranges around the η_Γ parameter as determined with the `error` command. These upper limits can be found in table 6.6.

Table 6.6: 90% confidence upper limits on the η_Γ parameter in $\mathrm{keV^{-1}\,cm^{-2}\,s^{-1}}$ for the different analysis regions and the three adopted values for the power law index Γ.

Γ	Wd10	Wd20	Wd30	Wd40
1.5	$4.04 \cdot 10^{-5}$	$5.89 \cdot 10^{-5}$	$8.19 \cdot 10^{-5}$	$1.25 \cdot 10^{-4}$
2.0	$3.16 \cdot 10^{-5}$	$5.72 \cdot 10^{-5}$	$7.18 \cdot 10^{-5}$	$1.15 \cdot 10^{-4}$
2.5	$2.20 \cdot 10^{-5}$	$4.68 \cdot 10^{-5}$	$5.45 \cdot 10^{-5}$	$8.81 \cdot 10^{-5}$

To be conservative in the calculation of a single upper limit on the X-ray synchrotron flux for the entire analysis area, the highest upper limits for each individual region were used. As explained above, this refers to the setting $\Gamma = 1.5$. Therefore, the resulting limits are $\eta_\Gamma^{\mathrm{Wd10}} \lesssim 4.04 \cdot 10^{-5}\,\mathrm{keV^{-1}\,cm^{-2}\,s^{-1}}$ for Wd10, $\eta_\Gamma^{\mathrm{Wd20}} \lesssim 5.89 \cdot 10^{-5}\,\mathrm{keV^{-1}\,cm^{-2}\,s^{-1}}$ for Wd20, $\eta_\Gamma^{\mathrm{Wd30}} \lesssim 8.19 \cdot 10^{-5}\,\mathrm{keV^{-1}\,cm^{-2}\,s^{-1}}$ for Wd30, and $\eta_\Gamma^{\mathrm{Wd40}} \lesssim 1.25 \cdot 10^{-4}\,\mathrm{keV^{-1}\,cm^{-2}\,s^{-1}}$ for Wd40.

As one can tell from the increasing magnitude of these upper limits, the additional synchrotron power law components were not normalized to an area of 1 arcmin^2 for the fits. Therefore, these upper limits do already correspond to the areas of the four analysis regions as given in table 6.4. Summing up the upper limits, I obtain in total

$$\eta_{\mathrm{X}}^{\mathrm{Wd10-40}} \lesssim 3.06 \cdot 10^{5}\,\mathrm{TeV^{-1}\,cm^{-2}\,s^{-1}}, \tag{6.4.1}$$

for an emission area of $A_{\mathrm{X}} = 3565.73\,\mathrm{arcmin}^2$. Coincidentally, this upper limit is already given as a differential flux as required for the SED fits, meaning that no further dimensionality conversion is necessary. However, the area still has to be normalized. For fitting the SED of Wd 1, the VHE data of Aharonian et al. (2022) was used, which was obtained by combining 16 areas of size 0.45° × 0.45°. Summed up, this corresponds to an area of $A_{\mathrm{HESS}} = 11\,664\,\mathrm{arcmin}^2$. Rescaling the X-ray upper limit to this area via multiplying with $A_{\mathrm{HESS}}/A_{\mathrm{X}}$ yields

$$\eta_{\mathrm{X}} \lesssim 1.00 \cdot 10^{6}\,\mathrm{TeV^{-1}\,cm^{-2}\,s^{-1}}. \tag{6.4.2}$$

6.4.2 Radio Upper Limit

In their analysis of the VHE emission around Wd 1, Aharonian et al. (2022) also discuss an upper limit on the radio synchrotron flux obtained from Planck archival data. They consider the flux at a frequency of $\nu_{\mathrm{rad}} = 30\,\mathrm{GHz}$ and find $f_{\mathrm{rad}} \lesssim 0.55\,\mathrm{MJy\,sr^{-1}}$ for the average flux per area in a region of radius 1° around Wd 1.

For using this upper limit in my SED fit, it first has to converted into $\mathrm{TeV^{-1}\,cm^{-2}\,s^{-1}}$. First of all, the frequency $\nu_{\mathrm{rad}} = 30\,\mathrm{GHz}$ corresponds to an energy of $E_{\mathrm{rad}} = h\nu_{\mathrm{rad}} = 1.241 \cdot 10^{-4}\,\mathrm{eV}$.

Regarding the radio flux per area, multiplying this with A_{HESS} yields

$$F_{\mathrm{rad}} \lesssim 5.428 \cdot 10^{2}\,\mathrm{Jy}. \tag{6.4.3}$$

Since $1\,\mathrm{Jy} = 10^{-23}\,\mathrm{erg\,Hz^{-1}\,cm^{-2}\,s^{-1}}$, this has to be converted into a particle flux via dividing by E_{rad}, the energy of the particles under consideration. This way, one obtains

$$\Phi^{\nu}_{\mathrm{rad}} \lesssim 2.730 \cdot 10^{-5}\,\mathrm{Hz}^{-1}\,\mathrm{cm}^{-2}\,\mathrm{s}^{-1}, \tag{6.4.4}$$

which has to be converted into a differential flux per energy Φ^E, not per frequency Φ^ν. Following the relation between E and ν, one has $\Phi^E = \Phi^\nu h^{-1}$, and therefore obtains

$$\Phi_{\mathrm{rad}} \equiv \Phi^{E}_{\mathrm{rad}} \lesssim 6.602 \cdot 10^{21}\,\mathrm{TeV}^{-1}\,\mathrm{cm}^{-2}\,\mathrm{s}^{-1}. \tag{6.4.5}$$

6.4.3 High-energy Upper Limit

As a final ingredient for the SED fit, I use the upper limit on the HE γ-ray flux in the vicinity of Wd 1 obtained by Ohm et al. (2013) with data from Fermi LAT. These authors do not state the upper limit explicitly in their study, but it can be derived from their figure 2, which is reproduced here as figure 4.5. The resulting value is $E_{\mathrm{HE}}^2\Phi_{\mathrm{HE}} \lesssim 1.3 \cdot 10^{-11}\,\mathrm{erg}\,\mathrm{cm}^{-2}\,\mathrm{s}^{-1}$, using the higher limit which considers the emission from J1651.6−4621. For $E_{\mathrm{HE}} = 30\,\mathrm{GeV}$, this corresponds to a differential flux of

$$\Phi_{\mathrm{HE}} \lesssim 9.0 \cdot 10^{-9}\,\mathrm{TeV}^{-1}\,\mathrm{cm}^{-2}\,\mathrm{s}^{-1}. \tag{6.4.6}$$

According to Ohm et al. (2013), this limit was obtained following the spatial H.E.S.S. template from Abramowski et al. (2012). Unfortunately, the precise extent of this template is not provided. Still, following figure 1 from Abramowski et al. (2012), reproduced here as figure 4.2, I estimate the extent of the γ-emission in this study to roughly be half the area of a circle with radius 1.1°, i.e., $A_{\mathrm{HE}} \approx 6842\,\mathrm{arcmin}^2$. Rescaling the HE upper limit via multiplying with $A_{\mathrm{HESS}}/A_{\mathrm{HE}}$, I obtain

$$\Phi_{\mathrm{HE}} \lesssim 1.53 \cdot 10^{-8}\,\mathrm{TeV}^{-1}\,\mathrm{cm}^{-2}\,\mathrm{s}^{-1}. \tag{6.4.7}$$

6.5 Spectral Energy Distribution Fit

Using these upper limits, I fitted the SED of the emission coming from the vicinity of Wd 1. For this purpose, I used the VHE γ-ray spectral data for J1646−458 obtained by H.E.S.S. and presented in Aharonian et al. (2022). Unfortunately, the raw data used in this study is not publicly available. Therefore, I read off the data from figure 7 of Aharonian et al. (2022), reproduced here as figure 4.4. More precisely, this figure gives the photon energy E on the x-axis and the differential VHE flux $\mathrm{d}N/\mathrm{E}$ times E^2 on the y-axis. Therefore, after reading off E and $E^2\mathrm{d}N/\mathrm{E}$, I divided the latter by E^2 to obtain the differential fluxes. In addition, I also read of the error bars and transformed them into differential fluxes in the same way. To sum up, the data used for the SED fits encompasses upper limits on radio, X-ray, and HE fluxes, as well as H.E.S.S. data in the VHE range.

For performing the SED fits, the `Naima` code[3] was used (Zabalza, 2015). `Naima` allows Markov chain Monte Carlo fits of different nonthermal radiation models to data over a wide spectral

---

[3] https://naima.readthedocs.io

range, implemented via the `emcee` package (Foreman-Mackey et al., 2013). The nonthermal models include synchrotron radiation, bremsstrahlung, IC scattering, and pion decay, as discussed in section 2.4. Importantly, `Naima` does not only allow direct fits to the spectra, but it also allows to fit the leptonic and hadronic particle distributions responsible for the nonthermal radiation.

The main new result of this study is the upper limit on the synchrotron X-ray flux around Wd 1. Since synchrotron flux is negligible in a hadronic emission scenario, I focused my SED fits on a leptonic scenario. To this end, I chose a standard exponential cutoff power law electron distribution

$$\frac{\mathrm{d}N}{\mathrm{d}E_\mathrm{e}} = \Phi_0^\mathrm{e}\left(\frac{E_\mathrm{e}}{1\,\mathrm{TeV}}\right)^{-\Gamma} \exp\left(-\frac{E_\mathrm{e}}{E_\mathrm{c}}\right). \tag{6.5.1}$$

Here, N is the number of electrons, E_e is their energy, Φ_0^e is the normalization of the distribution, Γ the power law index, and E_c the cutoff energy.

The assumed γ-ray production mechanism was IC scattering, implemented in `Naima` following Khangulyan et al. (2014). On the other hand, bremsstrahlung is subdominant in most astrophysical systems and in particular it is dependent on the presence of dense gas. Therefore, bremsstrahlung was neglected. To be consistent with Aharonian et al. (2022), a distance to Wd 1 of 3.9 kpc was used as well as the following target photon fields for IC scattering: the CMB, infrared radiation with a temperature of 26 K and an energy density of $0.74\,\mathrm{eV\,cm^{-3}}$, optical star light with 2400 K and $1.4\,\mathrm{eV\,cm^{-3}}$, and radiation from Wd 1 with 40 000 K and $30\,\mathrm{eV\,cm^{-3}}$.

Further, synchrotron radiation was added to the model, which is implemented in `Naima` according to Aharonian et al. (2010). The synchrotron radiation is produced by the same electron population as the γ-rays, which is described by the parameters Φ_0^e, Γ, and E_c. The only additional parameter required by the synchrotron radiation is the magnetic field strength B.

As initial fit parameters, I used the best leptonic fit parameters of Aharonian et al. (2022) and a magnetic field strength of 2 μG. These parameters, together with my resulting fit parameters, are given in table 6.7. Note that a direct comparison to the parameters obtained by Härer et al. (2023) was not performed, as these authors used the `Gamera` code and time-evolved an initial particle distribution. Therefore, their fit parameters are not directly comparable to the ones obtained with `Naima`. Still, their parameters are consistent with Aharonian et al. (2022), meaning that consistency of the parameters presented here with one of these studies implies consistency with the other one, too.

The obtained best fit parameters are consistent with the Aharonian et al. (2022) parameters within their 2σ bounds for Φ_0^e and Γ, and within 1σ for E_c. This seems unsurprising since the only non-upper limit data used in the fit comes from Aharonian et al. (2022). The large uncertainty of E_c likely stems from the large measurement uncertainties of the highest energy H.E.S.S. data points.

The resulting SED is depicted in figure 6.11. Synchrotron emission is in green while IC γ-rays are in blue. Note how the synchrotron component clearly shows a spectral break due to synchrotron self absorption around 10^{-7} eV and an exponential cutoff around 10^{3} eV. Further, the different contributions to the γ-rays by different target photon fields are given in black via different line styles: the CMB is solid, infrared is dashed, optical light is dashed-dotted, and

Wd 1's contribution is dotted.

The IC model closely follows the red VHE H.E.S.S. data, which is the only data not being an upper limit. Therefore, it likely determines the three fit parameters Φ_0^{e}, Γ, and E_{c}. Surprisingly, the HE upper limit in green lies below the IC model. This will be discussed in more detail in the next section. On the other hand, the X-ray upper limit in orange and the radio upper limit in blue lie above the synchrotron model as expected.

The only additional parameter in the synchrotron model is B, with the three other ones likely being determined by the VHE data. As one can see from figure 6.11, the synchrotron flux still has some leeway below the X-ray upper limit. In fact, the magnetic field can be increased up to a value of $\approx 2\,\mu\mathrm{G}$ without violating the limit. Therefore, I adopt $B \lesssim 2\,\mu\mathrm{G}$ as the upper limit on the magnetic field strength in a leptonic emission scenario.

Table 6.7: Resulting fit parameters of the leptonic SED fit in comparison to the parameters obtained by Aharonian et al. (2022). Together with a magnetic field strength of 2 μG, the latter parameters were used as initial parameters for my fit. Uncertainties are given as 1σ confidence ranges.

	Φ_0^{e} [eV^{-1}]	Γ	E_{c} [TeV]	B [μG]
This study	$3.6^{+0.3}_{-0.3} \cdot 10^{35}$	$2.84^{+0.04}_{-0.06}$	120^{+40}_{-40}	$1.4^{+0.5}_{-0.8}$
Aharonian et al. (2022)	$4.7^{+0.5}_{-0.5} \cdot 10^{35}$	$2.97^{+0.03}_{-0.07}$	180^{+200}_{-70}	

6.6 Discussion

The main result of this study is the non-detection of synchrotron radiation around Wd 1 with the eROSITA X-ray telescope. This non-detection, based on the comparison of the four analysis regions to test regions, Gaussian residua fits to the differences between those regions' spectra, as well as t-tests is consistent with the possibility to fit the analysis region spectra with pure background models. Consequently, the synchrotron flux from the analysis regions remains constrained only by an upper limit, albeit a considerably lower one than the previous Planck radio upper limit. In the following, the SED fit presented above is discussed in the light of the literature on Wd 1 and with respect to its implications for the VHE emission scenario of J1646−458.

6.6.1 Magnetic Field Strength

First of all, in the context of a leptonic emission scenario where the bulk of the γ-rays stem from IC scattering, the upper limit of $\eta_{\mathrm{X}} \lesssim 1.00 \cdot 10^{6}\,\mathrm{TeV}^{-1}\,\mathrm{cm}^{-2}\,\mathrm{s}^{-1}$ on the X-ray flux from the region of J1646−458 implies an upper limit on the magnetic field strength of $B \lesssim 2\,\mu\mathrm{G}$. As previously discuss, the preferred acceleration site in a leptonic scenario is the cluster wind termination

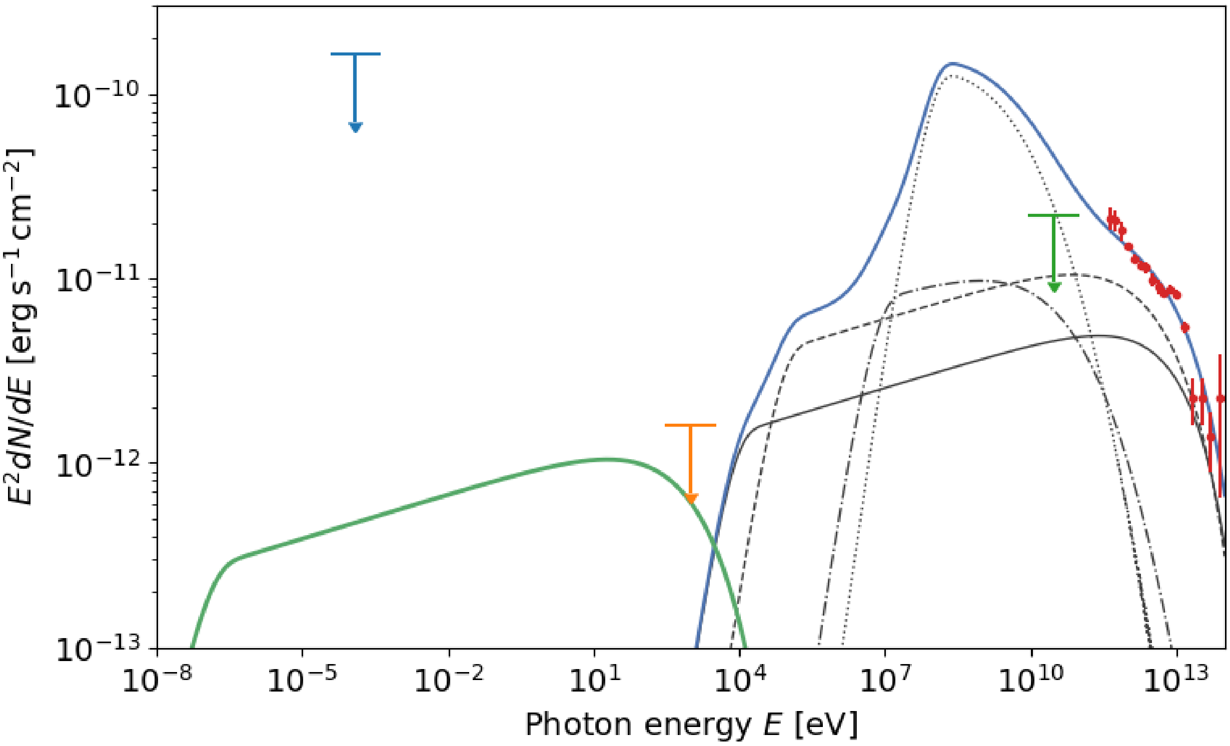

Figure 6.11: Resulting SED fit to the vicinity of Wd 1 using a leptonic model with IC scattering in blue and synchrotron radiation in green. The fit parameters are given in the first row of table 6.7. The contributions of the different IC target photon fields are the CMB (solid line), infrared radiation (dashed), optical star light (dashed-dotted), and Wd 1 (dotted). The blue, orange, and green upper limits are Planck radio data, eROSITA X-ray data, and Fermi LAT HE data, respectively. H.E.S.S. VHE data is given in red.

shock, since it can account for the morphology of the VHE source. Therefore, the upper limit on B relates to the magnetic field strength around the cluster wind termination shock.

Comparing this result with the literature, strong limits on the magnetic field B_{acc} strength around the termination shock are also obtained by Härer et al. (2023) for a leptonic cluster wind termination shock scenario. Specifically, these authors find $0.7\,\mu\mathrm{G} \lesssim B_{\mathrm{acc}}$ and $B_{\mathrm{acc}} \lesssim 4.5\,\mu\mathrm{G}$ based on the Hillas criterion and the requirement of a strong shock with an Alfvén Mach number $\mathcal{M}_{\mathrm{A}} > 1$, respectively.

The upper limit $B \lesssim 2\,\mu\mathrm{G}$ obtained here is more restrictive than the previous upper limit, though consistent with the range allowed by Härer et al. (2023). Interestingly, these authors do in fact assume $B_{\mathrm{acc}} = 2\,\mu\mathrm{G}$ for their analysis of Wd 1. From this point of view, it might then not seem surprising that eROSITA failed to detect synchrotron emission from J1646−456, assuming that the estimation presented by Härer et al. (2023) is reasonable.

Further, since the upper limit of these authors is already more restrictive than the upper limit of 10 μG obtained by Aharonian et al. (2022) using Planck data, my new upper is also consistent with this one. However, one should be careful in comparing this limit on B with the fit presented here, since Aharonian et al. (2022) derived this limit via extrapolating their leptonic fit model described in table 6.7 to lower energies. In particular, they calculated the synchrotron flux expected around 30 GHz assuming 10 μG and their fit parameters.

Since my fit parameters are different from the ones obtained by these authors, my upper limit on B based on radio data should be different, too. Indeed, by increasing the B parameter of my fit I found the maximum possible value for the magnetic field to be $\approx 28\,\mu\mathrm{G}$, around three times higher than for Aharonian et al. (2022). The main reason for this seems to be the lower power law index of 2.84 inferred in this study, as compared to their value of 2.97. This leads to a harder synchrotron component in my fit with a lower flux around 30 GHz. Consequently, the leverage between the model and the Planck upper limit is larger for here than for Aharonian et al. (2022), thus also allowing for a larger magnetic field strength.

Note that the large gap between the radio flux measured by Planck and the maximum possible synchrotron contribution allowed by the limit $B \lesssim 2\,\mu\mathrm{G}$ still implies a negligible contribution of J1646−458 to the radio emission around 30 GHz. In this frequency range, the main contribution is expected to be synchrotron radiation from electrons diffusing through the Galaxy and its halo (Martire et al., 2022). Connecting the radio upper limit with the eROSITA X-ray upper limit then requires a stark drop in the spectral shape of this synchrotron component. Interestingly, such a decline was found by Klein et al. (2018) in the analysis of the synchrotron continuum spectra of 14 star-forming galaxies. Most of these spectra require cutoffs or breaks to larger spectral indices in the range of 1.5 to 7 GeV. As a possible explanation, these authors suggest radiative losses of high-energy CR electrons before they leave the galactic halos.

6.6.2 Very-high-energy Emission Scenario

The previous discussion focused on a leptonic emission scenario. On the other hand, in a hadronic scenario, fulfilling the synchrotron upper limit is trivial since no detectable synchrotron flux is expected from protons anyways. For this reason, an additional hadronic fit is not presented in this thesis, as it would not add much new information to the fits performed by Aharonian et al. (2022) and Härer et al. (2023).

As a consequence, while the results obtained in this thesis provide stronger constraints on the synchrotron flux and the magnetic field strength around Wd 1 than available before, they do not provide strong evidence for or against a particular acceleration scenario. In particular, since my upper bound on B agrees well with the limits obtained by Härer et al. (2023), the leptonic emission scenario at the cluster wind termination shock discussed in this article is still as viable as before.

At the same time, the scenario of hadronic acceleration inside the cluster itself also remains a possibility since no synchrotron flux is expected in this case. Still, one should keep in mind that this scenario suffers from a lack of observed spatial correlation between VHE γ-rays and the dense material in the ISM around Wd 1. On a final note, the true emission scenario of J1646−459 does not need to be one of the two extreme cases, but it could also be a hybrid scenario with relevant contributions from leptons as well as from hadrons.

6.6.3 High-energy Upper Limit

Finally, it is worth discussing the Fermi LAT HE upper limit in greater detail since it is violated by the leptonic fit in figure 6.11. As the fit presented here is based on the leptonic model of Aharonian et al. (2022), this violation should already be present there. Unfortunately, however, the Fermi LAT upper limit is neither discussed by these authors nor by Härer et al. (2023).

Judging by the dotted black line in figure 6.11, the main driver of the discrepancy is the photon target field provided by the star cluster Wd 1 itself. Its large energy density of 30 eV cm^{-3} causes it to violate the HE upper limit. By varying this parameter, I found that restoring agreement with the upper limit would require an energy density of $\approx 2\,\text{eV}\,\text{cm}^{-3}$. This is an order of magnitude below the estimates of Aharonian et al. (2022), namely 30 eV cm^{-3}, and Härer et al. (2023), namely 42 eV cm^{-3}. Further, while Härer et al. (2023) consider a range of temperatures for the cluster photon fields, these different temperatures do only change the widths of the IC contribution and cannot restore the agreement with the upper limit.

Apart from that, I see at least three different explanations for the apparent discrepancy, which are not mutually exclusive: First of all, it is well possible that I might have missestimated the size of the area used for obtaining the HE upper limit in Ohm et al. (2013). These authors state that they employed the VHE template by Abramowski et al. (2012), but they do not provide the precise size of this template. Based on the extent of the γ-ray emission in figure 4.2, I assumed an area of about half a circle with radius 1.1°. If the actual area was smaller than this, the value of the upper limit would increase accordingly. To restore agreement with the model, a relatively modest increase of the limit of about a factor 2 is necessary, meaning that the true area would need to be two times smaller than assumed here.

Second, the value of the upper limit by Ohm et al. (2013) is model dependent. In particular, these authors assumed a power law model with a spectral index of 2. However, in the case of the leptonic fit in figure 6.11, the steep slope in the HE range implies an index significantly larger than 2. As demonstrated by the derivation of X-ray upper limits in this thesis, different power law indices Γ can result in different limits. In particular, if the data points which dominantly determined the Fermi LAT upper limit were at higher energies than the reference energy for the fit model's normalization, then a higher power law index would have resulted in a larger upper limit.

Third, it is worth noting that in a hadronic model, accommodating the upper limit is easier since the steep emission peak from the Wd 1 cluster photon field is absent. Instead, the differential flux is expected to rise not significantly above the highest value indicated by the lowest energy VHE data point given in figure 6.11. Even in an only partly hadronic scenario, this might ease the apparent discrepancy.

CHAPTER 7

Analysis of Westerlund 1

und heißt dann: schweigen und walten,
wissend, daß sie zerfällt,
dennoch die Schwerter halten
vor die Stunde der Welt.

Gottfried Benn, Dennoch die Schwerter halten

7.1 Region Definitions

Apart from the diffuse emission around Wd 1, I also analyzed the diffuse emission of the star cluster itself using eROSITA data. Depending on the characteristics of this emission, e.g., if it is thermal or nonthermal, it might allow to infer new information about the physical nature of its source. In particular, young stellar clusters are expected to produce X-rays via the magnetic activity of young stellar objects, the winds of massive stars, and the activity of compact objects. Further, a part of the emission could stem from accelerated CRs produced at stellar winds or supernova shocks.

In that regard, the analysis presented here follows the works of Muno et al. (2006) and Kavanagh et al. (2011), the first one of which find that the diffuse emission of Wd 1 can be fitted either with two thermal `apec` components or with an `apec` and a nonthermal `powerlaw` component. For the rest of this thesis, these fits will be referred to as the 2APEC and the APEC+PL model, respectively. Later on, Kavanagh et al. (2011) reported a preference for the 2APEC model due to the detection of a 6.7 keV emission line in the diffuse spectrum. This line can be attributed to a K-shell transition in helium-like iron (Fe XXV), which indicates the emission to be thermal.

For the spectrum extraction, source and background regions were defined as shown in figure 7.1 in white and green, respectively. For the source region, I chose a circle centered on $(\alpha, \delta) =$

(251.77°, −45.85°) with a radius of 3 arcmin, corresponding to Wd 1's optical radius. Note that I did not use the event file with masked point sources for extracting the source spectrum, as Wd 1 is largely masked in this event file. Instead, only the bright magnetar CXOU 164710.2−455216 was manually excluded with a mask of radius 0.42 arcmin centered on $(\alpha, \delta) = (251.79°, -45.87°)$. This mask can be seen as the smaller white circle in figure 7.1.

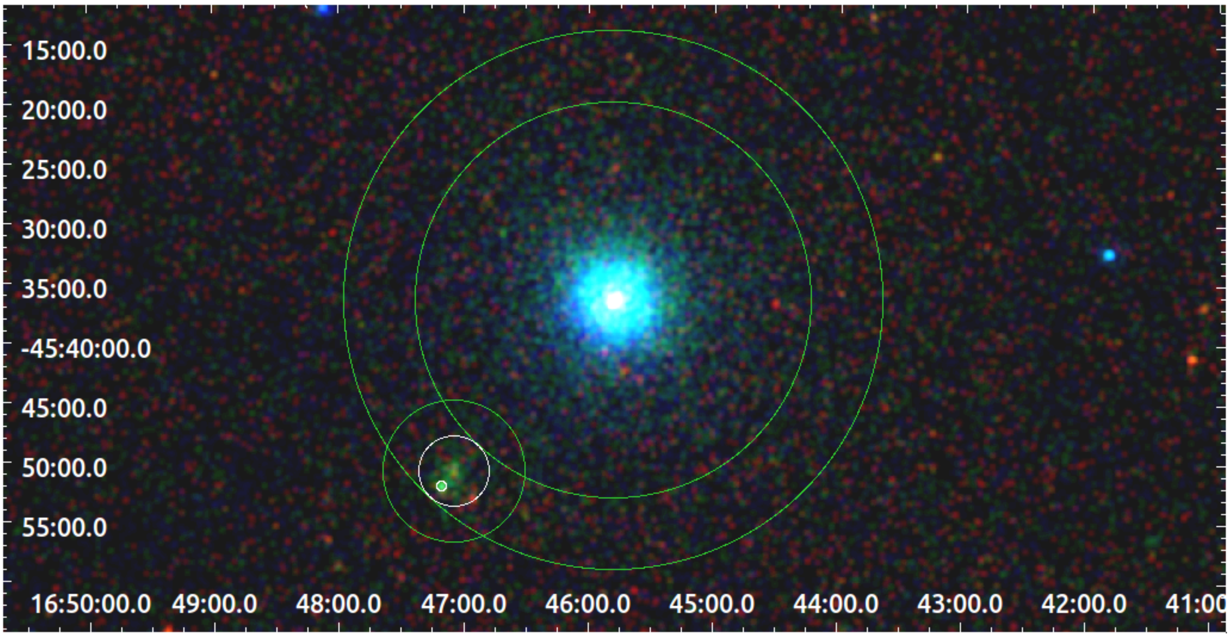

Figure 7.1: The source region for the spectral analysis of Wd 1 is given by the larger white circle, while the smaller white circle marks the mask used on CXOU 164710.2−455216. On the other hand, the large green annulus minus the smaller green circle shows the background region employed for this analysis. The image was smoothed using a Gaussian kernel with a standard deviation of 2.5 arcsec. Note that only for the background spectrum extraction the event file with masked point sources was used.

For the background region, it is important to use a region with a similar stray light contamination from GX 340+0 as the source region. Therefore, a region with the same distance from the LMXB as Wd 1 was chosen. For obtaining optimal statistics, the annulus of width 6 arcmin around GX 340+0 which overlaps with the source region was used. Specifically, this background region is centered on $(\alpha, \delta) = (251.45°, -45.61°)$ and has an inner and outer radius of 16.62 arcmin and 22.62 arcmin, respectively. Further, a circular region around Wd 1 was excluded from the background region. It is centered on $(\alpha, \delta) = (251.77°, -45.85°)$, just like the source region, and has a radius of 6 arcmin.

As before, I used the eSASS task `srctool` for extracting the source and the background spectra. In both cases, the source extent type TOPHAT was chosen and no point spread function was specified.

Lastly, the areas A in arcmin^2, the values of the BACKSCAL keywords in deg^2, and the column densities N_H of the source and the analysis region are listed in table 7.1. The area A is required for normalizing the fits to an area of 1 arcmin^2, as done for the spectral fits to the analysis regions around Wd 1, and the BACKSCAL values are required for setting the normalization of the FWC models. As before, I determined the N_H values with the `nh` tool. For the background region, the arithmetic mean of eleven evenly distributed N_H values in the region was calculated. For the source region, only one N_H value was used due to the region's small extent.

Table 7.1: Areas A, values of the BACKSCAL keyword, and N_H values for the source and the background region. The first two parameters were taken from the headers of the respective spectral fits files. The spectra combining all TMs except numbers 5 and 7 were used due to the low statistics in the source region. The N_H value of the background region is given with an uncertainty derived from the variance of the eleven N_H values from which it was calculated.

	A [arcmin^2]	BACKSCAL [deg^2]	N_H [10^{22} cm^{-2}]
Source region	28.57	0.00642	2.200
Background region	672.07	0.0593	2.11 ± 0.10

7.2 Background Fit

Since the source region is relatively small and Wd 1 is not particularly bright, its spectrum has relatively low statistics. Therefore, the spectra of the different TMs were not fitted separately as for the analysis of the surroundings of Wd 1. Rather, the combined spectrum of all TMs except TM5 and TM7 was used. Further, the background spectrum was not subtracted from the source region, but it was fitted separately. This allowed me to fit the source spectrum with a combination of the fixed background model and a free source model. Both spectra were fitted in the energy range from 0.2 to 9.5 keV using the Cash fit statistic and the Pearson χ^2 test statistic.

As before, I used a FWC model by Yeung et al. (2023), this time for the combination of all TMs except for the numbers 5 and 7. The normalization of this model was fixed to the spectrum's BACKSCAL parameter, given in table 7.1. Also given in this table is the area of the background region used for normalizing the X-ray background model to an area of 1 arcmin^2.

The X-ray background model is largely defined as in section 6.3. In particular, this entails the following components:

1. The LHB, described by an `apec` model with temperature 0.11 keV and a Solar metal abundance $1Z_\odot$.

2. The absorbed CGM, described by an `apec` model with temperature 0.16 keV and a metal abundance of $0.08Z_\odot$. The N_H value given in table 7.1 was used as an upper limit for the absorbing `tbabs` component.

3. The absorbed Galactic corona, described by an `apec` model with temperature 0.65 keV and a Solar metal abundance $1Z_\odot$. The N_H value given in table 7.1 was used as an upper limit for the absorbing `tbabs` component.

4. The absorbed CXB, described by a `powerlaw` model with spectral index 1.46 and normalization $8.88 \cdot 10^{-7}\,\mathrm{keV}^{-1}\,\mathrm{cm}^{-2}\,\mathrm{s}^{-1}\,\mathrm{arcmin}^{-2}$. The N_H value given in table 7.1 was used as a fixed parameter for the absorbing `tbabs` component.

5. A `diskbb` component absorbed by a `tbabs` component to model the stray light contamination from GX 340+0. For this background fit, the parameters of these components were not fixed but rather left free. The parameters determined this way were then used for the fits described in section 6.3.

As before, I dropped an additional SWCX component since it was consistently set to a normalization of ≈ 0. In total, the fit parameters were the column densities of the CGM and the corona, $N_\mathrm{H}^\mathrm{CGM}$ and $N_\mathrm{H}^\mathrm{cor}$, and the normalizations of the LHB, CGM, and corona, η_LHB, η_CGM, η_cor. Further, the stray light model's free parameters were its column density $N_\mathrm{H}^\mathrm{stray}$, and the `diskbb` component's inner disk temperature $k_\mathrm{B}T_\mathrm{in}$ and its normalization η_diskbb. Note that, as before, η_diskbb is not normalized to a source area of $1\,\mathrm{arcmin}^2$.

The resulting fit parameters can be found in table 7.2, while the spectral data and the final model can be seen in figure 7.2. As before, the `error` command of `Xspec` was used to calculate the 90% confidence intervals of the parameters and to find potential better fits. The resulting reduced χ^2_P was 918.41/897 and the goodness of the fit as evaluated by the `goodness` command of `Xspec` was $P = 0.67$. The fit parameters are largely in line with the ones found for the background fits to Wd10, Wd20, Wd30, and Wd40. Therefore, the discussion presented in section 6.3 is also applicable here.

Table 7.2: Resulting parameters of the fit to the background region defined for the star cluster Wd 1. The uncertainties give the 90% confidence intervals of the parameters. If an uncertainty is given without a plus or minus sign, it indicates the upper limit on the parameter allowed by the fit.

Component	Parameter	Unit	Value	Confidence Interval (90%)
LHB	η_LHB	$10^{-14}\,\mathrm{cm}^{-5}$	$1.0^{+0.4}_{-0.6} \cdot 10^{-6}$	$(0.4 \cdot 10^{-6}, 1.4 \cdot 10^{-6})$
CGM	$N_\mathrm{H}^\mathrm{CGM}$	$10^{22}\,\mathrm{cm}^{-2}$	$0.4^{+0.3}_{-0.4}$	$(0, 0.7)$
	η_CGM	$10^{-14}\,\mathrm{cm}^{-5}$	$9^{+30}_{-8} \cdot 10^{-5}$	$(1 \cdot 10^{-5}, 39 \cdot 10^{-5})$
Corona	$N_\mathrm{H}^\mathrm{cor}$	$10^{22}\,\mathrm{cm}^{-2}$	$1.16^{+0.23}_{-0.20}$	$(0.96, 1.39)$
	η_cor	$10^{-14}\,\mathrm{cm}^{-5}$	$1.4^{+0.6}_{-0.4} \cdot 10^{-5}$	$(1.0 \cdot 10^{-5}, 2.0 \cdot 10^{-5})$
Stray light	$N_\mathrm{H}^\mathrm{stray}$	$10^{22}\,\mathrm{cm}^{-2}$	$4.3^{+0.7}_{-0.5}$	$(3.8, 5.0)$
	$k_\mathrm{B}T_\mathrm{in}$	keV	10^{100}_{-6}	$(4, 110)$
	η_diskbb	$10^{-2}\,\mathrm{km}^2\,\mathrm{kpc}^{-2}$	$4^{+20}_{-4} \cdot 10^{-3}$	$(0 \cdot 10^{-3}, 24 \cdot 10^{-3})$

Noteworthy are the large uncertainties on $k_\mathrm{B}T_\mathrm{in}$ and η_diskbb. In fact, the first one of these parameters even ran into its upper limit of 100 keV during the error calculation. The uncertainty of these parameters might be connected to the fact that I found the fit to be relatively degenerate regarding their values: Similarly good fits were possible for large values of $k_\mathrm{B}T_\mathrm{in}$ combined with small values for η_diskbb and for the other way around.

Finally, the precise values to which the stray light model converged are $N_\mathrm{H}^\mathrm{stray} = 4.32 \cdot 10^{22}\,\mathrm{cm}^{-2}$ and $k_\mathrm{b}T_\mathrm{in} = 9.73\,\mathrm{keV}$, which were used as fixed values for the stray light components of the fits to Wd10, Wd20, Wd30, and Wd40 in section 6.3.

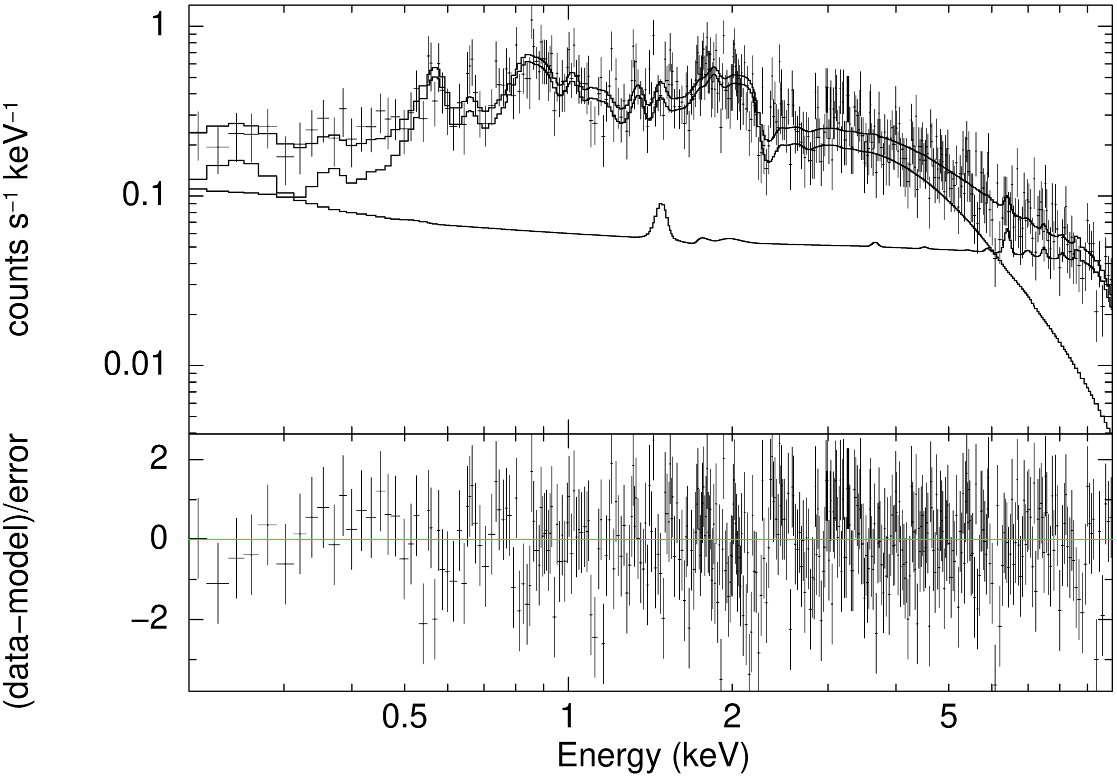

Figure 7.2: *Upper panel:* Spectral data of the background region chosen for the analysis of the diffuse emission of Wd 1. The black lines give the X-ray background model, which drops off rapidly at high energies, the FWC model, which is a relatively hard power law over the entire energy range, and the sum of those two. I rebinned the data to a minimum significance of 3σ for better visibility. *Lower panel:* Residua of the fit divided by the uncertainty of each data bin.

7.3 2APEC Model

The models used for fitting the source region of Wd 1 consisted of the background model defined as described above and fixed to the fit parameters in table 7.2 as well as of additional source components. The only background parameters left free to vary were $N_\mathrm{H}^\mathrm{CGM}$ and $N_\mathrm{H}^\mathrm{cor}$, since the column density of absorbing hydrogen is expected to vary over the sky. As before, I normalized the resulting combined source and background model to the area of the source region. Further, I rescaled the η_diskbb parameter obtained from the background fit to the source region area before fixing it.

This procedure was the same for the 2APEC and for the APEC+PL model. In the case of the 2APEC model, the additional source model is the sum of two `apec` components absorbed by a `tbabs` component. These source components, too, were normalized to a source area of 1 arcmin^2.

The final fit parameters were the column densities of the CGM, the Galactic corona, and the source component, $N_\mathrm{H}^\mathrm{CGM}$, $N_\mathrm{H}^\mathrm{cor}$, and $N_\mathrm{H}^\mathrm{2APEC}$, the temperatures of the two `apec` components, $k_\mathrm{B}T_1$ and $k_\mathrm{B}T_2$, and their normalizations, η_APEC1 and η_APEC2. Since the metal abundances of the two `apec` components were not well constrained by the fit, they were fixed to $Z_1 = 2Z_\odot$ and $Z_2 = 0.62Z_\odot$ to be consistent with Muno et al. (2006) and Kavanagh et al. (2011).

The resulting fit had a reduced Pearson χ^2 of $\chi_\mathrm{P}^2/\nu = 1743.02/1803$. Running the `goodness` command resulted in $P = 0.32$. However, this required me to freeze the parameter $k_\mathrm{B}T_2$ first, which the fit had become insensitive to. The final fit parameters can be found in table 7.3. Different form the rest of this thesis, they are given with 1σ confidence intervals to be consistent with Muno et al. (2006) and Kavanagh et al. (2011). The resulting fit can be seen in figure 7.3, which also shows the corresponding background fit in red for comparison. One can clearly see the larger flux of the background spectrum which results from the background region's larger extent. As described above, this was taken care of via normalizing the background component in the source fit to the correct area.

Table 7.3: Fit parameters of the 2APEC source model compared to literature values. All normalizations and fluxes were normalized to a source area of 1 arcmin^2. Values from Muno et al. (2006) were recalculated to a single source area as described in the text. The uncertainties give the 1σ confidence intervals of the parameters. If an uncertainty is given without a plus or minus sign, it indicates the upper limit on the parameter allowed by the fit.

Param.	Unit	This study	Muno et al. (2006)	Kavanagh et al. (2011)
$N_\mathrm{H}^\mathrm{CGM}$	$10^{22}\,\mathrm{cm}^{-2}$	$0.42^{+0.13}_{-0.09}$		
$N_\mathrm{H}^\mathrm{cor}$	$10^{22}\,\mathrm{cm}^{-2}$	$1.7^{2.2}_{-0.5}$		
$N_\mathrm{H}^\mathrm{2APEC}$	$10^{22}\,\mathrm{cm}^{-2}$	$2.2^{2.2}_{-0.22}$	$2.15^{+0.15}_{-0.15}$	$2.03^{+0.11}_{-0.15}$
$k_\mathrm{B}T_1$	keV	$0.46^{+0.11}_{-0.13}$	$0.90^{+0.14}_{-0.14}$	$0.68^{+0.12}_{-0.13}$
η_APEC1	$10^{-14}\,\mathrm{cm}^{-5}$	$1.4^{+1.2}_{-0.6} \cdot 10^{-4}$	$5.4^{+1.5}_{-0.8} \cdot 10^{-5}$	
$k_\mathrm{B}T_2$	keV	$5.7^{+10}_{-2.5}$	$9.1^{+2.8}_{-1.4}$	$3.07^{+0.60}_{-0.38}$
η_APEC2	$10^{-14}\,\mathrm{cm}^{-5}$	$1.14^{+0.4}_{-0.25} \cdot 10^{-4}$	$1.46^{+0.10}_{-0.09} \cdot 10^{-4}$	
$f_1^{2-8\,\mathrm{keV}}$	$\mathrm{erg\,cm^{-2}\,s^{-1}\,arcmin^{-2}}$	$0.4^{+0.6}_{-0.4} \cdot 10^{-14}$	$1.143 \cdot 10^{-14}$	
$f_2^{2-8\,\mathrm{keV}}$	$\mathrm{erg\,cm^{-2}\,s^{-1}\,arcmin^{-2}}$	$10^{+5}_{-5} \cdot 10^{-14}$	$12.836 \cdot 10^{-14}$	
$F^{2-8\,\mathrm{keV}}$	$\mathrm{erg\,cm^{-2}\,s^{-1}\,arcmin^{-2}}$	$10^{+5}_{-5} \cdot 10^{-14}$		$13.608 \cdot 10^{-14}$

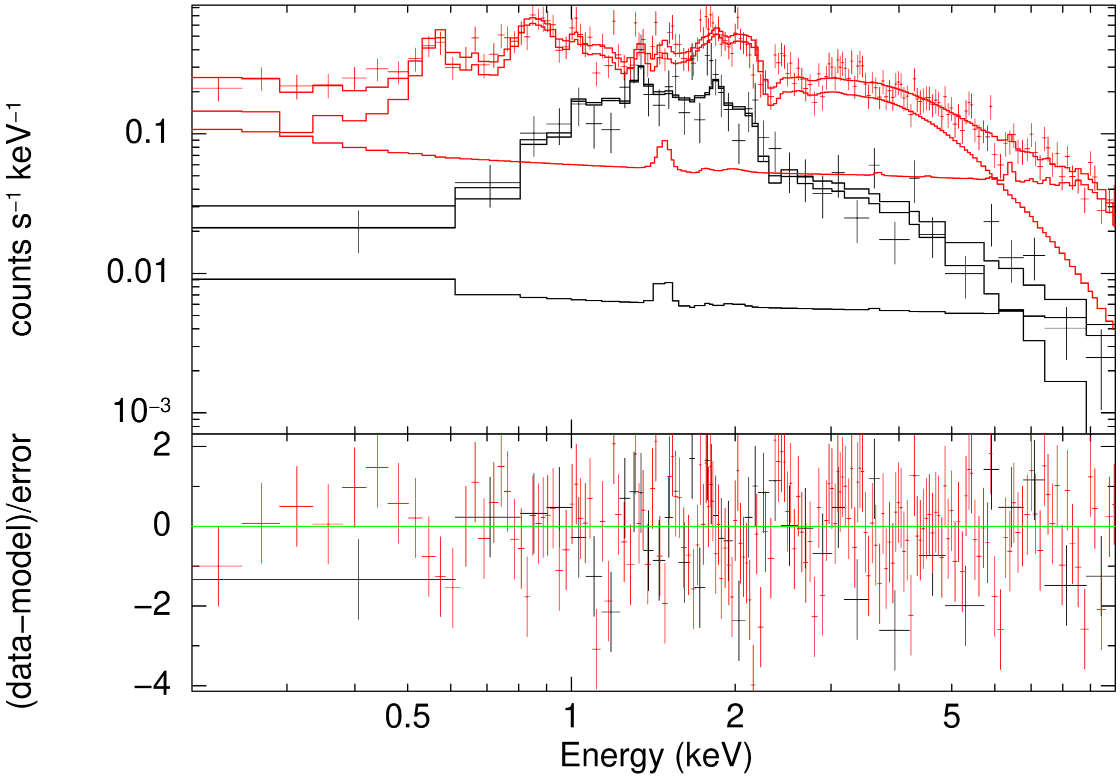

Figure 7.3: *Upper panel:* The 2APEC model fit to the source region of Wd 1 is shown in black while the corresponding background fit is shown in red for comparison. The source data was rebinned to a minimum significance of 3σ and the background data to a minimum significance of 5σ for better visibility. *Lower panel:* Residua of the fits divided by the uncertainty of each data bin.

The column density of the source region $N_\mathrm{H}^\mathrm{2APEC}$ was set to $2.2 \cdot 10^{22}\,\mathrm{cm}^{-2}$ by the fit, which is the maximum value allowed by the HI 4 Pi survey. Further, I found the high metallicity apec component to be cooler with $k_\mathrm{B}T_1 = 0.46^{+0.11}_{-0.13}\,\mathrm{keV}$ and the lower metallicity apec component to be hotter with $k_\mathrm{B}T_2 = 5.7^{+10}_{-2.5}\,\mathrm{keV}$. This is in qualitative agreement with the results in the literature. However, the uncertainty of the hot component's temperature is large, with a lower and upper bound on the 1σ confidence interval of 3.2 keV and 15.7 keV, respectively. Indeed, through varying the $k_\mathrm{B}T_2$ component manually, I found higher temperatures to only have a small impact on the overall quality of the fit.

Table 7.3 also lists the fit parameters of Muno et al. (2006) and Kavanagh et al. (2011) for comparison. In addition, it also gives the de-absorbed fluxes per area of the two apec components between 2 and 8 keV, $f_1^{2-8\,\mathrm{keV}}$ and $f_2^{2-8\,\mathrm{keV}}$, and the sum of these fluxes, $F^{2-8\,\mathrm{keV}}$, for this study and the literature studies where available. I calculated the fluxes with the `Xspec` `cflux` component, resulting in a total source flux from the entire source area of $2.8^{+1.5}_{-1.5} \cdot 10^{-12}\,\mathrm{erg\,cm^{-2}\,s^{-1}}$.

In the case of Muno et al. (2006), parameters are given for four circular analysis regions individually, were the first one is a circle with a radius of 1 arcmin and the other three are annuli with radii between 1 and 2 arcmin, 2 and 3.5 arcmin, and 3.5 and 5 arcmin. Since the source region in this study has a radius of 3 arcmin, I calculated area weighted averages of the three innermost regions of Muno et al. (2006) for $N_{\mathrm{H}}^{2\mathrm{APEC}}$ and the two temperatures and the sums of the parameters in the three innermost regions for the normalizations and fluxes. Further, the corresponding errors were calculated via Gaussian error propagation.

In the case of Kavanagh et al. (2011), the parameters are given for a source region with a radius of 2 arcmin. Therefore, the normalizations and fluxes of Muno et al. (2006) and Kavanagh et al. (2011) were rescaled to a common source area of 1 arcmin^2. The parameters obtained here are consistent with the literature values within their 1σ confidence bounds in all cases except for $k_{\mathrm{B}}T_1$ of Muno et al. (2006), which is hotter than here, η_{APEC1} of Muno et al. (2006), which is smaller than here, and $f_1^{2-8\,\mathrm{keV}}$ of Muno et al. (2006), for which no confidence interval is stated in the respective study. However, the overall agreement between the parameters seems to be good. Therefore, I conclude that the results of this study largely confirm the previous literature results.

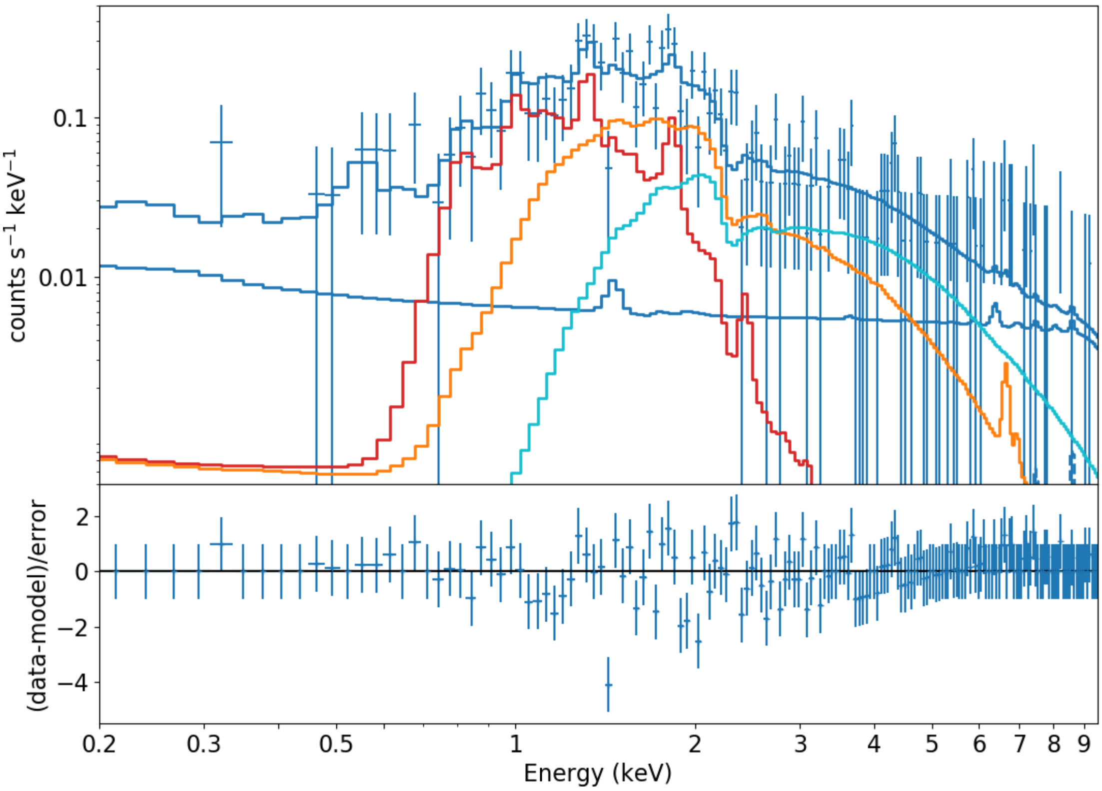

Figure 7.4: Spectrum and 2APEC model fit of the source region. The data is binned to a minimum significance of 5σ per bin. The data, the overall X-ray background model, and the FWC model are given in blue. The cooler apec component is red, the hotter one orange, and the stray light component cyan.

Finally, the source region fit alone can be seen in figure 7.4, where three components of the model are highlighted: the cooler apec component in red, the hotter apec component in orange, and the stray light component in cyan. Other background components, e.g., the LHB and the CGM, are not shown. The overall smoother shape of the hotter `apec` component results from its low metal abundance of $0.62 Z_\odot$. However, one can clearly see a pronounced peak around 6.7 keV, resulting from a helium-like iron emission line. While this line is not visible in the eROSITA spectrum of Wd 1, its detection allowed Kavanagh et al. (2011) to identify the harder source component as thermal.

7.4 APEC+PL Model

The only difference between the 2APEC and the APEC+PL model is that in the latter case the hot low-abundance `apec` component was replaced with a `powerlaw` component. Otherwise, the fits and the comparison to the literature were performed in the same way as above. The free fit parameters of the `powerlaw` component were its spectral index Γ and its normalization η_PL. The fit had a reduced Pearson χ^2 of $\chi^2_\mathrm{P}/\nu = 1754.42/1803$ and a goodness of $P = 0.29$. However, for the goodness calculation I had to freeze both η_APEC and η_PL due to the fit having become insensitive to these parameters.

Table 7.4: Fit parameters of the APEC+PL source model compared to literature values. All normalizations and fluxes were normalized to a source area of 1 arcmin^2. Values from Muno et al. (2006) were recalculated to a single source area as described in the text. The uncertainties give the 1σ confidence intervals of the parameters. If an uncertainty is given without a plus or minus sign, it indicates the upper limit on the parameter allowed by the fit.

Param.	Unit	This study	Muno et al. (2006)	Kavanagh et al. (2011)
$N_\mathrm{H}^\mathrm{CGM}$	10^{22} cm^{-2}	$0.43^{+0.13}_{-0.09}$		
$N_\mathrm{H}^\mathrm{cor}$	10^{22} cm^{-2}	$1.4^{2.2}_{-0.4}$		
N_H^PL	10^{22} cm^{-2}	$2.2^{2.2}_{-0.22}$	$2.40^{+0.16}_{-0.15}$	$2.07^{+0.23}_{-0.26}$
$k_\mathrm{B}T$	keV	$0.43^{+0.13}_{-0.12}$	$0.96^{+0.14}_{-0.08}$	$0.81^{+0.16}_{-0.09}$
η_APEC	10^{-14} cm^{-5}	$1.2^{+1.4}_{-0.6} \cdot 10^{-4}$	$6.2^{+1.1}_{-1.2} \cdot 10^{-5}$	
Γ		$2.1^{+0.5}_{-0.6}$	$2.12^{+0.08}_{-0.09}$	$2.43^{+0.19}_{-0.22}$
η_PL	keV^{-1} cm^{-2} s^{-1}	$4.8^{+1.5}_{-2.0} \cdot 10^{-5}$	$6.5^{+1.0}_{-0.9} \cdot 10^{-4}$	
$f_\mathrm{APEC}^{2-8\,\mathrm{keV}}$	erg cm^{-2} s^{-1} arcmin^{-2}	$0.30^{+0.4}_{-0.19} \cdot 10^{-14}$	$1.247 \cdot 10^{-14}$	
$f_\mathrm{PL}^{2-8\,\mathrm{keV}}$	erg cm^{-2} s^{-1} arcmin^{-2}	$9.0^{+4}_{-2.6} \cdot 10^{-14}$	$13.096 \cdot 10^{-14}$	
$F^{2-8\,\mathrm{keV}}$	erg cm^{-2} s^{-1} arcmin^{-2}	$9^{+5}_{-2.7} \cdot 10^{-14}$		$11.936 \cdot 10^{-14}$

As before, the resulting parameters with their 1σ confidence bounds can be found in table 7.4 together with the corresponding values of Muno et al. (2006) and Kavanagh et al. (2011). The total flux from the source region analyzed here is $2.5^{+1.5}_{-0.8} \cdot 10^{-12}$ erg cm^{-2} s^{-1}. The best fit parameter values are similar to the literature values with overlapping 1σ confidence intervals. The only exception is N_H^PL of Muno et al. (2006), which is relatively large with $2.40 \cdot 10^{22}$ cm^{-2}.

However, the reason for the non-overlap probably lies in the missing upper uncertainty of my corresponding value which ran into its maximum allowed value of $2.2 \cdot 10^{22}\,\mathrm{cm}^{-2}$. Further, the best fit $k_\mathrm{B}T$ is relatively small with 0.43 keV, whereas the literature values are 0.96 keV and 0.81 keV for Muno et al. (2006) and Kavanagh et al. (2011), respectively.

The source data and the APEC+PL fit can be seen in figure 7.5. As for the 2APEC fit, the two source components and the stray light component were highlighted. The `apec` component is shown in red, the `powerlaw` component is shown in orange, and the stray light component is given in cyan. A comparison to figure 7.4 shows that the main function of the `powerlaw` component is to replace the spectral shape of the hotter `apec` component in the 2APEC fit. The main difference is that for the `powerlaw` component, no emission line is visible around 6.7 keV.

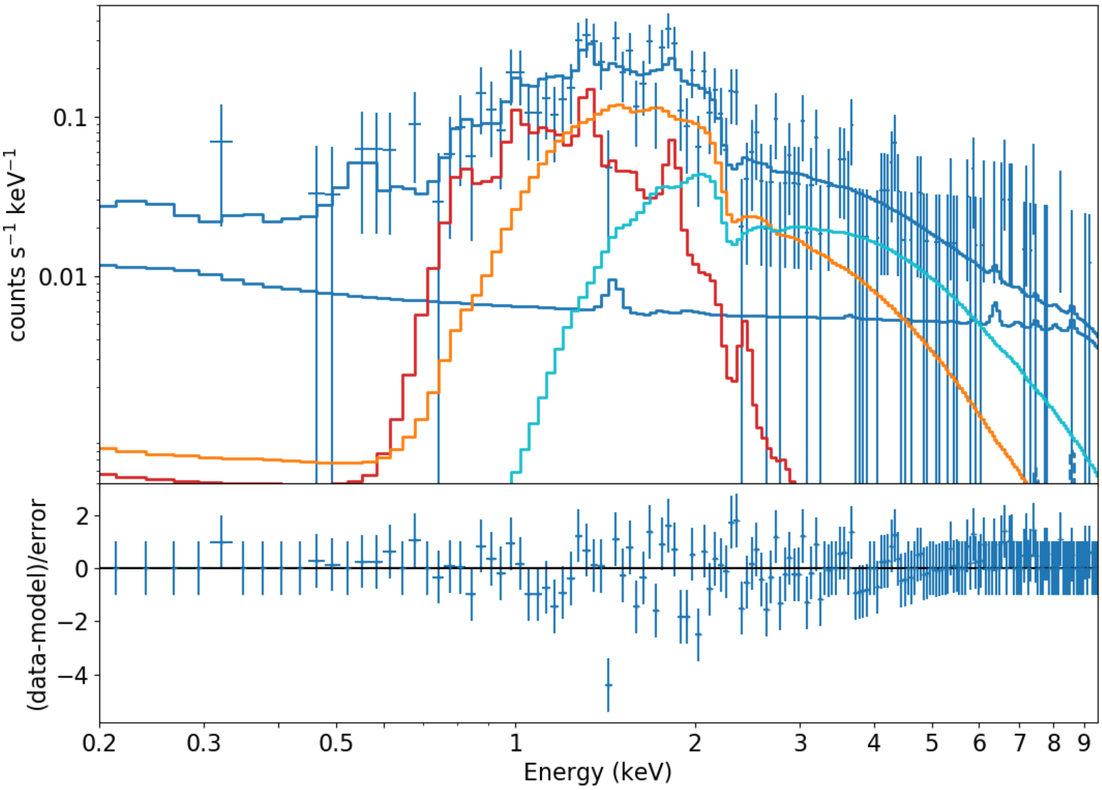

Figure 7.5: Spectrum and APEC+PL model fit of the source region. The data is binned to a minimum significance of 5σ per bin. The data, the overall X-ray background model, and the FWC model are given in blue. The `apec` component is red, the `powerlaw` component orange, and the stray light component cyan.

7.5 Discussion

Judging only from the 2APEC and APEC+PL fits, both models seem to provide an equally good description of the diffuse X-ray emission from Wd 1. In particular, however, this also means that the results presented here do not conflict with the ones of Kavanagh et al. (2011) who detected a 6.7 keV in the central 2 arcmin radius region of the cluster. Indeed, figure 7.4 demonstrates that the eROSITA data is consistent with the presence of such a line at an abundance of $Z_2 = 0.62 Z_\odot$ for the hot plasma, as derived by Kavanagh et al. (2011). Therefore, I conclude that the eROSITA data itself neither corroborates nor refutes one of the two tested models and the preference for a 2APEC model found by Kavanagh et al. (2011) is still valid.

Based on the 2APEC fit, the contribution of different physical sources to the diffuse emission of Wd 1 can now be estimated. Namely, these components are pre-main sequence (PMS) stars, stellar winds, and SNRs. Note that I do not consider nonthermal radiation from accelerated particles as these are disfavoured by the results of Kavanagh et al. (2011).

For discussing potential source components, it is important to estimate the X-ray luminosity of Wd 1. Using $F^{2-8\,\mathrm{keV}}$ from the 2APEC fit, a distance to the cluster of 3.9 kpc, and considering the source area's extent of $\pi(3\,\mathrm{arcmin})^2$, one finds

$$L^{2-8\,\mathrm{keV}} = 5.2^{+2.6}_{-2.6} \cdot 10^{33}\,\mathrm{erg\,s^{-1}}, \tag{7.5.1}$$

using Gaussian error propagation. Further, this results in luminosities $l_1^{2-8\,\mathrm{keV}} = 0.26^{+0.4}_{-0.26} \cdot 10^{33}\,\mathrm{erg\,s^{-1}}$ and $l_2^{2-8\,\mathrm{keV}} = 5.2^{+2.6}_{-2.6} \cdot 10^{33}\,\mathrm{erg\,s^{-1}}$ for the cooler and hotter apec component, respectively.

For comparison, Muno et al. (2006) find $L^{2-8\,\mathrm{keV}} = 3^{+1}_{-1} \cdot 10^{34}\,\mathrm{erg\,s^{-1}}$, however from a larger area with radius 5 arcmin and assuming a distance of $d = 5\,\mathrm{kpc}$. On the other hand, Kavanagh et al. (2011) find $L^{2-8\,\mathrm{keV}} = 1.7 \cdot 10^{33}\,\mathrm{erg\,s^{-1}}$, using a region with area 2 arcmin and $d = 3.5\,\mathrm{kpc}$. As a further note, be aware that while these authors masked many point sources inside Wd 1 before extracting the diffuse emission spectrum, only the magnetar CXOU 164710.2−455216 was masked for the analysis presented here.

7.5.1 Pre-Main Sequence Stars

Apart from high mass stars, Clark et al. (2005) also detected a population of PMS stars in Wd 1. PMS stars can emit X-ray radiation through magnetic reconnection events which heat the surrounding medium to high temperatures. These authors found 45 candidates for such stars down to a limiting luminosity of $\approx 3 \cdot 10^{31}\,\mathrm{erg\,s^{-1}}$ at $d = 5\,\mathrm{kpc}$, corresponding to $\approx 1.8 \cdot 10^{31}\,\mathrm{erg\,s^{-1}}$ at $d = 3.9\,\mathrm{kpc}$, as adopted for this work. By comparison with the Orion Nebular Cluster, Clark et al. (2005) estimate a PMS population of at least 32000 in Wd 1.

Similarly, Kavanagh et al. (2011) estimate the contribution of PMS stars to the diffuse X-ray flux in Wd 1. I adopt their analysis and slightly modify it to account for the differences in my treatment of the data. The comparison is based on data from the Chandra Orion Ultradeep Project (Getman et al., 2005), which identified point sources in the Orion Nebular Complex. Importantly, it identified a larger part of the PMS population than is known for Wd 1. Kavanagh et al. (2011) rescaled the $0.5 - 8\,\mathrm{keV}$ flux distribution of PMS sources in the Orion cluster using the age, absorbing column density, and distance of Wd 1.

From this flux distribution, they estimated the luminosity of unresolved PMS stars in Wd 1 to be $\approx 1.3 \cdot 10^{33}\,\mathrm{erg\,s^{-1}}$ between 2 and 8 keV. However, no PMS sources were masked for this thesis due to none of them being resolved by eROSITA. Therefore, the luminosities of PMS stars masked by Kavanagh et al. (2011) have to be added to their estimated value, resulting in $\approx 1.65 \cdot 10^{33}\,\mathrm{erg\,s^{-1}}$. The masked sources are listed in table 1 of their study.

Kavanagh et al. (2011) assume $d = 3.55\,\mathrm{kpc}$, while $d = 3.9\,\mathrm{kpc}$ is used for this thesis. Rescaling the estimated flux accordingly results in an estimated luminosity of $L_{\mathrm{PMS}}^{2-8\,\mathrm{keV}} \approx 2 \cdot 10^{33}\,\mathrm{erg\,s^{-1}}$ from PMS stars. Consequently, PMS stars might be able to explain up to 40% of the diffuse X-ray flux from Wd 1 as seen by eROSITA.

This is more than two times as large as the 15% estimated by Kavanagh et al. (2011). The main differences in the analysis are the smaller flux inferred by my fit as compared to their fit, as can be seen in table 7.3, the addition of PMS sources masked by these authors to the estimate presented here, as well as the different source areas. Specifically, Kavanagh et al. (2011) assume most PMS stars to reside within 3 arcmin of the cluster center, as demonstrated in figure 3 of Clark et al. (2005). Accordingly, they rescaled the estimated PMS luminosity to their analysis region with a radius of 2 arcmin. Since my analysis region already has a radius of 3 arcmin, no such rescaling was performed.

7.5.2 Stellar Winds

Wd 1 contains a rich population of massive stars, in particular 24 WR stars, which are expected to posses strong stellar winds. In the relatively densely packed cluster, these winds should collide and thermalize, producing a hot X-ray emitting plasma.

I follow Muno et al. (2006) and Kavanagh et al. (2011) in estimating the properties of the thermalized cluster wind plasma via the analytic cluster wind model of Cantó et al. (2000). Assuming the supersonic solution and a gas with an adiabatic index of 5/3, as appropriate for monoatomic hydrogen, the density n and the temperature $k_{\mathrm{B}}T$ of the thermalized cluster wind are

$$n = 0.19N \left(\frac{\dot{M}}{10^{-5} M_{\odot}\mathrm{yr}^{-1}}\right) \left(\frac{v_{\mathrm{w}}}{1000\,\mathrm{km\,s^{-1}}}\right)^{-1} \left(\frac{R_{\mathrm{c}}}{1\,\mathrm{pc}}\right)^{-2} \mathrm{cm}^{-3} \tag{7.5.2}$$

and

$$k_{\mathrm{B}}T = 1.3 \left(\frac{v_{\mathrm{w}}}{1000\,\mathrm{km\,s^{-1}}}\right)^{2} \mathrm{keV}, \tag{7.5.3}$$

where N is the number of WR stars, $\dot{M}$ is their mean mass loss rate, v_{w} is their mean wind speed, and R_{c} is the cluster radius, assuming a spherical shape.

Employing $N = 24$ (Clark et al., 2020), $\dot{M} = 1.4 \cdot 10^{-5} M_{\odot}\mathrm{yr}^{-1}$, $v_{\mathrm{w}} = 1320\,\mathrm{km\,s^{-1}}$, as estimated by Kavanagh et al. (2011), and $R_{\mathrm{c}} = 3.4\,\mathrm{pc}$, corresponding to 3 arcmin at $d = 3.9\,\mathrm{kpc}$, one finds $n = 0.4\,\mathrm{cm}^{-3}$ and $k_{\mathrm{B}}T = 2.3\,\mathrm{keV}$. Comparing this temperature with the best fit temperature of the hot apec component in table 7.3, I find the predicted value to lie somewhat lower than the 1σ bound of the fitted one.

The predicted value n can now be used to calculate an emission measure via

$$K_{\mathrm{EM}} = \frac{4}{3}\pi R_{\mathrm{c}}^{3} n^{2}, \tag{7.5.4}$$

which yields K_{EM} $=7.8 \cdot 10^{56}\,\mathrm{cm}^{-3}$. At a distance of 3.9 kpc, this corresponds to an apec normalization of

$$\eta_{\mathrm{APEC}} = \frac{10^{-14}}{4\pi d^2} K_{\mathrm{EM}} = 0.004\,\mathrm{cm}^{-5}. \tag{7.5.5}$$

Using this normalization and the derived temperature, I defined an apec model in `Xspec` and calculated its flux between 2 and 8 keV via the `flux` command. The result is $F^{2-8\,\mathrm{keV}} = 2.0 \cdot 10^{-12}\,\mathrm{erg\,cm^{-2}\,s^{-1}}$, corresponding to $L^{2-8\,\mathrm{keV}} = 3.7 \cdot 10^{33}\,\mathrm{erg\,s^{-1}}$. This is about 70% of the best fit value for the diffuse X-ray luminosity of Wd 1. However, keep in mind the large uncertainty on the luminosity which has a 1σ lower bound of $1.6 \cdot 10^{33}\,\mathrm{erg\,s^{-1}}$. Therefore, either PMS stars or thermalized stellar winds can explain the bulk of the X-ray luminosity from Wd 1 as observed with eROSITA.

Still, it is important to keep in mind that the estimate presented here depends sensitively on the assumed properties of the stars driving the winds. For example, using $\dot{M} = 6 \cdot 10^{-5} M_{\odot}\mathrm{yr}^{-1}$ and $v_{\mathrm{w}} = 1700\,\mathrm{km\,s^{-1}}$, as done by Muno et al. (2006) based on Leitherer et al. (1992), results in $n = 1.4\,\mathrm{cm}^{-3}$. Since the apec normalization depends quadratically on this density, one obtains a luminosity about a factor 15 larger, everything else being equal. This demonstrates the relatively large leeway provided by such an estimate.

7.5.3 Supernova Remnants

The magnetar CXOU 164710.2−455216 is the only direct piece of evidence for past supernova activity in Wd 1. However, given the cluster's age and high-mass stellar population, it is reasonable to assume that numerous supernovae should already have happened there. In principle, the resulting SNRs could then contribute to the diffuse X-ray flux in Wd 1.

Based on an extrapolation of an initial mass function with a slope between 1.8 and 2.7, Muno et al. (2006) estimate that Wd 1 should initially have contained more than 50 stars with masses above $50 M_{\odot}$. These should already have exploded as supernovae, resulting in an average rate of about 1 supernova every 7000 − 13 000 yr. With a standard supernova explosion energy of 10^{51} erg, this results in a released power between 2.5 and $4.5 \cdot 10^{39}\,\mathrm{erg\,s^{-1}}$. In principle, only a negligible fraction of this would be necessary to explain the observed diffuse X-ray luminosity.

Still, several reasons speak against SNRs as the dominant source of the diffuse X-ray emission from Wd 1. First of all, no SNRs are detected in the cluster, indicating that if they are present, they do not strongly interact with the surrounding ISM to produce X-ray emission. Indeed, stellar winds from Wd 1 might have cleared away the surrounding ISM, therefore preventing such an interaction. Second, while SNRs can in principle also emit X-rays through interactions with stellar winds, the resulting emission is not expected to be as hard as for the dominant hot component observed in Wd 1 (Kavanagh et al., 2011). Finally, SNR ejecta travelling with $1000\,\mathrm{km\,s^{-1}}$ would leave the cluster after $\sim$ 1000 yr. Combined with the estimated supernova rate above, this indicates that Wd 1 should be devoid of SNRs for most of the time, rendering it unlikely that they are responsible for the currently observed diffuse X-ray emission.

CHAPTER 8

Summary

> Everybody's a mad scientist, and life is their lab. We're all trying to experiment to find a way to live, to solve problems, to fend off madness and chaos.
>
> David Cronenberg

This Master's thesis aims at adding to the understanding of the origin of the highest energy CRs. Only recently, this research field was profoundly impacted by the discovery of a Galactic population of PeVatron sources which casts into doubt the long-held standard paradigm of particle acceleration up to PeV energies in isolated SNRs. In particular, the association of PeVatron candidates with sources such as PWNe and young stellar clusters reinvigorated the interest in these objects as alternative sources of accelerated particles, potentially paving the way to a better model of CR production and transport in the Milky Way.

However, any such model of CR production has to account for the fact that the bulk of CRs is hadronic in nature. For any individual PeVatron candidate, identified via its γ-ray emission, this opens up the question whether this emission is better explained via a leptonic or hadronic particle population. This is exactly where this study comes in. In particular, it is aimed at the search for X-ray synchrotron radiation from J1646−458, the PeVatron candidate associated with the massive young star cluster Wd 1. As synchrotron radiation from hadrons is strongly suppressed, its detection would indicate the presence of an accelerated electron population. For this analysis, I used data from eRASS:4 provided by eROSITA, since its all-sky survey nature is particularly well suited for studying the large angular extent of J1646−458.

The main obstacle in this analysis was the strong contamination of the source area around Wd 1 with stray light from the nearby LMXB GX 340+0. Therefore, it was not easily possible to spectrally model the source regions. Instead, I compared the source regions to test regions of comparable stray light contamination. Visual inspections of images of the source region and of the spectra of the source and test regions did not reveal any clear evidence for an additional source component in the source regions. More importantly, fits of Gaussian distributions to the difference residua of the source spectra minus the test spectra consistently resulted in negative mean values.

Crucially, this finding was confirmed by one-sample two-sided t-tests. Based on these, the null hypothesis of an equal or larger number of counts in source and test regions had to be rejected in favor of the alternative of more counts in the test regions with a significance $\gtrsim 3\sigma$, depending on the specific regions which were compared. Following this finding, the main conclusion of this thesis is that no evidence for synchrotron radiation around Wd 1 is present in the eROSITA data. The higher count number in the test regions could be explained by their slightly smaller absorbing column densities or their slightly larger exposure times.

Based on the non-detection of an additional source component, I fitted the source regions with pure background models based on Ponti et al. (2023). One of the main factors of uncertainty in these fits was the treatment of the stray light contamination from GX 340+0, which was modelled with a phenomenological absorbed `diskbb` component.

The resulting fits provide reasonable descriptions of the data with goodness values between 0.49 and 0.90. However, different from Ponti et al. (2023), I had to assume absorbing column densities for the CGM and Galactic corona smaller than the HI 4 Pi survey values. In addition, the normalization of the Galactic corona component in the fits presented here is orders of magnitude larger than for these authors. A possible explanation is the difference in the source regions, which lie on the Galactic plane for this study, while they are removed from the Galactic plane for Ponti et al. (2023). This might well lead to a larger contribution from hot gas and possibly unresolved M dwarf stars in the Galactic disk.

Next, based on the background fits, an upper limit on the synchrotron flux from the region of J1646−458 of $\eta_X \lesssim 1.00 \cdot 10^6\,\mathrm{TeV}^{-1}\,\mathrm{cm}^{-2}\,\mathrm{s}^{-1}$ was derived. Adding this upper limit to a leptonic SED fit based on γ-ray data from Aharonian et al. (2022) resulted in an upper limit on the magnetic field strength of $B \lesssim 2\,\mu\mathrm{G}$. This value is somewhat more restrictive than, though consistent with a previous estimate from Härer et al. (2023), namely $0.7\,\mu\mathrm{G} \lesssim B \lesssim 4.5\,\mu\mathrm{G}$. Therefore, I conclude that both the leptonic emission scenario, where particles would be accelerated at Wd 1's cluster wind termination shock, as well as the hadronic emission scenario, where they would be accelerated inside the cluster itself, are still viable. However, one should keep in mind that the hadronic scenario suffers from a lack of correlation between γ-ray emission and the density of gas which is necessary for providing sufficient target material for pion production.

Further, it is worth mentioning that an upper limit on the HE γ-ray flux derived by Ohm et al. (2013) seems to be violated by the aforementioned leptonic SED fit. Possible explanations are a wrong estimation of the source size used for deriving the HE upper limit, the model dependence of this limit, or a potential hadronic contribution to the emission which would alleviate the discrepancy.

Finally, I also extracted the diffuse X-ray emission spectrum of the star cluster Wd 1 itself. After estimating the background to this emission with a spectral fit to a suitable background region, I modelled the diffuse emission with a two-component `apec` model (2APEC) and an `apec` model with an additional nonthermal `powerlaw` component (APEC+PL). In line with previous studies (Kavanagh et al., 2011; Muno et al., 2006), both models can explain the data equally well. In particular, the eROSITA data seems to be insufficient to confirm or refute the presence of a

6.7 keV iron emission line reported by Kavanagh et al. (2011), which would indicate a preference for the 2APEC model. Therefore, the preference for the purely thermal model established by these authors seems to remain intact.

Regarding the origin of the diffuse X-ray emission, I find that its flux of $F^{2-8\text{ keV}} = 2.8^{+1.5}_{-1.5} \cdot 10^{-12}\,\mathrm{erg\,cm^{-2}\,s^{-1}}$ can be explained by colliding stellar winds inside the cluster with a potential contribution up to around 40% from unresolved PMS stars. However, the estimate for the stellar winds is very sensitive to the assumed wind parameters, where small differences can lead to order of magnitude differences in the predicted luminosity. Further, the estimate for the PMS stars differs from the one of Kavanagh et al. (2011), who find a maximum contribution from these objects of 15%. The main difference between this thesis and their analysis is their larger inferred diffuse flux, the masking of PMS stars resolved in their data, and their smaller analysis region.

Finally, while SNRs could in principle provide sufficient energy to explain the diffuse X-ray flux, none of them is detected with Wd 1. Even more, based on the estimated supernova rate in the cluster and a typical SNR expansion velocity, they are expected to be absent from the star cluster for prolonged time periods.

Bibliography

Aab, A., Abreu, P., Aglietta, M., Albury, J. M., Allekotte, I., Almela, A., Alvarez Castillo, J., Alvarez-Muñiz, J., Alves Batista, R., Anastasi, G. A., Anchordoqui, L., Andrada, B., Andringa, S., Aramo, C., Araújo Ferreira, P. R., Asorey, H., Assis, P., Avila, G., Badescu, A. M., … Pierre Auger Collaboration. (2020). Measurement of the cosmic-ray energy spectrum above 2.5 $\times 10^{18}$ eV using the Pierre Auger Observatory. *Physical Review D*, *102*(6), 062005.

Aartsen, M. G., Abraham, K., Ackermann, M., Adams, J., Aguilar, J. A., Ahlers, M., Ahrens, M., Altmann, D., Anderson, T., Archinger, M., Arguelles, C., Arlen, T. C., Auffenberg, J., Bai, X., Barwick, S. W., Baum, V., Bay, R., Beatty, J. J., Becker Tjus, J., … IceCube Collaboration. (2015). A Combined Maximum-likelihood Analysis of the High-energy Astrophysical Neutrino Flux Measured with IceCube. *ApJ*, *809*(1), 98.

Abeysekara, A. U., Albert, A., Alfaro, R., Angeles Camacho, J. R., Arteaga-Velázquez, J. C., Arunbabu, K. P., Avila Rojas, D., Ayala Solares, H. A., Baghmanyan, V., Belmont-Moreno, E., BenZvi, S. Y., Brisbois, C., Caballero-Mora, K. S., Capistrán, T., Carramiñana, A., Casanova, S., Cotti, U., Cotzomi, J., Coutiño de León, S., … HAWC Collaboration. (2020). Multiple Galactic Sources with Emission Above 56 TeV Detected by HAWC. *Physical Review Letters*, *124*(2), 021102.

Abramowski, A., Acero, F., Aharonian, F., Akhperjanian, A. G., Anton, G., Balzer, A., Barnacka, A., Barres de Almeida, U., Becherini, Y., Becker, J., Behera, B., Bernlöhr, K., Birsin, E., Biteau, J., Bochow, A., Boisson, C., Bolmont, J., Bordas, P., Brucker, J., … Zechlin, H. .-. (2012). Discovery of extended VHE γ-ray emission from the vicinity of the young massive stellar cluster Westerlund 1. *AAP*, *537*, A114.

Ackermann, M., Ajello, M., Allafort, A., Baldini, L., Ballet, J., Barbiellini, G., Bastieri, D., Belfiore, A., Bellazzini, R., Berenji, B., Blandford, R. D., Bloom, E. D., Bonamente, E., Borgland, A. W., Bottacini, E., Brigida, M., Bruel, P., Buehler, R., Buson, S., … Bontemps, S. (2011). A Cocoon of Freshly Accelerated Cosmic Rays Detected by Fermi in the Cygnus Superbubble. *Science*, *334*(6059), 1103.

Ackermann, M., Ajello, M., Albert, A., Atwood, W. B., Baldini, L., Ballet, J., Barbiellini, G., Bastieri, D., Bechtol, K., Bellazzini, R., Bissaldi, E., Blandford, R. D., Bloom, E. D., Bottacini, E., Brandt, T. J., Bregeon, J., Bruel, P., Buehler, R., Buson, S., … Zimmer, S. (2015). The Spectrum of Isotropic Diffuse Gamma-Ray Emission between 100 MeV and 820 GeV. *ApJ*, *799*(1), 86.

Adriani, O., Barbarino, G. C., Bazilevskaya, G. A., Bellotti, R., Boezio, M., Bogomolov, E. A., Bonechi, L., Bongi, M., Bonvicini, V., Borisov, S., Bottai, S., Bruno, A., Cafagna, F., Campana, D., Carbone, R., Carlson, P., Casolino, M., Castellini, G., Consiglio, L., … Zverev, V. G. (2011). PAMELA Measurements of Cosmic-Ray Proton and Helium Spectra. *Science*, *332*(6025), 69.

Aharonian, F., Ashkar, H., Backes, M., Barbosa Martins, V., Becherini, Y., Berge, D., Bi, B., Böttcher, M., de Bony de Lavergne, M., Bradascio, F., Brose, R., Brun, F., Bulik, T., Burger-Scheidlin, C., Cangemi, F., Caroff, S., Casanova, S., Cerruti, M., Chand, T., … Wong, G. (2022). A deep spectromorphological study of the γ-ray emission surrounding the young massive stellar cluster Westerlund 1. *AAP*, *666*, A124.

Aharonian, F. A., Atoyan, A. M., & Kifune, T. (1997). Inverse Compton gamma radiation of faint synchrotron X-ray nebulae around pulsars. *MNRAS*, *291*(1), 162–176.

Aharonian, F. A., Kelner, S. R., & Prosekin, A. Y. (2010). Angular, spectral, and time distributions of highest energy protons and associated secondary gamma rays and neutrinos propagating through extragalactic magnetic and radiation fields. *Physical Review D*, *82*(4), 043002.

Aharonian, F., Yang, R., & de Oña Wilhelmi, E. (2019). Massive stars as major factories of Galactic cosmic rays. *Nature Astronomy*, *3*, 561–567.

Aharonian, F. A. (2004). *Very High Energy Cosmic Gamma Radiation: A Crucial Window on the Extreme Universe*. World Scientific Publishing.

Amenomori, M., Bao, Y. W., Bi, X. J., Chen, D., Chen, T. L., Chen, W. Y., Chen, X., Chen, Y., Cirennima, Cui, S. W., Danzengluobu, Ding, L. K., Fang, J. H., Fang, K., Feng, C. F., Feng, Z., Feng, Z. Y., Gao, Q., Gou, Q. B., … Tibet AS γ Collaboration. (2019). First Detection of Photons with Energy beyond 100 TeV from an Astrophysical Source. *Physical Review Letters*, *123*(5), 051101.

Baade, W., & Zwicky, F. (1934). Cosmic Rays from Super-novae. *Proceedings of the National Academy of Science*, *20*(5), 259–263.

Ballet, J. (2006). X-ray synchrotron emission from supernova remnants. *Advances in Space Research*, *37*(10), 1902–1908.

Bartelmann, M. (2013). *Theoretical Astrophysics: An Introduction*. WILEY-VCH Verlag.

Beasor, E. R., Davies, B., Smith, N., Gehrz, R. D., & Figer, D. F. (2021). The Age of Westerlund 1 Revisited. *ApJ*, *912*(1), 16.

Beasor, E. R., Smith, N., & Andrews, J. E. (2023). Don't Believe the Hype(r): The Yellow Supergiants of Westerlund 1. *ApJ*, *952*(2), 113.

Bell, A. R., Schure, K. M., Reville, B., & Giacinti, G. (2013). Cosmic-ray acceleration and escape from supernova remnants. *MNRAS*, *431*(1), 415–429.

Bethe, H., & Heitler, W. (1934). On the stopping of fast particles and on the creation of positive electrons. *Proceedings of the Royal Society*, *A14683*(112), 147–163.

Bhadra, S., Gupta, S., Nath, B. B., & Sharma, P. (2022). Cosmic rays from massive star clusters: a close look at Westerlund 1. *MNRAS*, *510*(4), 5579–5591.

Blumenthal, G. R., & Gould, R. J. (1970). Bremsstrahlung, Synchrotron Radiation, and Compton Scattering of High-Energy Electrons Traversing Dilute Gases. *Reviews of Modern Physics*, *42*(2), 237–271.

Boulares, A., & Cox, D. P. (1990). Galactic Hydrostatic Equilibrium with Magnetic Tension and Cosmic-Ray Diffusion. *ApJ*, *365*, 544.

Brandner, W., Clark, J. S., Stolte, A., Waters, R., Negueruela, I., & Goodwin, S. P. (2008). Intermediate to low-mass stellar content of Westerlund 1. *AAP*, *478*(1), 137–149.

Brose, R., Sushch, I., & Mackey, J. (2022). Core-collapse supernovae in dense environments - particle acceleration and non-thermal emission. *MNRAS*, *516*(1), 492–505.

Bykov, A. M., Gladilin, P. E., & Osipov, S. M. (2013). Non-linear model of particle acceleration at colliding shock flows. *MNRAS*, *429*(3), 2755–2762.

Cantó, J., Raga, A. C., & Rodríguez, L. F. (2000). The Hot, Diffuse Gas in a Dense Cluster of Massive Stars. *ApJ*, *536*(2), 896–901.

Cao, Z., Aharonian, F. A., An, Q., Axikegu, L. X., Bai, Bai, Y. X., Bao, Y. W., Bastieri, D., Bi, X. J., Bi, Y. J., Cai, H., Cai, J. T., Cao, Z., Chang, J., Chang, J. F., Chang, X. C., Chen, B. M., Chen, J., Chen, L., Chen, L., … Zuo, X. (2021). Ultrahigh-energy photons up to 1.4 petaelectronvolts from 12 γ-ray Galactic sources. *Nature*, *594*(7861), 33–36.

Cardillo, M., & Giuliani, A. (2023). The LHAASO PeVatron bright sky: what we learned. *Applied Sciences*, *13*(11), 6433.

Carroll, B. W., & Ostlie, D. A. (2014). *An introduction to modern astrophysics* (2nd ed.). Pearson.

Cash, W. (1979). Parameter estimation in astronomy through application of the likelihood ratio. *ApJ*, *228*, 939–947.

Casse, M., & Paul, J. A. (1980). Local gamma rays and cosmic-ray acceleration by supersonic stellar winds. *ApJ*, *237*, 236–243.

Clark, J. S., Negueruela, I., Crowther, P. A., & Goodwin, S. P. (2005). On the massive stellar population of the super star cluster Westerlund 1. *AAP*, *434*(3), 949–969.

Clark, J. S., Muno, M. P., Negueruela, I., Dougherty, S. M., Crowther, P. A., Goodwin, S. P., & de Grijs, R. (2008). Unveiling the X-ray point source population of the Young Massive Cluster Westerlund 1. *AAP*, *477*(1), 147–163.

Clark, J. S., Ritchie, B. W., & Negueruela, I. (2020). A VLT/FLAMES survey for massive binaries in Westerlund 1. VII. Cluster census. *AAP*, *635*, A187.

Cristofari, P. (2021). The Hunt for Pevatrons: The Case of Supernova Remnants. *Universe*, *7*(9), 324.

Cristofari, P., Blasi, P., & Amato, E. (2020). The low rate of Galactic pevatrons. *Astroparticle Physics*, *123*, 102492.

Crowther, P. A., Hadfield, L. J., Clark, J. S., Negueruela, I., & Vacca, W. D. (2006). A census of the Wolf–Rayet content in Westerlund 1 from near-infrared imaging and spectroscopy*. *MNRAS*, *372*(3), 1407–1424.

Dashyan, G., & Dubois, Y. (2020). Cosmic ray feedback from supernovae in dwarf galaxies. *AAP*, *638*, A123.

Davis, J. E. (2001). The Formal Underpinnings of the Response Functions Used in X-Ray Spectral Analysis. *ApJ*, *548*(2), 1010–1019.

Dickey, J. M., & Lockman, F. J. (1990). H I in the galaxy. *ARAA*, *28*, 215–261.

Draine, B. T. (2010). *Physics of the Interstellar and Intergalactic Medium (Princeton Series in Astrophysics)*. Princeton University Press.

Drury, L. O. (1983). Review Article: An introduction to the theory of diffusive shock acceleration of energetic particles in tenuous plasmas. *Reports on Progress in Physics*, *46*(8), 973–1027.

Foreman-Mackey, D., Hogg, D. W., Lang, D., & Goodman, J. (2013). emcee: The MCMC Hammer. *Publications of the Astronomical Society of the Pacific*, *125*(925), 306.

Freyberg, M., Perinati, E., Pacaud, F., Eraerds, T., Churazov, E., Dennerl, K., Predehl, P., Merloni, A., Meidinger, N., Bulbul, E., Friedrich, S., Gilfanov, M., Tenzer, C., Pommranz, C., Eckert, D., Schmitt, J., Brusa, M., & Santangelo, A. (2020). SRG/eROSITA in-flight background at L2. In J.-W. A. den Herder, S. Nikzad, & K. Nakazawa (Eds.), *Space telescopes and instrumentation 2020: Ultraviolet to gamma ray* (114441O).

Gabici, S., Evoli, C., Gaggero, D., Lipari, P., Mertsch, P., Orlando, E., Strong, A., & Vittino, A. (2019). The origin of Galactic cosmic rays: Challenges to the standard paradigm. *International Journal of Modern Physics D*, *28*(15), 1930022–339.

Getman, K. V., Flaccomio, E., Broos, P. S., Grosso, N., Tsujimoto, M., Townsley, L., Garmire, G. P., Kastner, J., Li, J., Harnden, J., F. R., Wolk, S., Murray, S. S., Lada, C. J., Muench, A. A., McCaughrean, M. J., Meeus, G., Damiani, F., Micela, G., Sciortino, S., … Feigelson, E. D. (2005). Chandra Orion Ultradeep Project: Observations and Source Lists. *ApJS*, *160*(2), 319–352.

Gupta, S., Nath, B. B., Sharma, P., & Eichler, D. (2020). Realistic modelling of wind and supernovae shocks in star clusters: addressing 22Ne/20Ne and other problems in Galactic cosmic rays. *MNRAS*, *493*(3), 3159–3177.

H. E. S. S. Collaboration, Abramowski, A., Aharonian, F., Ait Benkhali, F., Akhperjanian, A. G., Angüner, E. O., Backes, M., Balenderan, S., Balzer, A., Barnacka, A., Becherini, Y., Becker-Tjus, J., Berge, D., Bernhard, S., Bernlöhr, K., Birsin, E., Biteau, J., Böttcher, M., Boisson, C., … Zechlin, H. .-. (2015). The exceptionally powerful TeV γ-ray emitters in the Large Magellanic Cloud. *Science*, *347*(6220), 406–412.

Härer, L. K., Reville, B., Hinton, J., Mohrmann, L., & Vieu, T. (2023). Understanding the TeV γ-ray emission surrounding the young massive star cluster Westerlund 1. *AAP*, *671*, A4.

HAWC Collaboration, Abeysekara, A. U., Albert, A., Alfaro, R., Alvarez, C., Álvarez, J. D., Arceo, R., Arteaga-Velázquez, J. C., Avila Rojas, D., Ayala Solares, H. A., Belmont-Moreno, E., BenZvi, S. Y., Brisbois, C., Caballero-Mora, K. S., Capistrán, T., Carramiñana, A., Casanova, S., Castillo, M., Cotti, U., … Zhou, H. (2018). Very high energy particle acceleration powered by the jets of the microquasar SS 433. *arXiv e-prints*, arXiv:1810.01892.

Hess, V. F. (1912). Über Beobachtungen der durchdringenden Strahlung bei sieben Freiballonfahrten. *Phys. Z.*, *13*, 1084–1091.

HESS Collaboration, Abramowski, A., Aharonian, F., Benkhali, F. A., Akhperjanian, A. G., Angüner, E. O., Backes, M., Balzer, A., Becherini, Y., Tjus, J. B., Berge, D., Bernhard, S., Bernlöhr, K., Birsin, E., Blackwell, R., Böttcher, M., Boisson, C., Bolmont, J., Bordas, P., … Żywucka, N. (2016). Acceleration of petaelectronvolt protons in the Galactic Centre. *Nature*, *531*(7595), 476–479.

Hillas, A. M. (1984). The Origin of Ultra-High-Energy Cosmic Rays. *ARA&A*, *22*, 425–444.

Hillas, A. M. (2005). TOPICAL REVIEW: Can diffusive shock acceleration in supernova remnants account for high-energy galactic cosmic rays? *Journal of Physics G Nuclear Physics*, *31*(5), R95–R131.

IceCube Collaboration, Abbasi, R., Ackermann, M., Adams, J., Aguilar, J. A., Ahlers, M., Ahrens, M., Alameddine, J. M., Alves, A. A., Amin, N. M., Andeen, K., Anderson, T., Anton, G., Argüelles, C., Ashida, Y., Athanasiadou, S., Axani, S., Bai, X., V., A. B., ... Zhelnin, P. (2023). Observation of high-energy neutrinos from the galactic plane. *Science*, *380*(6652), 1338–1343.

Ipavich, F. M. (1975). Galactic winds driven by cosmic rays. *ApJ*, *196*, 107–120.

Kavanagh, P. J., Norci, L., & Meurs, E. J. A. (2011). Diffuse thermal X-ray emission in the core of the young massive cluster Westerlund 1. *NA*, *16*(7), 461–469.

Kavanagh, P. J., Vink, J., Sasaki, M., Chu, Y.-H., Filipović, M. D., Ohm, S., Haberl, F., Manojlovic, P., & Maggi, P. (2019). Magnetic field estimates from the X-ray synchrotron emitting rims of the 30 Dor C superbubble and the implications for the nature of 30 Dor C's TeV emission. *AAP*, *621*, A138.

Kelner, S. R., Aharonian, F. A., & Bugayov, V. V. (2006). Energy spectra of gamma rays, electrons, and neutrinos produced at proton-proton interactions in the very high energy regime. *Physical Review D*, *74*(3), 034018.

Khangulyan, D., Aharonian, F. A., & Kelner, S. R. (2014). Simple Analytical Approximations for Treatment of Inverse Compton Scattering of Relativistic Electrons in the Blackbody Radiation Field. *ApJ*, *783*(2), 100.

Klein, U., Lisenfeld, U., & Verley, S. (2018). Radio synchrotron spectra of star-forming galaxies. *AAP*, *611*, A55.

Kothes, R., & Dougherty, S. M. (2007). The distance and neutral environment of the massive stellar cluster Westerlund 1. *AAP*, *468*(3), 993–1000.

Kroupa, P. (2002). The Initial Mass Function of Stars: Evidence for Uniformity in Variable Systems. *Science*, *295*(5552), 82–91.

Lagage, P. O., & Cesarsky, C. J. (1983). The maximum energy of cosmic rays accelerated by supernova shocks. *AAP*, *125*, 249–257.

Lavagetto, G., Iaria, R., di Salvo, T., Burderi, L., Robba, N. R., Frontera, F., & Stella, L. (2004). A BeppoSAX study of the Galactic Z-source GX 340+0. *Nuclear Physics B Proceedings Supplements*, *132*, 616–619.

Leitherer, C., Robert, C., & Drissen, L. (1992). Deposition of Mass, Momentum, and Energy by Massive Stars into the Interstellar Medium. *ApJ*, *401*, 596.

Lenok, V. (2022). *Measurement of the Cosmic-ray Energy Spectrum Using a Novel Approach to Model the Aperture of Radio Arrays* (PhD Thesis). Karlsruher Institut für Technologie. Retrieved July 29, 2022, from https://www.iap.kit.edu/tunka-rex/downloads/10.5445IR1000143479.pdf

LHAASO Collaboration, Cao, Z., Aharonian, F., An, Q., Axikegu, Bai, L. X., Bai, Y. X., Bao, Y. W., Bastieri, D., Bi, X. J., Bi, Y. J., Cai, H., Cai, J. T., Cao, Z., Chang, J., Chang, J. F., Chen, B. M., Chen, E. S., Chen, J., ... Zuo, X. (2021). Peta-electron volt gamma-ray emission from the Crab Nebula. *Science*, *373*, 425–430.

Liu, B., Yang, R.-z., & Chen, Z. (2022). Gamma-ray observation towards the young massive star cluster NGC 6618 in the M17 region. *MNRAS*, *513*(4), 4747–4753.

Longair, M. (2011). *High Energy Astrophysics* (draft, 3ed). CUP.

Mac Low, M.-M., & Klessen, R. S. (2004). Control of star formation by supersonic turbulence. *Reviews of Modern Physics*, *76*(1), 125–194.

Martire, F. A., Barreiro, R. B., & Martínez-González, E. (2022). Characterization of the polarized synchrotron emission from Planck and WMAP data. *Journal of Cosmology and Astroparticle Physics*, *2022*(4), 003.

Merloni, A., Predehl, P., Becker, W., Böhringer, H., Boller, T., Brunner, H., Brusa, M., Dennerl, K., Freyberg, M., Friedrich, P., Georgakakis, A., Haberl, F., Hasinger, G., Meidinger, N., Mohr, J., Nandra, K., Rau, A., Reiprich, T. H., Robrade, J., … German eROSITA Consortium, t. (2012). eROSITA Science Book: Mapping the Structure of the Energetic Universe. *arXiv e-prints*, arXiv:1209.3114.

Miller, J. M., Raymond, J., Cackett, E., Grinberg, V., & Nowak, M. (2016). An Ultra-fast X-Ray Disk Wind in the Neutron Star Binary GX 340+0. *ApJL*, *822*(1), L18.

Mitchell, A. M. W., & Gelfand, J. (2022). Pulsar Wind Nebulae. In *Handbook of x-ray and gamma-ray astrophysics* (p. 61).

Morales, E. F. E., Wyrowski, F., Schuller, F., & Menten, K. M. (2013). Stellar clusters in the inner Galaxy and their correlation with cold dust emission. *AAP*, *560*, A76.

Morlino, G., Blasi, P., Peretti, E., & Cristofari, P. (2021). Particle acceleration in winds of star clusters. *MNRAS*, *504*(4), 6096–6105.

Muno, M. P., Law, C., Clark, J. S., Dougherty, S. M., de Grijs, R., Portegies Zwart, S., & Yusef-Zadeh, F. (2006). Diffuse, Nonthermal X-Ray Emission from the Galactic Star Cluster Westerlund 1. *ApJ*, *650*(1), 203–211.

Navarete, F., Damineli, A., Ramirez, A. E., Rocha, D. F., & Almeida, L. A. (2022). Distance and age of the massive stellar cluster Westerlund 1. I. Parallax method using Gaia-EDR3. *MNRAS*, *516*(1), 1289–1301.

Negueruela, I., Alfaro, E. J., Dorda, R., Marco, A., Maíz Apellániz, J., & González-Fernández, C. (2022). Westerlund 1 under the light of Gaia EDR3: Distance, isolation, extent, and a hidden population. *AAP*, *664*, A146.

Ohm, S., Hinton, J. A., & White, R. (2013). γ-ray emission from the Westerlund 1 region. *MNRAS*, *434*(3), 2289–2294.

Padovani, M., Ivlev, A. V., Galli, D., Offner, S. S. R., Indriolo, N., Rodgers-Lee, D., Marcowith, A., Girichidis, P., Bykov, A. M., & Kruijssen, J. M. D. (2020). Impact of Low-Energy Cosmic Rays on Star Formation. *Space Science Reviews*, *216*(2), 29.

Pais, M., Pfrommer, C., Ehlert, K., & Pakmor, R. (2018). The effect of cosmic ray acceleration on supernova blast wave dynamics. *MNRAS*, *478*(4), 5278–5295.

Parizot, E., Marcowith, A., van der Swaluw, E., Bykov, A. M., & Tatischeff, V. (2004). Superbubbles and energetic particles in the Galaxy. I. Collective effects of particle acceleration. *AAP*, *424*, 747–760.

Pavlinsky, M., Tkachenko, A., Levin, V., Alexandrovich, N., Arefiev, V., Babyshkin, V., Batanov, O., Bodnar, Y., Bogomolov, A., Bubnov, A., Buntov, M., Burenin, R., Chelovekov, I., Chen, C. .-., Drozdova, T., Ehlert, S., Filippova, E., Frolov, S., Gamkov, D., … Yaskovich, A. (2021). The ART-XC telescope on board the SRG observatory. *AAP*, *650*, A42.

Piatti, A. E., Bica, E., & Claria, J. J. (1998). Fundamental parameters of the highly reddened young open clusters Westerlund 1 and 2. *AAPS*, *127*, 423–432.

Ponti, G., Zheng, X., Locatelli, N., Bianchi, S., Zhang, Y., Anastasopoulou, K., Comparat, J., Dennerl, K., Freyberg, M., Haberl, F., Merloni, A., Reiprich, T. H., Salvato, M., Sanders, J., Sasaki, M., Strong, A., & Yeung, M. C. H. (2023). Abundance and temperature of the outer hot circumgalactic medium. The SRG/eROSITA view of the soft X-ray background in the eFEDS field. *AAP*, *674*, A195.

Predehl, P., Andritschke, R., Arefiev, V., Babyshkin, V., Batanov, O., Becker, W., Böhringer, H., Bogomolov, A., Boller, T., Borm, K., Bornemann, W., Bräuninger, H., Brüggen, M., Brunner, H., Brusa, M., Bulbul, E., Buntov, M., Burwitz, V., Burkert, W., … Yaroshenko, V. (2021). The eROSITA X-ray telescope on SRG. *AAP*, *647*, A1.

Ruszkowski, M., & Pfrommer, C. (2023). Cosmic ray feedback in galaxies and galaxy clusters – A pedagogical introduction and a topical review of the acceleration, transport, observables, and dynamical impact of cosmic rays. *arXiv e-prints*, arXiv:2306.03141.

Saha, L., Domínguez, A., Tibaldo, L., Marchesi, S., Ajello, M., Lemoine-Goumard, M., & López, M. (2020). Morphological and Spectral Study of 4FGL J1115.1-6118 in the Region of the Young Massive Stellar Cluster NGC 3603. *ApJ*, *897*(2), 131.

Simpson, J. A. (1983). Elemental and Isotopic Composition of the Galactic Cosmic Rays. *Annual Review of Nuclear and Particle Science*, *33*, 323–382.

Skellam, J. G. (1946). The Frequency Distribution of the Difference between Two Poisson Variates Belonging to Different Populations. *Journal of the Royal Statistical Society*, *109*(3), 296–296.

Sun, X.-N., Yang, R.-Z., Liang, Y.-F., Peng, F.-K., Zhang, H.-M., Wang, X.-Y., & Aharonian, F. (2020). Diffuse γ-ray emission toward the massive star-forming region, W40. *AAP*, *639*, A80.

Sunyaev, R., Arefiev, V., Babyshkin, V., Bogomolov, A., Borisov, K., Buntov, M., Brunner, H., Burenin, R., Churazov, E., Coutinho, D., Eder, J., Eismont, N., Freyberg, M., Gilfanov, M., Gureyev, P., Hasinger, G., Khabibullin, I., Kolmykov, V., Komovkin, S., … Voron, V. (2021). SRG X-ray orbital observatory. Its telescopes and first scientific results. *AAP*, *656*, A132.

Tarricq, Y., Soubiran, C., Casamiquela, L., Cantat-Gaudin, T., Chemin, L., Anders, F., Antoja, T., Romero-Gómez, M., Figueras, F., Jordi, C., Bragaglia, A., Balaguer-Núñez, L., Carrera, R., Castro-Ginard, A., Moitinho, A., Ramos, P., & Bossini, D. (2021). 3D kinematics and age distribution of the open cluster population. *AAP*, *647*, A19.

Tibet ASγ Collaboration, Amenomori, M., Bao, Y. W., Bi, X. J., Chen, D., Chen, T. L., Chen, W. Y., Chen, X., Chen, Y., Cirennima, S. W., Cui, Danzengluobu, L. K., Ding, Fang, J. H., Fang, K., Feng, C. F., Feng, Z., Feng, Z. Y., Gao, Q., Gou, Q. B., Guo, Y. Q., … Zhaxisangzhu, X. X., Zhou. (2021). Potential PeVatron supernova remnant G106.3+2.7 seen in the highest-energy gamma rays. *Nature Astronomy*, *5*, 460–464.

Titarchuk, L. (1994). Generalized Comptonization Models and Application to the Recent High-Energy Observations. *ApJ*, *434*, 570.

Verner, D. A., Ferland, G. J., Korista, K. T., & Yakovlev, D. G. (1996). Atomic Data for Astrophysics. II. New Analytic FITS for Photoionization Cross Sections of Atoms and Ions. *ApJ*, *465*, 487.

Vieu, T., Gabici, S., & Tatischeff, V. (2020). Particle acceleration at colliding shock waves. *MNRAS*, *494*(3), 3166–3176.

Webber, W. R. (1998). A New Estimate of the Local Interstellar Energy Density and Ionization Rate of Galactic Cosmic Cosmic Rays. *ApJ*, *506*(1), 329–334.

Westerlund, B. E. (1987). Photometry and spectroscopy of stars in the region of a highly reddened cluster in Ara. *AAPS*, *70*, 311–324.

Westerlund, B. (1961). A Heavily Reddened Cluster in Ara. *AJ*, *66*, 57–57.

Wiener, J., Zweibel, E. G., & Ruszkowski, M. (2019). Cosmic ray acceleration of cool clouds in the circumgalactic medium. *MNRAS*, *489*(1), 205–223.

Wilms, J., Allen, A., & McCray, R. (2000). On the Absorption of X-Rays in the Interstellar Medium. *ApJ*, *542*(2), 914–924.

Workman, R. e. a. (2022). *Review of Particle Physics*. Prog. Theor. Exp. Phys.

Yang, R.-z., de Oña Wilhelmi, E., & Aharonian, F. (2018). Diffuse γ-ray emission in the vicinity of young star cluster Westerlund 2. *AAP*, *611*, A77.

Yeung, M. C. H., Freyberg, M. J., Ponti, G., Dennerl, K., Sasaki, M., & Strong, A. (2023). SRG/eROSITA X-ray shadowing study of giant molecular clouds. *AAP*, *676*, A3.

Yoast-Hull, T. M., Gallagher, J. S., & Zweibel, E. G. (2016). Equipartition and cosmic ray energy densities in central molecular zones of starbursts. *MNRAS*, *457*(1), L29–L33.

Zabalza, V. (2015). Naima: A python package for inference of relativistic particle energy distributions from observed nonthermal spectra. *Proc. of International Cosmic Ray Conference 2015*, 922.

Appendix

Δὶς ἐς τὸν αὐτὸν ποταμὸν οὐκ ἂν ἐμβαίης.

Ἡράκλειτος, Κρατύλος (Πλάτων)

1 Manually Selected Source Masks

Table A1.1: List of all manually chosen masks for the event file preparation. All masks are circular. α and δ are the right ascensions and declinations of their centers and R are their radii. Potential counterparts to the masked sources were found using the Vizier online library of astronomical catalogs[1]. HMXBs are high mass and LMXBs are low mass X-ray binaries.

α [°]	δ [°]	R [°]	Potential counterparts
251.449	-45.611	0.180	LMXB GX 340+0 / 4U 1642−45
250.462	-45.540	0.045	HMXB 2MASS J16415078-4532253
257.227	-44.102	0.230	LMXB 4U 1705-44
256.564	-43.036	0.180	LMXB X Ara X-1
255.706	-48.790	0.360	HMXB V* V821 Ara
247.022	-49.219	0.120	LMXB 4U 1624−49
250.319	-48.777	0.160	NGC 6193
247.809	-47.806	0.100	VPHAS J163114.1−474822.7
249.881	-47.839	0.080	1RXS J163931.4−475019
248.507	-47.393	0.080	LMXB X Nor X-1
252.027	-44.797	0.025	HMXB 2MASS J16480656−4512068
251.647	-44.882	0.025	HMXB 2MASS J16463526−4507045
256.045	-43.475	0.0292	1RXS J170410.9−443131
255.670	-44.618	0.0292	1RXS J170240.8−452254

---

[1] vizier.cds.unistra.fr

Table A1.1: Continuation.

α [°]	δ [°]	R [°]	Potential counterparts
252.362	-42.181	0.025	SWIFT J164926.9−434909
252.304	-42.074	0.025	
249.613	-43.754	0.075	
248.872	-47.901	0.025	
248.468	-47.889	0.025	Binary star HD 148937
246.325	-48.853	0.0292	Binary star HD 147633

2 Gaussian Fits and t-tests for Larger Regions

To check the robustness of my main result for higher statistics, I performed the same analysis as described in subsection 6.2.2 for two combinations of the regions Wd20, Wd30, and Wd40. These regions are defined as follows:

- **Wd1530:** Centered on $(\alpha, \delta) = (251.767°, -45.851°)$, reaching from a radius of 15 arcmin to a radius of 30 arcmin. The mask around the LMXB GX 340+0 is centered on $(\alpha, \delta) = (251.449°, -45.611°)$ and has a radius of 18 arcmin.
- **Wd2040:** Centered on $(\alpha, \delta) = (251.767°, -45.851°)$, reaching from a radius of 20 arcmin to a radius of 40 arcmin. The mask around the LMXB GX 340+0 is centered on $(\alpha, \delta) = (251.449°, -45.611°)$ and has a radius of 30 arcmin.

The corresponding test regions WdT1530 and WdT2040 are defined following the scheme described in subsection 6.2.2. Due to their larger extent, these analysis and test regions contain significantly more events than the smaller regions discussed in the main text.

Table A1.2: Resulting fit parameters of Gaussian fits to the residua histograms in figure A1.1. The parameters are the normalization A, the mean value μ, and the standard deviation σ. The two last columns give the t-statistic and the p-value of a one-sample left-sided t-test testing the null hypothesis that the mean of the distribution underlying the residua is equal to at least 0. The number of degrees of freedom is 874 in each case.

	A	μ	σ	t	p
Wd1530	872 ± 16	-0.56 ± 0.09	4.21 ± 0.09	-5.874	$3.024 \cdot 10^{-9}$
Wd2040	850 ± 40	-0.42 ± 0.21	4.45 ± 0.21	-3.654	$1.366 \cdot 10^{-4}$

The resulting fit parameters are given in table A1.2. The histograms and Gaussian fits are shown in figure A1.1. As before, the means of the Gaussian fits are negative, indicating less counts in the analysis than in the test regions. In addition, I also performed t-tests in the same way as before. The t-statistics and p-values are given in the same table and are in line with the results obtained for the smaller regions. In particular, the p-values are still below the threshold set for rejecting the null hypothesis.

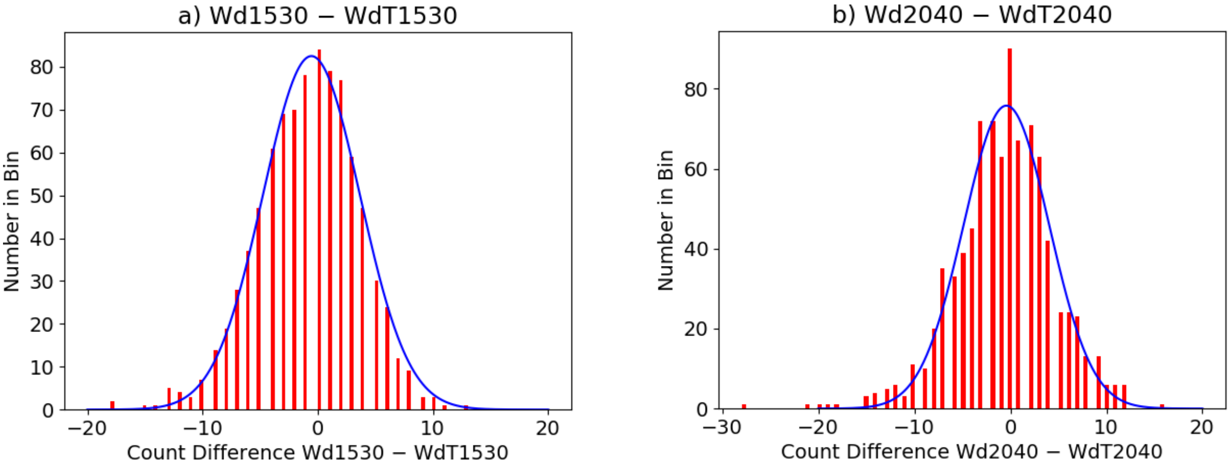

Figure A1.1: The red data shows the histogram of the residua of the subtraction of test region spectra from the corresponding analysis region spectra. The blue lines are Gaussian fits. The different panels are: *a* – Wd1530/WdT1530, *b* – Wd2040/WdT2040.

3 Filter Wheel Closed Model Parameters

Table A1.3: Normalizations for different TMs and FWC models. w are the dimensionless weighing factors multiplied with the X-ray models of the different TMs. They were fixed based on models provided by Jonathan Knies[2]. The B parameters are the normalizations of the FWC models for the different regions and TMs. They are given by the BACKSCAL keyword of the respective spectral fits files. This keyword gives the average area in deg^2 of the source region's intersection with the detector during the valid time intervals.

	TM1	TM2	TM3	TM4	TM6
w	1	1.156	1.144	1.006	1.100
B_{Wd10}	0.0320	0.0319	0.0318	0.0312	0.0321
B_{Wd20}	0.0679	0.0677	0.0675	0.0660	0.0681
B_{Wd30}	0.0868	0.0864	0.0875	0.0857	0.0866
B_{Wd40}	0.0841	0.0835	0.0840	0.0827	0.0839

---

[2] Private communication

Acknowledgment

> Ein Kopf denkt nie allein.
>
> Karlheinz Deschner

Human beings don't exist in isolation, and luckily not so. Without friends to share your interests and to have discussions with, life would be more boring, and if every young scientist had to start from zero again and again, science would be considerably less fruitful. We are indeed standing on the shoulders of giants, and we are also supported by family, friends, colleagues, and mentors. Therefore, a few words of gratitude are appropriate for a young man who is about to leave his alma mater.

First of all, I want to thank my supervisor Manami Sasaki, who not only offered me the opportunity to work on this Master's project, but who has been supporting me since my Bachelor's project. Further, this Master's thesis itself has seen considerable improvement thanks to the advice from many more people. Specifically, Konrad Dennerl, Victoria Grinberg, Amy Joyce, Philipp Thalhammer, and Aafia Zainab helped me to better understand the low mass X-ray binary GX 340+0 and its spectrum. Similarly, I want to thank Thomas Reiprich for pointing me towards the phenomenon of X-ray stray light as well as Michael Freyberg for helping me to interpret and deal with the said stray light contamination. In particular, I also want to thank Jonathan Knies for allowing me to use his analysis scripts and, more importantly, for providing frequent advice on `Xspec` and X-ray spectral analysis. This project would have been a lot more tedious without his help.

In a wider context, I want to express my gratitude towards Uli Katz for his help in navigating the bureaucracy of the university on many occasions and, specifically, for a short but important lesson on the nature of scientific research. In general, his support for the students of the university is remarkable and inspiring.

”Jedem Ende wohnt ein Anfang inne,” i.e., ”There is a new beginning to each ending.”[1] Accordingly, I do not only want to look back to my Master's studies, but also into the future. In that regard, I am particularly grateful to Stacy McGaugh, Sebastian von Hausegger, Federico Lelli, and Marcel Pawlowski for their invaluable support during a time of great uncertainty. In

---

[1] Sometimes attributed to Hermann Hesse, though it rather seems to be a modification of his ”Jedem Anfang wohnt ein Zauber inne.” In the end, the meaning of a phrase lies primarily in its content anyway, and only secondarily in its author.

the end, everything seems to have worked out and I am looking forward to my doctoral studies with Federico Lelli.

Further, a strong and, in my opinion, positive influence on my attitude towards the quest for knowledge came from my dear friends Helmut Fink and Jonas Pöld, who taught me the importance of philosophy, specifically the philosophy of science. This is a discipline which I used to disregard far too easily in the past, but into which I hope to delve deeper in the future.

Entering the private realm even further now, I want to thank my parents. For obvious reasons, none of this would have been possible without them and their support. In a similar fashion, I am also grateful towards my two uncles who encouraged my curiosity and my interest in the sciences since my earliest childhood. Without them, too, I would not be where I am now, and I doubt that it would be a better place.

For certain, however, the last years would have been less enjoyable without my good friend Florian Steynberg. We spent more than the last five years together having many fruitful discussions, finishing a lot of laboratory experiments, and importantly, sometimes just having a good time. These were some of my most formative years and I am happy that we got through this together.

Finally, thanks to my partner Nico Büttner for everything. You arrived just when I needed you, you inspired me, and gave me the courage to reach for what I aspire. I am looking forward to the future.

This work is based on data from eROSITA, the soft X-ray instrument aboard SRG, a joint Russian-German science mission supported by the Russian Space Agency (Roskosmos), in the interests of the Russian Academy of Sciences represented by its Space Research Institute (IKI), and the Deutsches Zentrum für Luft- und Raumfahrt (DLR). The SRG spacecraft was built by Lavochkin Association (NPOL) and its subcontractors, and is operated by NPOL with support from the Max Planck Institute for Extraterrestrial Physics (MPE).

The development and construction of the eROSITA X-ray instrument was led by MPE, with contributions from the Dr. Karl Remeis Observatory Bamberg & ECAP (FAU Erlangen-Nuernberg), the University of Hamburg Observatory, the Leibniz Institute for Astrophysics Potsdam (AIP), and the Institute for Astronomy and Astrophysics of the University of Tübingen, with the support of DLR and the Max Planck Society. The Argelander Institute for Astronomy of the University of Bonn and the Ludwig Maximilians Universität Munich also participated in the science preparation for eROSITA. The eROSITA data shown here were processed using the eSASS software system developed by the German eROSITA consortium.

Eigenständigkeitserklärung

Hiermit bestätige ich, dass ich diese Arbeit selbstständig und nur unter Verwendung der angegebenen Quellen und Hilfsmittel angefertigt habe.